

# **COUPLED SOLITARY WAVES IN OPTICAL WAVEGUIDES**

A Thesis submitted for  
the degree of Doctor of Philosophy at the  
University of New South Wales

William Chi Keung Mak

School of Electrical Engineering, University of New South Wales,  
Kensington, New South Wales 2052, Australia.

1998

## Acknowledgements

I would like to extend my thanks to my supervisors, Prof. P. L. Chu, and Dr. I. M. Skinner, for the excellent supervisions they provided. Especially, I would thank Prof. Chu for all the help, advice and assistance which he gave besides those related to academic matters. I whole-heartedly appreciate.

Moreover, I would like to extend my gratefulness to Prof. B. A. Malomed. He opened up my eyes and mind in mathematics. His teaching led me to the correct understanding of solitons. He also taught me how to gain a better relationship with other people. Without his guidance, this thesis could not come to fruition.

# Abstract

Soliton states in three coupled optical waveguide systems were studied: two linearly coupled waveguides with quadratic nonlinearity, two linearly coupled waveguides with cubic nonlinearity and Bragg gratings, and a quadratically nonlinear waveguide with resonant gratings, which enable three-wave interaction. The methods adopted to tackle the problems were both analytical and numerical. The analytical method mainly made use of the variational approximation. Since no exact analytical method is available to find solutions for the waveguide systems under study, the variational approach was proved to be very useful to find accurate approximations. Numerically, the shooting method and the relaxation method were used. The numerical results verified the results obtained analytically. New asymmetric soliton states were discovered for the coupled quadratically nonlinear waveguides, and for the coupled waveguides with both cubic nonlinearity and Bragg gratings. Stability of the soliton states was studied numerically using the Beam Propagation Method. Asymmetric couplers with quadratic nonlinearity were also studied. The bifurcation diagrams for the asymmetric couplers were those unfolded from the corresponding diagrams of the symmetric couplers. Novel *stable* two-soliton bound states due to three-wave interaction were discovered for a quadratically nonlinear waveguide equipped with resonant gratings. Since the coupled optical waveguide systems are controlled by a larger number of parameters than in the corresponding single waveguide, the coupled systems can find a much broader field of applications. This study provides useful background informations to support these applications.

## List of Publications

1. W.C.K. Mak, B.A. Malomed, and P.L. Chu, “Three-wave Gap Solitons in Waveguides with Quadratic Nonlinearity”, *Phys. Rev. E*, **58**, 6708–6722, (Nov. 1998).
2. W.C.K. Mak, B.A. Malomed, and P.L. Chu, “Solitary Waves in Asymmetric Coupled Waveguides with Quadratic Nonlinearity”, *Opt. Commun.*, **154**, 145–151 (Aug. 1998).
3. W.C.K. Mak, B.A. Malomed, and P.L. Chu, “Solitary Waves in Coupled Non-linear Waveguides with Bragg Gratings”, *J. Opt. Soc. Am. B* **15**, 1685–1692 (Jun. 1998).
4. W.C.K. Mak, B.A. Malomed, and P.L. Chu, “Asymmetric Solitons in Coupled Second-Harmonic-Generating Waveguides”, *Phys. Rev. E*, **57**, 1092–1103 (Jan. 1998).
5. W.C.K. Mak, B.A. Malomed, and P.L. Chu, “Solitons in Coupled Waveguides with Quadratic Nonlinearity”, *Phys. Rev. E*, **55**, 6134–6140 (May 1997).
6. W.C.K. Mak, “Soliton Switching in Fused Tapered Fibre Couplers”<sup>1</sup>, *Technical Digest, Tenth Int. Conf. on Integrated Opt. and Opt. Fibre Commun.*, The Chinese University of Hong Kong Press, **3**, 150 (Jun. 1995).

---

<sup>1</sup>The materials of this paper are not covered in this thesis.

# Contents

## 1 Introduction 1

1.1	Historic Perspective . . . . .	1
1.2	Origin of Optical Nonlinearity . . . . .	4
1.3	The Constitutive Relation . . . . .	5
1.3.1	Time-domain Response Function Approach . . . . .	6
1.3.2	Frequency Domain Susceptibility Approach . . . . .	7
1.4	Solitary Wave Propagation Equations . . . . .	9
1.4.1	Equations for Spatial Solitons in Slab Waveguides . . . . .	9
1.4.2	Normalization . . . . .	16

## 2 Closely Coupled $\chi^{(2)}$ Waveguides 19

2.1	Introduction . . . . .	19
2.2	Mathematical Model . . . . .	21
2.3	Stationary Solutions . . . . .	23
2.3.1	Variational Analysis . . . . .	25
2.3.2	Zero-mode Analysis . . . . .	31
2.3.3	Numerical Check of VA results . . . . .	33
2.3.4	Comparison of Results . . . . .	36

2.4	Stability of the Solitons . . . . .	38
2.4.1	Beam Propagation Method . . . . .	40
2.4.2	Error Analysis . . . . .	42
2.4.3	Stability of the Asymmetric and Symmetric Solitons . . . . .	44
2.5	Summary . . . . .	48
<b>3</b>	<b>Coupled Quadratically Nonlinear Waveguides</b>	<b>50</b>
3.1	Introduction . . . . .	50
3.2	Mathematical Model . . . . .	51
3.3	Stationary Solution . . . . .	52
3.3.1	Variational Analysis . . . . .	53
3.3.2	Newton-Raphson method . . . . .	55
3.3.3	Numerical Analysis . . . . .	57
3.3.4	Discussion of Results . . . . .	58
3.4	The Stability Analysis . . . . .	68
3.5	Conclusion . . . . .	72
<b>4</b>	<b>Secondary Effects</b>	<b>74</b>
4.1	Introduction . . . . .	74
4.2	Effects of Spatial Walkoff . . . . .	76
4.3	Effects of Varying the Phase Mismatch . . . . .	81
4.4	Asymmetric Coupler . . . . .	85
4.4.1	Mathematical Model . . . . .	86
4.4.2	Results . . . . .	87
4.4.3	Solitons in the Coupler with One Linear and One Nonlinear Cores . . . . .	96

4.5	Conclusion . . . . .	98
<b>5</b>	<b>Coupled Waveguides with Bragg Gratings</b>	<b>100</b>
5.1	Introduction . . . . .	100
5.2	Background Theory . . . . .	103
5.3	Coupled-Mode Equations for a Single Nonlinear Waveguide . . . . .	106
5.4	Scope of Investigation . . . . .	109
5.5	The Mathematical Techniques . . . . .	110
5.6	Stationary Solutions . . . . .	116
	5.6.1 Quiescent Solitons . . . . .	116
	5.6.2 Moving Solitary Waves . . . . .	123
5.7	The Stability Analysis . . . . .	124
5.8	Discussion . . . . .	126
5.9	Conclusion . . . . .	131
<b>6</b>	<b>Three Wave Gap Solitons</b>	<b>132</b>
6.1	Introduction . . . . .	132
6.2	Scope of Study . . . . .	134
6.3	The Model . . . . .	137
6.4	The Linearized and Semilinearized Systems . . . . .	139
6.5	Analytical and Numerical Techniques . . . . .	141
6.6	Stationary Solutions: Existence and Stability . . . . .	142
6.7	Two-Soliton States . . . . .	151
6.8	Conclusion . . . . .	162

**7 Conclusion 163**

# Chapter 1

## Introduction

### 1.1 Historic Perspective

The search of new communication technology always remains the quest of human society for the betterment of our living conditions. The communication technology is also always at the forefront of all other sciences and technologies.

Ever since the invention of telephone at the beginning of this century, the dissemination of information has become faster and more and more convenient, the volume of information being transferred has grown exponentially, and the pace of advancement has accelerated at a faster and faster speed. At the same time, the advancement in communication technology opens up new opportunity and challenges for the whole society.

From mid- to late-1970s, we saw the advent of telecommunications using optical fibres. Uncladded glass fibres, in fact, were first fabricated in the 1920s, with J. L. Baird registering a British patent [1] in 1927. Considerable improvement in the fibre characteristics was made in 1950s, when a cladding layer was proposed [2],

though these early fibres were still extremely lossy. Thus, the use of glass fibres was just confined to short distance image transmission. In 1966, Kao and Hockham [3] suggested to use optical fibres as the medium for long distance communication systems. Following that, much progress was made in the glass fibre fabrication process. By 1979, a loss level of about  $0.2\text{dB}/\text{km}$  near the  $1.55\mu\text{m}$  wavelength was reached; this limit was imposed mainly by the inherent Rayleigh scattering process.

The emergence of low loss fibres stimulated the study of nonlinear phenomena in both optical fibres and waveguides. In the last twenty years, the intense activities in the study of the nonlinear effects in optical fibre has resulted in a number of important advances. The nonlinear effects in optical fibres have been exploited to develop new kinds of lasers such as the fibre Raman lasers and the soliton lasers. The advances in laser, on the other hand, bring the use of optical fibres for telecommunications steps closer to reality. The nonlinearity has also been used for pulse compression to produce optical pulses as short as under  $5\text{fs}$ .

In 1973, an important contribution was made by Hasegawa and Tappert. Inspired by Hasegawa's earlier work on electron cyclotron wave in a plasma field, which had similar modelling equations; i.e., the well-known Nonlinear Scrodinger Equation, they demonstrated the stability of solitons for the light wave envelope in fibres by performing various computer simulations [4]. They also recognised the fact that the dispersive distortion in such optical solitons in optical fibres can be suppressed by the nonlinear effect implied immense potential of its use for high speed telecommunication. This triggered off heated research interests in  $\chi^{(3)}$  nonlinear materials, which mainly mean silica glass. Numerous papers has been published, from 1970s until present, on various topics such as stimulated Raman and Brillouin scatterings, self-phase and cross-phase modulation, parametric four-wave mixing,

optically induced birefringence, nonlinear pulse compression techniques, etc. The number of such works is so large that it is not possible to list all of them and it is unrespectful to cite just a few.

In recent years, there have been renewed efforts in the research of nonlinearity in  $\chi^{(2)}$  materials; i.e., materials with quadratic nonlinearity. As a matter of fact, research efforts were at first focused here in 1960s, when researchers began to look into nonlinear optical properties of materials. However, the excitement over the immense potential of silica glass fibres to be used in long-haul telecommunications diverted the attention of researchers. Silica glass, being a material with molecular inverse symmetry, does not exhibit second order nonlinearity. The lowest order of nonlinearity is cubic, which is inherently smaller, by several orders of magnitude, when compared with the quadratic nonlinearity which is found in materials such as KTP, or some organic polymer materials. This makes the use of silica glass for small-size portable optical switching devices unattractive. This is also the reason why the research interests in  $\chi^{(2)}$  materials revives recently in these few years. Researchers explore the potential in the use of  $\chi^{(2)}$  materials as all-optical switching devices.

In this thesis, the topics to be discussed exactly adhere to this theme. Specifically, my research efforts have been concentrated on the switching characteristics of *soliton*. Here, I would like to first clarify my usage of terms. In this thesis, I use the terms "soliton" and "solitary wave" interchangeably to loosely mean the same thing; i.e., localized solution to the modelling equations. Thus, I do not adhere to the conventional use of the term "soliton" to denote localized solutions to the modelling partial differential equations, which are integrable by the Inverse Scattering Transform technique. All the models considered in this thesis are not integrable in this sense.

## 1.2 Origin of Optical Nonlinearity

I now describe briefly how the nonlinear effect in materials can arise. We can consider the materials in optics as a collections of positively charged ions, surrounded by negatively charged electrons. When an electric field is applied, the charged particles are moved. In dielectric materials, this movement is limited because the charged particles are bounded together; they are just slightly displaced from their equilibrium positions. This slight displacement induces an effect which we call polarization, or electric dipole moments.

If this electric field is due to a light wave passing through the dielectric materials, the motion of the particles (which mainly are that of electrons), in response to the optical electric field, is thus oscillatory. For simplicity, we consider the optical wave to be monochromatic. If the applied electric field of the optical wave is not large, the oscillation of the electric charges will be sinusoidal, and the induced polarization will be at the same frequency harmonious with the incident optical field. So, we can express the polarization  $\tilde{P}$  as

$$\tilde{P} = \frac{1}{2}\epsilon_o\tilde{\chi}\tilde{E}_o\exp(i\omega t) + c.c., \quad (1.1)$$

where  $\tilde{E}_o$ , and  $\omega$  are the amplitude, and frequency of the optical field,  $\tilde{\chi}$  is the linear susceptibility and  $\epsilon_o$  is the free space permittivity. (Note that, in this thesis, we use the tilde accent to stand for vector and tensor quantities.) So, what we have considered is the linear regime. It is approximately true if the applied optical field and thus the displacements of the electric charges are small. For stronger optical wave, and thus larger displacements, the dielectric restoring force will then be significantly nonlinear. This anharmonic response gives rise to an induced polarization which is significantly nonlinear too. Spectral analysis will show that the polarization will

contains significant components oscillating at the harmonic frequencies  $2\omega, 3\omega, \dots$ , etc.. Mathematically, we can express the polarization  $\tilde{P}$  in the form:

$$\begin{aligned}\tilde{P} &= \tilde{P}^{(0)} + \tilde{P}^{(1)} + \tilde{P}^{(2)} + \dots + \tilde{P}^{(n)} + \dots \\ &= \epsilon_o(\tilde{\chi}^{(1)}\tilde{E} + \tilde{\chi}^{(2)}\tilde{E}^2 + \tilde{\chi}^{(3)}\tilde{E}^3 + \dots),\end{aligned}\tag{1.2}$$

where  $\tilde{P}^{(1)}$  and  $\tilde{\chi}^{(1)}$  are the linear polarization and linear susceptibility,  $\tilde{P}^{(2)}$  and  $\tilde{\chi}^{(2)}$  are quadratic, and so on.

The component of the polarization  $\tilde{P}$  at the second harmonic frequency  $2\omega$  will radiate an electric field at the frequency  $2\omega$ . This is then the phenomenon of second harmonic generation. Higher harmonic terms will give rise to many more nonlinear optical phenomena, such as Kerr Effect if the cubic nonlinear term is considered.

### 1.3 The Constitutive Relation

Constitutive relation is the relation between the induced polarization  $\tilde{P}(t)$  and the driving electric field  $\tilde{E}(t)$ . It can be considered from two approaches : one is based on time-domain response function, and the other is on the frequency-domain susceptibilities. These two alternative approaches will be considered briefly; details can be found in, e.g., [5]. Also, here we only consider the local response, which means that the polarization at a point in the dielectric medium is determined by the electric field at the same point in space. This usually is a very good assumption for the kind of optical problems considered in this thesis [6].

### 1.3.1 Time-domain Response Function Approach

The most general possible relation between the time dependent  $n$ th-order polarization  $\tilde{P}^{(n)}(t)$  and the electric field  $\tilde{E}(t)$  is

$$\tilde{P}^{(n)}(t) = \epsilon_o \int_{-\infty}^{+\infty} d\tau_1 \cdots \int_{-\infty}^{+\infty} d\tau_n \tilde{T}^{(n)}(t; \tau_1, \cdots, \tau_n) | \tilde{E}(\tau_1) \cdots \tilde{E}(\tau_n), \quad (1.3)$$

where a vertical bar is used to replace a column of  $n$  dots which indicate the contraction operation.  $\tilde{T}^{(n)}(t; \tau_1, \cdots, \tau_n)$  is a  $(n+1)$ th-rank tensor which is a function of the  $(n+1)$  times  $t, \tau_1, \cdots, \tau_n$ . The individual component of  $\tilde{T}^{(n)}$  can be expressed in suffix notation as  $T_{\mu\alpha_1\cdots\alpha_n}$ , where  $\mu, \alpha_1, \cdots, \alpha_n$  are labels for the coordinate axes (i.e.,  $x, y, z$  in Cartesian coordinates).  $\mu$  refers to the coordinate axis where the component of the polarization  $\tilde{P}$  considered lies. In general, the tensor  $\tilde{T}^{(n)}$  is not unique, because there are  $n!$  different orders to arrange the terms  $\tilde{E}(\tau_1) \cdots \tilde{E}(\tau_n)$ . However, the usual convention is to define  $\tilde{T}^{(n)}$  by the average over the  $n!$  possible permutations, and thus making  $\tilde{T}^{(n)}$  unique. Then, by invoking the Principle of Time Invariance, it can be easily shown that

$$\tilde{T}^{(n)}(t; \tau_1 - t_o, \cdots, \tau_n - t_o) = \tilde{T}^{(n)}(t + t_o; \tau_1, \cdots, \tau_n), \quad (1.4)$$

which simply means that  $\tilde{T}^{(n)}$  depends only on the difference between the times  $t$  and  $\tau$ 's, but not on their individual values. Thus, we can define a parameter called polarization response function  $\tilde{X}^{(n)}(\tau_1, \cdots, \tau_n)$  as

$$\tilde{X}^{(n)}(\tau_1, \cdots, \tau_n) \equiv \tilde{T}^{(n)}(t; t - \tau_1, \cdots, t - \tau_n). \quad (1.5)$$

Using this definition, Eq.(1.3) becomes

$$\tilde{P}^{(n)}(t) = \epsilon_o \int_{-\infty}^{+\infty} d\tau_1 \cdots \int_{-\infty}^{+\infty} d\tau_n \tilde{X}^{(n)}(\tau_1, \cdots, \tau_n) | \tilde{E}(t - \tau_1) \cdots \tilde{E}(t - \tau_n). \quad (1.6)$$

Since in most of this thesis, we are dealing with solitons in medium with quadratic nonlinearity, I will write, in particular, the canonical form for the quadratic polarization:

$$\tilde{P}^{(2)}(t) = \epsilon_o \int_{-\infty}^{+\infty} d\tau_1 \int_{-\infty}^{+\infty} d\tau_2 \tilde{X}^{(2)}(\tau_1, \tau_2) : \tilde{E}(t - \tau_1) \tilde{E}(t - \tau_2) \quad (1.7)$$

### 1.3.2 Frequency Domain Susceptibility Approach

Susceptibility is a more commonly used approach, although it is exactly equivalent to the time domain response function approach. To be able to work in the frequency domain, the electric field  $\tilde{E}(t)$  has to be expressed in terms of its Fourier transform:

$$\tilde{E}(t) = \int_{-\infty}^{+\infty} d\omega \tilde{E}(\omega) \exp(-i\omega t), \quad (1.8)$$

where

$$\tilde{E}(\omega) = \frac{1}{2\pi} \int_{-\infty}^{+\infty} d\tau \tilde{E}(\tau) \exp(i\omega t) \quad (1.9)$$

If we substitute Eq.(1.8) into Eq.(1.6), we obtain the  $n$ -th order polarization  $\tilde{P}^{(n)}(t)$  as:

$$\begin{aligned} \tilde{P}^{(n)}(t) = & \epsilon_o \int_{-\infty}^{+\infty} d\omega_1 \cdots \int_{-\infty}^{+\infty} d\omega_n \int_{-\infty}^{+\infty} d\tau_1 \cdots \int_{-\infty}^{+\infty} d\tau_n \tilde{X}^{(n)}(\tau_1, \dots, \tau_n) | \\ & \tilde{E}(\omega_1) \cdots \tilde{E}(\omega_n) \exp\{ -i[\omega_1(t - \tau_1) + \omega_2(t - \tau_2) + \cdots \\ & + \omega_n(t - \tau_n)] \}. \end{aligned} \quad (1.10)$$

If we now group all the  $i\omega_j\tau_j$  terms, where  $j = 1, \dots, n$ , together and define the susceptibility tensor  $\tilde{\chi}^{(n)}$  by

$$\tilde{\chi}^{(n)}(\omega_s; \omega_1, \dots, \omega_n) = \int_{-\infty}^{+\infty} d\tau_1 \cdots \int_{-\infty}^{+\infty} d\tau_n \tilde{X}^{(n)}(\tau_1, \dots, \tau_n) \exp\{i \sum_{j=1}^n \omega_j \tau_j\}, \quad (1.11)$$

where  $\omega_s = \sum_{j=1}^n \omega_j$ , we have

$$\begin{aligned} \tilde{P}^{(n)}(t) &= \epsilon_o \int_{-\infty}^{+\infty} d\omega_1 \cdots \int_{-\infty}^{+\infty} d\omega_n \tilde{\chi}^{(n)}(\omega_s; \omega_1, \dots, \omega_n) | \\ &\quad \tilde{E}(\omega_1) \cdots \tilde{E}(\omega_n) \exp(-i\omega_s t). \end{aligned} \quad (1.12)$$

Of course, by using the term  $\tilde{\chi}^{(n)}(\omega_s; \omega_1, \dots, \omega_n)$ , we implicitly confine our consideration of  $\tilde{P}^{(n)}(t)$  at a single frequency  $\omega_s$  and ignore components of  $\tilde{P}^{(n)}(t)$  at other possible frequencies. In other word, the Fourier component of  $\tilde{P}^{(n)}(t)$  at  $\omega_s$  is given by:

$$\tilde{P}^{(n)}(\omega_s) = \epsilon_o \tilde{\chi}^{(n)}(\omega_s; \omega_1, \dots, \omega_n) | \tilde{E}(\omega_1) \cdots \tilde{E}(\omega_n) \quad (1.13)$$

Sometimes, it is a common practice to extract the directional components out of all the vectors and tensors so that the parameter susceptibility can be expressed in scalar form. We write

$$\tilde{E}_{\omega_j} = \tilde{e}_j E_j, \quad (1.14)$$

where  $\tilde{E}_{\omega_j}$  is the component of the electric field at frequency  $\omega_j$ ,  $E_j$  is the complex amplitude scalar, and  $\tilde{e}_j$  is an unit vector in the direction of the electric field  $\tilde{E}_{\omega_j}$ .

We can then define a scalar nonlinear susceptibility by

$$\chi^{(n)}(\omega_s; \omega_1, \dots, \omega_n) = \tilde{e}_s^* \cdot \tilde{\chi}^{(n)}(\omega_s; \omega_1, \dots, \omega_n) | \tilde{e}_1 \cdots \tilde{e}_n, \quad (1.15)$$

where  $\tilde{e}_s$  is in the direction of the component of polarization under consideration.

So, the scalar component of polarization in the direction of  $\tilde{e}_s$  is

$$\begin{aligned} P_s^{(n)}(t) &= \epsilon_o \int_{-\infty}^{+\infty} d\omega_1 \cdots \int_{-\infty}^{+\infty} d\omega_n \\ &\quad \chi^{(n)}(\omega_s; \omega_1, \dots, \omega_n) E_1 \cdots E_n \exp(-i\omega_s t), \end{aligned} \quad (1.16)$$

i.e.,  $\tilde{P}_{\omega_s}^{(n)}(\omega) = \tilde{e}_s P_s^{(n)}(\omega)$ . To be clearer, it is written out as:

$$P_s^{(n)}(\omega) = \epsilon_o \chi^{(n)}(\omega_s; \omega_1, \dots, \omega_n) E_1 \cdots E_n. \quad (1.17)$$

As was done in the last subsection, I also write the scalar canonical form for the quadratic polarization:

$$P_s^{(2)}(t) = \epsilon_o \int_{-\infty}^{+\infty} d\omega_1 \int_{-\infty}^{+\infty} d\omega_2 \chi^{(2)} E_1 E_2 \exp[ -i(\omega_1 + \omega_2)t], \quad (1.18)$$

and  $\chi^{(2)}$  is given by

$$\chi^{(2)}(\omega_s; \omega_1, \omega_2) = \tilde{\epsilon}_s^* \cdot \tilde{\chi}^{(2)}(\omega_s; \omega_1, \omega_2) \cdot \tilde{\epsilon}_1 \tilde{\epsilon}_2. \quad (1.19)$$

In the next section, we proceed to derive the equations describing the propagation of optical solitons in a nonlinear medium.

## 1.4 Solitary Wave Propagation Equations

In this section, the objective is to obtain basic equations which describe the propagation of optical solitons in waveguides. Since in this thesis, we mostly deal with spatial solitons in slab waveguides, the derivation will be confined to this situation. However, because of the well-known duality between the spatial and temporal solitons, equations for temporal solitons take the same forms and can be derived similarly. Nevertheless, the inclusion of the derivation of these basic equations here is just for the completeness of the thesis. It is not the author's original work. Excellent derivations can be found in a lot of places; [5, 7, 8, 9, 10] are a few examples which I made reference to.

### 1.4.1 Equations for Spatial Solitons in Slab Waveguides

The starting point is Maxwell's Equations :

$$\nabla \times \tilde{E}(t) = \frac{\partial}{\partial t} \tilde{B}(t)$$

$$\nabla \times \tilde{H}(t) = \epsilon_o \frac{\partial}{\partial t} \tilde{E}(t) + \tilde{J}(t), \quad (1.20)$$

where the symbols carry their usual meanings. In optics, we are usually concerned with materials which are nonconductive, contain no free charge, so that  $\tilde{J}(t)$  consists of only the polarization current  $\partial \tilde{P}(t)/\partial t$ ; and nonmagnetic, so that  $\tilde{B}(t) = \mu_o \tilde{H}(t)$ . We can eliminate  $\tilde{H}(t)$  from Eq.(1.20) to get the following vector wave equation for the electric field (in SI units):

$$\nabla \times \nabla \times \tilde{E}(t) = \mu_o \frac{\partial^2}{\partial t^2} \tilde{D}(t), \quad (1.21)$$

where  $\tilde{D}(t)$  is the electric displacement vector, which can be expressed in terms of  $\tilde{E}(t)$  and  $\tilde{P}(t)$  as

$$\tilde{D}(t) = \epsilon_o \tilde{E}(t) + \tilde{P}(t) \quad (1.22)$$

So, we have

$$\nabla \times \nabla \times \tilde{E}(t) = \frac{1}{c^2} \frac{\partial^2}{\partial t^2} \tilde{E}(t) - \mu_o \frac{\partial^2}{\partial t^2} \tilde{P}(t) \quad (1.23)$$

We may choose to work with Eq.(1.23) in the time domain, but instead I use the frequency domain. Thus, for the frequency component  $\omega$ :

$$\nabla \times \nabla \times \tilde{E}(\omega) = \frac{\omega^2}{c^2} \tilde{E}(\omega) + \omega^2 \mu_o \tilde{P}(\omega). \quad (1.24)$$

To consider the nonlinear processes, it is usual to separate the polarization  $\tilde{P}(\omega)$  into its linear and nonlinear parts, by writing:

$$\tilde{P}(\omega) = \epsilon_o \chi^{(1)}(\omega; \omega) \cdot \tilde{E}(\omega) + \tilde{P}^{\text{NL}}(\omega), \quad (1.25)$$

where  $\tilde{P}^{\text{NL}}(\omega) = \sum_{n=2}^{\infty} \tilde{P}^{(n)}(\omega)$  and  $\tilde{P}^{(n)}(\omega)$  are given by Eq.(1.13). Substituting Eq.(1.25) into Eq.(1.24), and we will get

$$\nabla \times \nabla \times \tilde{E}(\omega) = \frac{\omega^2}{c^2} \tilde{\epsilon} \cdot \tilde{E}(\omega) + \omega^2 \mu_o \tilde{P}^{\text{NL}}(\omega), \quad (1.26)$$

where the linear permittivity  $\tilde{\epsilon}$  is given by  $\tilde{\epsilon} = 1 + \tilde{\chi}^{(1)}$ .

We consider travelling wave solutions of the wave equation Eq.(1.26); which is of the form

$$\tilde{E}(\omega) = \tilde{\epsilon} E(\omega) \exp(i\tilde{k} \cdot \tilde{r}), \quad (1.27)$$

where  $\tilde{k}$  is the wave vector,  $\tilde{r}$  is the positional vector, and  $\tilde{\epsilon}$  is the unit vector in the polarization direction of the  $\tilde{E}$  vector.  $E(\omega)$  is a slowly varying envelope function. Assuming that the nonlinearity is weak, we can consider  $\tilde{E}$  and  $\tilde{D}$  to be a superposition of  $n$  nearly monochromatic waves, thus,

$$\begin{aligned} \tilde{E}(x, y, z, \omega) &= \sum_{i=1}^n \tilde{\epsilon}_i E_i(x, y, z, \omega) \exp(i\tilde{k}_i \cdot \tilde{r}) + c.c. \\ \tilde{D}(x, y, z, \omega) &= \sum_{i=1}^n \tilde{d}_i D_i(x, y, z, \omega) \exp(i\tilde{k}_i \cdot \tilde{r}) + c.c., \end{aligned} \quad (1.28)$$

where the dependence on the spatial co-ordinates  $x, y, z$  has been explicitly spelt out. To find the linear dispersion relation, we can just consider a single monochromatic wave. When the amplitude is small enough, the nonlinear term can be ignored. Eq.(1.26) give

$$\nabla \times \nabla \times \tilde{E}(\omega) = \frac{\omega^2}{c^2} \tilde{\epsilon} \cdot \tilde{E}(\omega) \quad (1.29)$$

By putting the wave vector  $\tilde{k}$  as

$$\tilde{k} = \frac{\omega n}{c} \tilde{s}, \quad (1.30)$$

where  $\tilde{s}$  is an unit vector in the direction of propagation, and using Eq.(1.28) we can obtain from Eq.(1.29) the Fresnel's equation :

$$[(\tilde{s} \cdot \tilde{\epsilon})\tilde{s} - \tilde{\epsilon}]n^2 + \tilde{\epsilon} \cdot \tilde{\epsilon} = 0 \quad (1.31)$$

The three components of Eq.(1.31) are three homogeneous linear equations for each component of  $\tilde{\epsilon}$ . The solvability condition (i. e. the determinant of their coefficients

must vanish) gives the linear dispersion relation:

$$s_x^2(n^2 - n_y^2)(n^2 - n_z^2) + s_y^2(n^2 - n_x^2)(n^2 - n_z^2) + s_z^2(n^2 - n_x^2)(n^2 - n_y^2) = 0, \quad (1.32)$$

where the subscripts  $x, y, z$  denote the coordinate axes which have been aligned to the principal axes of the dielectric tensor  $\tilde{\epsilon}$ , and  $n_x = \sqrt{\epsilon_{xx}}$ ,  $n_y = \sqrt{\epsilon_{yy}}$ , and  $n_z = \sqrt{\epsilon_{zz}}$ .

This equation is quadratic in  $n^2$ , thus has four roots; two pairs each of the same magnitude but opposite sign. The opposite sign just means travelling waves in opposite directions. So, there are just two distinct values of  $n$ , corresponding to two distinct phase velocities (i. e., birefringence) for wave propagating in a given direction of  $\tilde{s}$ : They are called the ordinary and extraordinary waves. If we consider an uniaxial birefringent medium, for the ordinary wave, the directions of the wave vector  $\tilde{s}$  and the Poynting vector  $\tilde{N} = \tilde{E} \times \tilde{H}$  are the same; for the extraordinary wave, the directions of the wave vector  $\tilde{s}$  and the Poynting vector  $\tilde{N}$  are different, which means an energy walkoff from the wave travelling direction.

On the other hand, for a strong nonlinear parametric interaction of monochromatic waves, phase matching is always essential. A common phase matching technique makes use of the birefringence as mentioned above. For example, in the case of second harmonic generation (SHG), there are two typical techniques: for the so-called type I SHG method, both fundamental harmonic waves are of ordinary waves, and the second harmonic wave is of extraordinary wave; for the type II SHG method, one of the fundamental harmonics is of ordinary polarization, whereas the other fundamental harmonic and the second harmonic are of extraordinary polarization. Thus, in general, when we consider nonlinear wave mixing, we usually have to make provision to take this energy walkoff effect into account in the model. A

scheme was adopted which re-write Eq.(1.28), e. g. for  $\tilde{E}$ , as

$$\tilde{E}(x, y, z, w) = \sum_{i=1}^n \tilde{e}_i E_i(x - \rho_i z, y, z) \exp(ik_i z) + c.c., \quad (1.33)$$

where each  $\rho_i$  is the angle between the Poynting vector  $\tilde{n}_i$  (which is used to denote the unit vector in the direction of the Poynting vector) and the wave vector  $\tilde{s}_i$ .

In this equation, the  $z$ -axis has been chosen as the direction of  $\tilde{s}_i$ . Of course, this implies that all the  $\tilde{s}_i$  have the same direction. Such assumption means that there is no phase velocity walk-off among the different waves. This is, anyway, not a bad assumption, as a minimal phase velocity walkoff is necessary for any reasonable strong interaction among the waves. A further simplifying assumption is made that  $\tilde{e}_i \approx \tilde{d}_i$ , which implies weak anisotropy. However, since the main effect of energy walkoff has been taken into account by including the  $(x - \rho_i z)$  terms in Eq.(1.33), the assumptions of all  $\tilde{e}_i$  and  $\tilde{d}_i$  vectors being in the same direction, and all  $\tilde{k}_i$  also being in the same direction should be acceptable. One last assumption needs to be made before we can proceed. It is to assume that

$$\nabla \times \nabla \times \tilde{E} = -\nabla^2 \tilde{E}, \quad (1.34)$$

in Eq.(1.26), ignoring the  $\nabla(\nabla \cdot \tilde{E})$  term. However, the effect of this term is of minor order in the final equation, but the analysis will be much simplified if it is ignored. The influence of the effects of this term are well understood or have at least been discussed in details; discussions on it can be found in [6, 11, 12, 13].

The derivation follows by substituting Eqs.(1.17) & (1.34) into Eq.(1.26), together with the simplifying assumptions on the vector directions, we get the following scalar equation:

$$\frac{\partial^2 E_s}{\partial z^2} + \frac{\partial^2 E_s}{\partial x^2} + \frac{\partial^2 E_s}{\partial y^2} + \frac{\omega^2}{c^2} \epsilon(y) E_s +$$

$$\frac{\omega_s^2}{c^2} \chi^{(n)}(\omega_s; \omega_1, \dots, \omega_n) E_1 \cdots E_n \exp(i \Delta k z) = 0, \quad (1.35)$$

where  $E_s$  denotes the electric field at the sum frequency  $\omega_s$ ; i. e.,  $\omega_s = \sum_{j=1}^n \omega_j$ .  $\Delta k$  is the wave vector mismatch parameter ( $\Delta k = \sum_{j=1}^n k_j - k_s$ ). Note also that the  $y$ -dependence of the permittivity has been explicitly expressed as  $\epsilon(y)$  to indicate that the linear refractive index variation of the slab waveguide is in the  $y$ -direction only; i. e., the core-cladding interfaces are parallel to the  $Oxz$ -plane.

We then further assume that the thickness of the slab waveguide is much smaller than the soliton width. Thus, we can solve Eq.(1.35) by the method of separation of variables [7, 10]:

$$E_i(x, y, z) = F_i(y) A_i(x, z). \quad (1.36)$$

Substituting Eq.(1.36) into Eq.(1.35) gives

$$\begin{aligned} & F_s \frac{\partial^2 A_s}{\partial z^2} + F_s \frac{\partial^2 A_s}{\partial x^2} + A_s \left[ \frac{\partial^2 F_s}{\partial y^2} + \frac{\omega_s^2}{c^2} \{ \epsilon_s(y) - \epsilon_{eff} \} F_s \right] \\ & + \frac{\omega_s^2}{c^2} \epsilon_{eff} F_s A_s + \frac{\omega_s^2}{c^2} \chi^{(n)} F_1 F_2 \cdots F_n A_1 A_2 \cdots A_n \exp(i \Delta k z) = 0, \end{aligned} \quad (1.37)$$

where  $\epsilon_{eff}$  is a separation variable, which corresponds to the square of the bound mode effective refractive index.

Then, I would make use of the fact that spatial solitons are the result of a balance between diffraction and nonlinearity; thus, the terms corresponding to diffraction and nonlinearity are of the same order. Also, it is a fact that the variation of the linear refractive index due to doping to form the slab waveguide is much larger than the refractive index change due to nonlinearity. Thus, we can apply a scaling that the terms within the square brackets in Eq.(1.37) are of order  $\varepsilon$ , while the terms outside the square brackets are of order  $\varepsilon^2$ .  $\varepsilon$  is a small number used as a reference

for scaling. So, Eq.(1.37) can be separated into two equations:

$$\frac{\partial^2 F_s}{\partial y^2} + \frac{\omega_s^2}{c^2} \{ \epsilon_s(y) - \epsilon_{eff} \} F_s = 0, \quad (1.38)$$

and

$$F_s \frac{\partial^2 A_s}{\partial z^2} + F_s \frac{\partial^2 A_s}{\partial x^2} + \epsilon_{eff} \frac{\omega_s^2}{c^2} F_s A_s + \frac{\omega_s^2}{c^2} \chi^{(n)} F_1 F_2 \cdots F_n A_1 A_2 \cdots A_n \exp( -i \Delta k z ) = 0. \quad (1.39)$$

Eq.(1.38) is the famous scalar wave equation in Linear Optics Theory. The solution of this equation for various refractive index profiles are well-known, and can be found in, e. g. [11, 14].

In Eq.(1.39), the  $\partial^2 A_s / \partial z^2$  term can be expanded as

$$\frac{\partial^2 A_s}{\partial z^2} = 2ik_s \frac{\partial A_s}{\partial z} - 2ik_s \rho_s \frac{\partial A_s}{\partial x} - k_s^2 A_s - \rho_s \frac{\partial^2 A_s}{\partial x \partial z} + \frac{\partial^2 A_s}{\partial z^2}. \quad (1.40)$$

The  $k_s^2 A_s$  term cancels with the  $\epsilon_{eff} \frac{\omega_s^2}{c^2} F_s A_s$  term in Eq.(1.39) because of the linear dispersion relation. By invoking the slowly varying envelope approximation, the last two terms in Eq.(1.40) can be ignored. To get further simplification, we confine ourselves to consider only fundamental bound mode solution to Eq.(1.38),  $F_s(y)$ , which is also normalized to satisfy  $\int_{-\infty}^{\infty} F_s dy = 1$ . This enables us to integrate out the dependence on  $y$  from Eq.(1.39) to finally obtain

$$2ik_s \frac{\partial A_s}{\partial z} - 2ik_s \rho_s \frac{\partial A_s}{\partial x} + \frac{\partial^2 A_s}{\partial x^2} + \frac{\omega_s^2}{c^2} \chi_s^{(n)} Q_{eff} A_1 A_2 \cdots A_n \exp( -i \Delta k z ) = 0, \quad (1.41)$$

where  $Q_{eff}$  is the effective modal overlap integral which is defined as

$$Q_{eff} = \frac{\int_{-\infty}^{+\infty} F_1 F_2 \cdots F_n dy}{\int_{-\infty}^{+\infty} F_s^2 dy}. \quad (1.42)$$

For a slab waveguide with translational invariant structure along the  $z$ -direction,  $Q_{eff}$  is simply a constant.

For an  $n$ -th order nonlinearity, Eq.(1.41) will give a system of  $(n + 1)$  equations; each for one of the  $(n + 1)$  member waves participating in the nonlinear wave mixing process. Since we are especially interested in the parametric wave interaction in a quadratically nonlinear medium, as in the last section, I write down here the system of the three equations:

$$\begin{aligned}
2ik_1 \frac{\partial A_1}{\partial z} & \quad 2ik_1 \rho_1 \frac{\partial A_1}{\partial x} + \frac{\partial^2 A_1}{\partial x^2} + \frac{\omega_1^2}{c^2} \chi_1^{(2)} Q_{eff} A_3 A_2^* \exp(-i\Delta kz) = 0 \\
2ik_2 \frac{\partial A_2}{\partial z} & \quad 2ik_2 \rho_2 \frac{\partial A_2}{\partial x} + \frac{\partial^2 A_2}{\partial x^2} + \frac{\omega_2^2}{c^2} \chi_2^{(2)} Q_{eff} A_3 A_1^* \exp(-i\Delta kz) = 0 \\
2ik_3 \frac{\partial A_3}{\partial z} & \quad 2ik_3 \rho_3 \frac{\partial A_3}{\partial x} + \frac{\partial^2 A_3}{\partial x^2} + \frac{\omega_3^2}{c^2} \chi_3^{(2)} Q_{eff} A_1 A_2 \exp(+i\Delta kz) = 0
\end{aligned} \tag{1.43}$$

### 1.4.2 Normalization

It is convenient and also is a usual practice to reduce equations such as Eq.(1.41) to normalized form. Instead of doing it on the more general Eq.(1.41), I will normalize Eqs.(1.43) instead, with the two FH waves degenerate; i. e. the SHG case with  $A_1 = A_2$ ,  $k_1 = k_2$ , and  $\omega_1 = \omega_2$ . Moreover, I consider  $\rho_1 = \rho_2 = \rho_3$ , which is the case considered in the following three chapters (with the exception that dual waveguide systems are considered there, so that linear coupling between waves in the two waveguides is also considered). Eqs. (1.43) become

$$\begin{aligned}
2ik_1 \frac{\partial A_1}{\partial z} & \quad 2ik_1 \rho \frac{\partial A_1}{\partial x} + \frac{\partial^2 A_1}{\partial x^2} + \frac{\omega_1^2}{c^2} \chi_1^{(2)} Q_{eff} A_3 A_1^* \exp(-i\Delta kz) = 0 \\
2ik_3 \frac{\partial A_3}{\partial z} & \quad 2ik_3 \rho \frac{\partial A_3}{\partial x} + \frac{\partial^2 A_3}{\partial x^2} + \frac{\omega_3^2}{c^2} \chi_3^{(2)} Q_{eff} A_1^2 \exp(+i\Delta kz) = 0
\end{aligned} \tag{1.44}$$

where

$$\Delta k = 2k_1 - k_3$$

$$k_3 \approx 2k_1$$

Normalization for other nonlinear wave mixing processes can be done similarly. To do the normalization, I need to define several new parameters:

$$z_d = k_1 r_o^2 \quad (1.45)$$

where  $z_d$  is the diffraction (diffusion) length and  $r_o$  is the beam size.

$$\beta_3 = 2\beta_1 + \Delta k \quad (1.46)$$

where  $\beta_1$  is the nonlinearity induced phase velocity shift for wave 1.

$$\begin{aligned} K_1 &= \frac{\omega_1^2}{2k_1 c^2} \chi_1^{(2)} Q_{eff} \\ K_3 &= \frac{\omega_3^2}{k_1 c^2} \chi_3^{(2)} Q_{eff} \end{aligned} \quad (1.47)$$

Then, I make the following variable transformations [8]:

$$\begin{aligned} \zeta &= \frac{\beta_3}{z_d} z \\ s &= \frac{\sqrt{\beta_3}}{r_o} x \\ A_1 &= \frac{\beta_3}{k_1 \sqrt{K_1 K_3} r_o^2} u \exp\left(i \frac{1}{2} \beta_1 \tilde{z}\right) \\ A_3 &= \frac{\beta_3}{k_1 K_1 r_o^2} v \exp\left(i \frac{1}{2} \beta_3 \tilde{z}\right) \end{aligned} \quad (1.48)$$

where  $\tilde{z}$  is the scaled  $z$  with respect to the diffraction length  $z_d$ ; i. e.  $\tilde{z} = z/z_d$ .

With the variable transformations, the normalized equations of Eqs. (1.44) will be

$$\begin{aligned} i \frac{\partial u}{\partial \zeta} - i \delta \frac{\partial u}{\partial s} + \frac{1}{2} \frac{\partial^2 u}{\partial s^2} - qu + u^* v &= 0 \\ 2i \frac{\partial v}{\partial \zeta} - 2i \delta \frac{\partial v}{\partial s} + \frac{1}{2} \frac{\partial^2 v}{\partial s^2} - v + \frac{1}{2} u^2 &= 0 \end{aligned} \quad (1.49)$$

where

$$\delta = \frac{\rho k_1 r_o}{\sqrt{\beta_3}} \quad (1.50)$$

is the walkoff parameter, and

$$q = \frac{\beta_1}{2\beta_3} \quad (1.51)$$

is the phase mismatch parameter.

After deriving the normalized modelling equations for the nonlinear wave mixing process in quadratically nonlinear medium, we will go to investigate individual system configurations in the following chapters.

# Chapter 2

## Closely Coupled $\chi^{(2)}$ Waveguides

### 2.1 Introduction

The use of nonlinear twin-core fibre couplers as very fast optical switches have received keen research interest in recent years, after the pioneering work by Jensen [15]. However, Jensen's theoretical treatment of nonlinear coupled mode equations applied only to quasi-CW cases, because the time variable was not included. Thus, it is not applicable to describe pulse switching, especially soliton switching in the coupler.

Solitons in a dual-core fiber (directional coupler) with *cubic* ( $\chi^{(3)}$ ) nonlinearity were considered in a number of theoretical studies (see, e.g., Refs. [16]-[24]). An important feature of these solitons is that they have two components, which renders their dynamics richer than those in the single-component systems. In [17, 23], they investigated the coupled nonlinear Schrödinger equations with an variational approximation. It was found that a bifurcation occurred, and both symmetric and asymmetric soliton solutions co-existed. The bifurcation was subcritical and the

coupler showed a strong and easily controlled bistability. In [21], a detailed study was also undertaken on the stability of the soliton states for a nonlinear fiber coupler. Stability below and above the bifurcation point for symmetric, asymmetric and antisymmetric soliton states was characterized. On the other hand, saturable nonlinear couplers were studied in [22], and it was shown that the saturation of nonlinearity can cause the stability of stationary states to change. In [24], the nonlinear fiber coupler was considered as a Hamiltonian dynamical system, and numerical simulations were used to study the propagation dynamics of ultrashort soliton pulses. When polarization effect was taken into account, a model of two coupled nonlinear optical fibers with two polarizations, which were either linear or circular, in each fiber was considered in [25]. The interaction of soliton pulses and their stability in a nonlinear directional coupler were investigated in [26], using a perturbation theory based on a two-soliton system. To control the switching of soliton pulse, a method which makes use of a weak control pulse was introduced in [27]. Sharp switching characteristics can be obtained by varying the peak power or the phase of the weak pulse.

In the studies of materials with quadratic nonlinearity, there had been a lot of works in second harmonic generation, achieving phase matching by various means, such as using multiple layers [28]-[30], using an adsorbative layer with/without grating enhancement [31]-[33], using the quasi-phase matching technique [34, 35], or using the anomalous dispersion phase matching technique [36].

With respect to solitons in a dielectric medium with the quadratic nonlinearity, it has been demonstrated that such a medium can display self-focusing phenomena too, either by the cascading effect or not, which generates soliton by the mutual trapping of the fundamental and second-harmonic waves [37]-[40]. Experimentally,

observations of spatial solitary waves in quadratically nonlinear medium were made in both one-dimensional [41] and two-dimensional [42] cases.

However, since the surge of investigations in waveguides with quadratic nonlinearity, there had been just several works, which studied coupling effects in such medium [43]-[45]. In [45], coupling effects were studied between a quadratically nonlinear waveguide and a linear one. In [46], the pulse evolution in coupled waveguides with mixed quadratic-cubic nonlinearity was investigated. However, solitons were not considered in these investigations.

In this chapter, I will discuss the investigation of solitons in two linearly coupled quadratically nonlinear waveguides. Here, we will consider the simplest case, when the two waveguides are identical, and closely spaced, and the beams in them are strictly parallel. The cases when the two waveguides are non-identical, or when the beams are not parallel, will be considered in later chapters.

## 2.2 Mathematical Model

Equations describing copropagation of the fundamental harmonic (FH)  $u$  and second harmonic (SH)  $v$  in the coupled waveguides are as follows:

$$\begin{aligned}
 i\frac{\partial u_1}{\partial z} + i\delta\frac{\partial u_1}{\partial x} + \frac{1}{2}\frac{\partial^2 u_1}{\partial x^2} \quad qu_1 + u_1^*v_1 &= Qu_2, \\
 2i\frac{\partial v_1}{\partial z} + 2i\delta\frac{\partial v_1}{\partial x} + \frac{1}{2}\frac{\partial^2 v_1}{\partial x^2} \quad v_1 + \frac{1}{2}u_1^2 &= Kv_2, \\
 i\frac{\partial u_2}{\partial z} \quad i\delta\frac{\partial u_2}{\partial x} + \frac{1}{2}\frac{\partial^2 u_2}{\partial x^2} \quad qu_2 + u_2^*v_2 &= Qu_1, \\
 2i\frac{\partial v_2}{\partial z} \quad 2i\delta\frac{\partial v_2}{\partial x} + \frac{1}{2}\frac{\partial^2 v_2}{\partial x^2} \quad v_2 + \frac{1}{2}u_2^2 &= Kv_1,
 \end{aligned} \tag{2.1}$$

where the subscripts 1 and 2 pertain to the first and second waveguides,  $z$  and  $x$  being the propagation and the transverse coordinates in the waveguides, and  $\delta$

is the walkoff parameter (which we will consider to be zero in this chapter). The second derivative terms account for the diffraction; the nonlinear terms account for the FH-SH conversion. The parameter  $q$  measures the phase mismatch between the two harmonics, which, for the simplest case considered in this chapter, takes on the value of 1 for the fully matched case. Please refer to the last section of Chapter 1 for definitions of  $\delta$  and  $q$ . Note that the other frequently used mismatch parameter  $\alpha$ , defined as a coefficient in the equation for SH [38, 47], is just  $q^{-1}$ . These four equations can be derived from the Maxwell's Equations, similar to what I showed in the previous chapter for Eq. (1.45). Thus, the derivation from the Maxwell's Equations will not be elaborated again here. The only difference is the terms on the right-hand sides of the equations, which represent the linear coupling between the waveguides.  $Q$  and  $K$  are respectively the FH and SH coupling constants. The derivation of the general form of these coupling terms from the coupled mode theory can be found easily in some famous references; e.g., [11, 14]. Note that a supermode analysis leading to such expressions is exact, *provided* that the fields  $u_{1,2}$  and  $v_{1,2}$  are *superposition fields*, which are modes of the compound coupler structure consisting of both waveguides as a unit (see Chapter 6 of [14]). However, in most cases, these superposition fields are too complicated to find. In the investigations of this thesis, as in most other investigations by other researchers, the superposition fields are approximated by the mode fields of each individual waveguide. For such an approximation to be accurate, a basic assumption is that the two waveguides are not too closely spaced such that the contribution of one waveguide to the field at the centre of the second waveguide is small (see Section 18-11 of [11]).

If these coupling terms are derived using perturbation theory, this assumption is also needed because the second waveguide is treated as a perturbation of the

first fiber [48, 49]. In [49], there are detailed discussions of the derivation of the form of these terms, and the other assumptions needed for the derivation. Since the derivation is far afield from what is discussed here, and the derivation starting from the Reciprocity Theorem [49] is too lengthy, it is not repeated here.

Since the frequency of the SH waves is double that of the FH waves, the waveguide parameter  $V$  of the SH waves is larger, and thus the SH waves are more tightly bounded than the FH waves. Thus, the FH coupling constant  $Q$  is always larger than the SH coupling constant  $K$ . When the two waveguides are widely separated, since the fields fall off exponentially outside the cores and the SH waves are more tightly bounded, the SH field coupling will be negligible while there is still appreciable coupling between the FH fields. So, we can put  $K = 0$  for the widely separated core case. When the waveguides get close together, the overlap integral of the SH fields will increase and approach that of the FH fields; so the coupling constant of the SH fields will approach the coupling constant of the FH fields. Thus, in the limit, we can put  $K = Q$  for the closely spaced core case.

Note that coupling is also possible when  $u_1$  and  $u_2$  (or  $v_1$  and  $v_2$ ) have opposite signs (polarity), these cases are taken care of by  $Q$  (or  $K$  respectively) taking on negative values.

## 2.3 Stationary Solutions

The investigation of the coupled system presented here is carried out by first establishing its stationary solutions. Then, its stability is studied. This will be the topic to be discussed in later section.

To seek for the stationary solution, the  $z$ -derivative terms (the first terms) in

Eqs. (2.1) are set to zeros. As a first step to analyze this system, we will, in this chapter, ignore the walkoff terms, and assume no phase mismatch, viz., by putting  $q = 1$ . Also, we consider the important case of closely placed waveguides, which implies the coupling constants for the FH and SH are approximately equal, viz.,  $K = Q$ . These restrictions will be removed in later chapters. As such, Eqs. (2.1) will be simplified to the following equations:

$$\begin{aligned}
\frac{1}{2} \frac{\partial^2 u_1}{\partial x^2} \quad u_1 + u_1^* v_1 &= Q u_2, \\
\frac{1}{2} \frac{\partial^2 v_1}{\partial x^2} \quad v_1 + \frac{1}{2} u_1^2 &= Q v_2, \\
\frac{1}{2} \frac{\partial^2 u_2}{\partial x^2} \quad u_2 + u_2^* v_2 &= Q u_1, \\
\frac{1}{2} \frac{\partial^2 v_2}{\partial x^2} \quad v_2 + \frac{1}{2} u_2^2 &= Q v_1.
\end{aligned} \tag{2.2}$$

All the variables can then be assumed real. It can be checked further that Eqs. (2.2) allow the substitution

$$v_{1,2} = \pm u_{1,2} / \sqrt{2}, \tag{2.3}$$

where the sign is the same for both values of the subscript. Then, there remains two equations,

$$\begin{aligned}
\frac{1}{2} \frac{\partial^2 u_1}{\partial x^2} \quad u_1 + \frac{1}{\sqrt{2}} u_1^2 + Q u_2 &= 0, \\
\frac{1}{2} \frac{\partial^2 u_2}{\partial x^2} \quad u_2 + \frac{1}{\sqrt{2}} u_2^2 + Q u_1 &= 0.
\end{aligned} \tag{2.4}$$

The stationary solutions were found by two separate methods. First, they were found approximately, using the variational analysis (VA) approach. Then, they would be found by direct numerical approach; the numerical method used here was the shooting method.

### 2.3.1 Variational Analysis

To study the problem using the variational analysis (VA), we make use of the Hamilton's principle which states that the action given by the time integral of the Lagrangian takes the extremum. For the infinite dimension problem such as given by our system of modelling equations (2.4), Hamilton's principle is extended to the extremum of the action given by the Lagrangian density  $\mathcal{L}$  which is a real function of the fields  $u_1$ ,  $u_2$ , and also their derivatives,

$$\delta \int \mathcal{L}(u_1, u_{1x}, u_{1xx}, u_2, u_{2x}, u_{2xx}, \dots) dx = 0. \quad (2.5)$$

Note that the variable  $x$  here takes the role of 'time' in applications in classical mechanical problems. Also,  $\delta$  is used here to stand for the variational operator instead of representing the walkoff parameter, which is put to zero in this chapter.

The variation in (2.5) is defined by

$$\begin{aligned} & \delta \int_{-\infty}^{+\infty} \mathcal{L} dx \\ \equiv & \lim_{\epsilon \rightarrow 0} \frac{1}{\epsilon} \int_{-\infty}^{+\infty} \left\{ \mathcal{L}(u_1 + \epsilon(\delta u_1), u_2 + \epsilon(\delta u_2), \dots, u_{1xx} + \epsilon(\delta u_{1xx}), \dots) \right. \\ & \left. \mathcal{L}(u_1, u_2, \dots, u_{1xx}, \dots) \right\} dx \end{aligned} \quad (2.6)$$

Since we are considering soliton solutions, we can assume the variations  $\delta u_1$ , and  $\delta u_2$  etc. to vanish at the boundaries of the integration. As usual, we make use of the facts that  $\delta u_{1x} = \partial(\delta u_1)/\partial x$ , etc.. Then, after taking the integration by parts, Eq. (2.5) becomes

$$\int \sum_{n=0}^{\infty} \left\{ (-1)^n \frac{\partial^n}{\partial x^n} \frac{\partial \mathcal{L}}{\partial u_{1nx}} + (-1)^n \frac{\partial^n}{\partial x^n} \frac{\partial \mathcal{L}}{\partial u_{2nx}} \right\} dx = 0 \quad (2.7)$$

where  $u_{1nx} \equiv \partial^n u_1 / \partial x^n$  etc.. (Note that, in the system considered here,  $n$  can only be up to 2 because the second derivative terms are the highest derivatives

in Eqs. (2.4).) Since the variations  $\delta u_1$ , and  $\delta u_2$  are taken to be arbitrary and independent, we have, separately,

$$\begin{aligned}\frac{\delta \mathcal{L}}{\delta u_1} &\equiv \sum_{n=0}^2 (-1)^n \frac{\partial^n}{\partial x^n} \frac{\partial \mathcal{L}}{\partial u_{1nx}} = 0 \\ \frac{\delta \mathcal{L}}{\delta u_2} &\equiv \sum_{n=0}^2 (-1)^n \frac{\partial^n}{\partial x^n} \frac{\partial \mathcal{L}}{\partial u_{2nx}} = 0\end{aligned}\quad (2.8)$$

To construct the Lagrangian density  $\mathcal{L}$ , it should be such that Eqs. (2.8) will give the two modelling equations (2.4). So, the Lagrangian density of the system of Eqs. (2.4) is:

$$\mathcal{L} = \frac{1}{4} \left[ (u_1')^2 + (u_2')^2 \right] - \frac{1}{2} (u_1^2 + u_2^2) + \frac{1}{3\sqrt{2}} (u_1^3 + u_2^3) + Q u_1 u_2; \quad (2.9)$$

where the prime stands for  $d/dx$ .

To apply VA, we need an *ansatz*. To choose a suitable ansatz, we note that Eqs. (2.4) have an obvious symmetric solution, which was found a long time ago [50, 51]:

$$u_1 = u_2 = \frac{3}{\sqrt{2}} (1 - Q) \operatorname{sech}^2 \left( \sqrt{\frac{1}{2}} (1 - Q) x \right), \quad (2.10)$$

Also, we can refer to the VA for the solitons in the dual-core fiber with the cubic nonlinearity [17]. Both suggest us to adopt the following ansatz:

$$\begin{aligned}u_1 &= A \cos \theta \operatorname{sech}^2 \left( \frac{x}{W} \right), \\ u_2 &= A \sin \theta \operatorname{sech}^2 \left( \frac{x}{W} \right),\end{aligned}\quad (2.11)$$

where  $A$ ,  $W$ , and  $\theta$  are respectively the arbitrary amplitude, width, and asymmetry parameter of the solitons sought for.

The next step is to insert the ansatz (2.11) into Eq. (2.9), and calculate the effective Lagrangian,

$$L \equiv \int_{-\infty}^{+\infty} \mathcal{L} dx = \frac{4}{15} A^2 W^{-1} - \frac{2}{3} A^2 W$$

$$\begin{aligned}
& + \frac{16}{45\sqrt{2}} A^3 W (\cos^3 \theta + \sin^3 \theta) \\
& + \frac{2}{3} Q A^2 W \sin(2\theta).
\end{aligned} \tag{2.12}$$

Finally, the equations that determine the unknown parameters  $A$ ,  $W$ , and  $\theta$  are obtained by demanding that the variations of the effective Lagrangian with respect to each of the parameters are zero. This gives three algebraic equations,

$$\frac{2}{15W^2} + \frac{1}{3} - \frac{4}{15} A \sin \psi \left[ 1 + \frac{1}{2} \cos(2\psi) \right] + \frac{Q}{3} \cos(2\psi) = 0, \tag{2.13}$$

$$\frac{2}{15W^2} + \frac{1}{3} - \frac{8}{45} A \sin \psi \left[ 1 + \frac{1}{2} \cos(2\psi) \right] + \frac{Q}{3} \cos(2\psi) = 0, \tag{2.14}$$

$$\frac{4A}{15} \left[ \cos \psi + \frac{1}{2} \cos \psi \cos(2\psi) - \sin \psi \sin(2\psi) \right] + Q \sin(2\psi) = 0, \tag{2.15}$$

where

$$\psi \equiv \theta + \frac{\pi}{4}. \tag{2.16}$$

Eqs. (2.13-2.16) give two different types of solutions. When  $\theta = \pi/4$ , i.e.,  $\psi = \pi/2$ , Eqs. (2.11) implies  $u_1 = u_2$ ; the solutions are for symmetric solitons. It can be shown that Eqs. (2.13)&(2.14) together with the ansatz (2.11) give the exact symmetric solutions given by Eqs. (2.3)&(2.10), and these solutions exist at all  $Q < 1$ .

In the other case, after some algebra, Eqs. (2.13-2.15) will give the asymmetric soliton solutions as,

$$A = 5Q \frac{\sin \psi}{\sin(2\theta)}, \tag{2.17}$$

$$W = \sqrt{\frac{6\zeta}{5Q} (1 - \zeta)^{-1} \left( 1 + \frac{1}{2}\zeta \right)^{-1}}, \tag{2.18}$$

where the auxilliary parameter

$$\zeta = \cos(2\psi) = \frac{5Q}{2Q} \frac{6 + \sqrt{3(12 - 20Q - 5Q^2)}}{2Q}. \tag{2.19}$$

It can be seen that  $\psi$  (or  $\theta$ ) is real only if  $|\zeta| < 1$ . Thus, from Eq. (2.19), asymmetric solution exists in the interval of the coupling constant values,  $Q$ ,

$$1 < Q < \frac{3}{8} \quad (2.20)$$

Comparing with the existence range for symmetric soliton,  $Q < 1$ , it can be seen a *bifurcation* occurs for small  $|Q|$ , and the bifurcation points estimated by VA are at  $-1$  and  $3/8$ . A bifurcation diagram is found in Fig. 2.1.

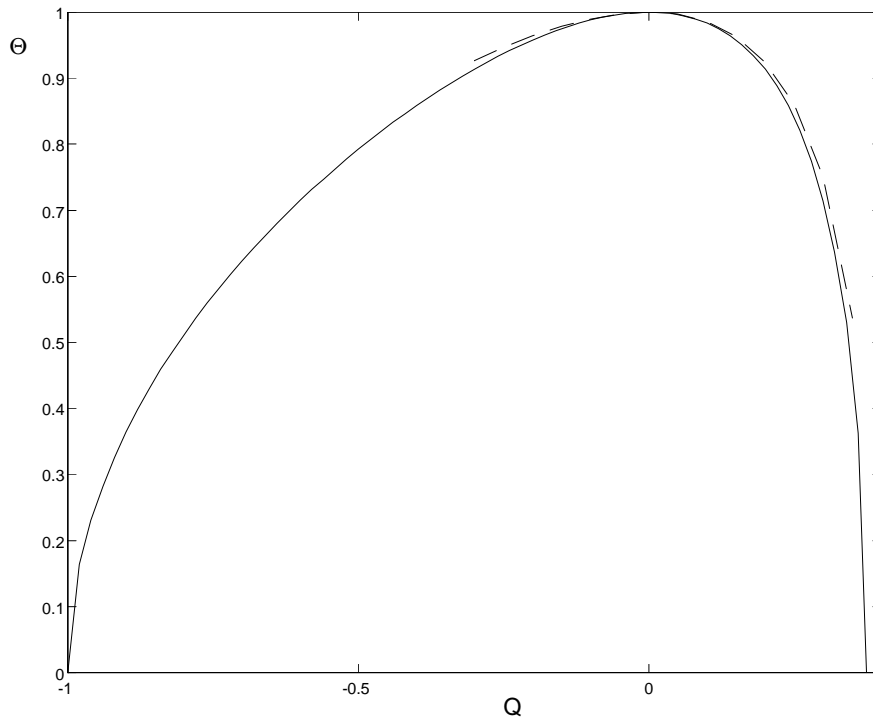


Figure 2.1: The bifurcation diagram of the system (2.4). The dashed line shows the numerically obtained results, while the solid line is from VA.

In Fig. 2.1, the asymmetric parameter  $\Theta$  is defined as:

$$\Theta = \cos 2\theta. \quad (2.21)$$

In Fig. 2.2, plots of the peak values of  $u_1$ ,  $u_2$ ,  $v_1$ , and  $v_2$ ; and in Fig. 2.3 & 2.4, plots of the width,  $W$ , and  $\theta$  versus the control parameter,  $Q$ , are shown.

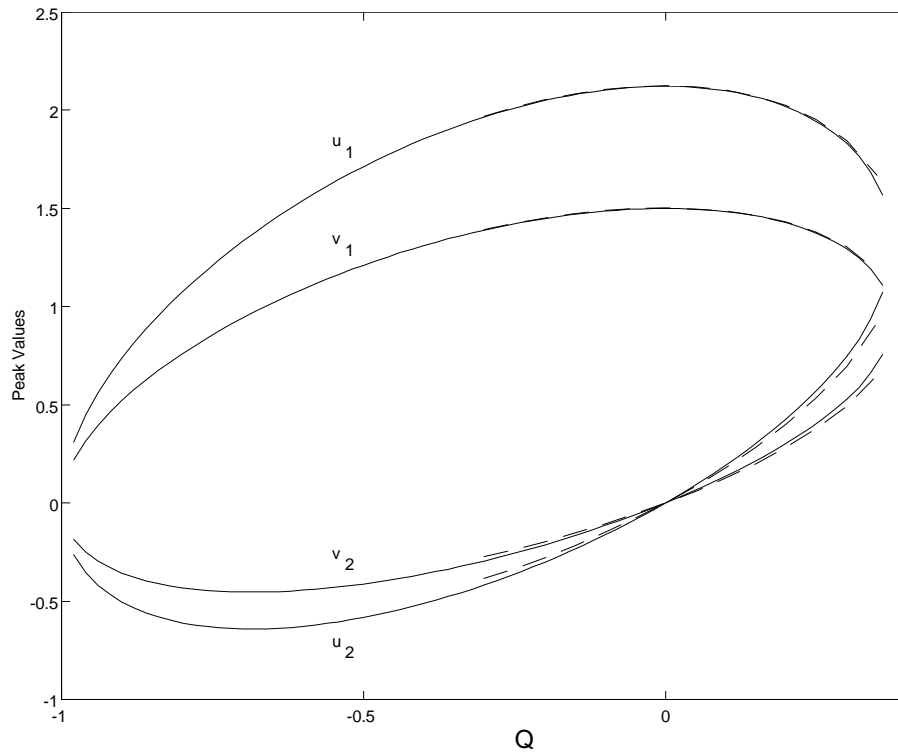


Figure 2.2: The peak values of  $u_1$ ,  $u_2$ ,  $v_1$ , and  $v_2$  versus the control parameter  $Q$ .

In both Figs. 2.2 & 2.3, the dashed lines show the numerically obtained results, while the solid lines are from VA.

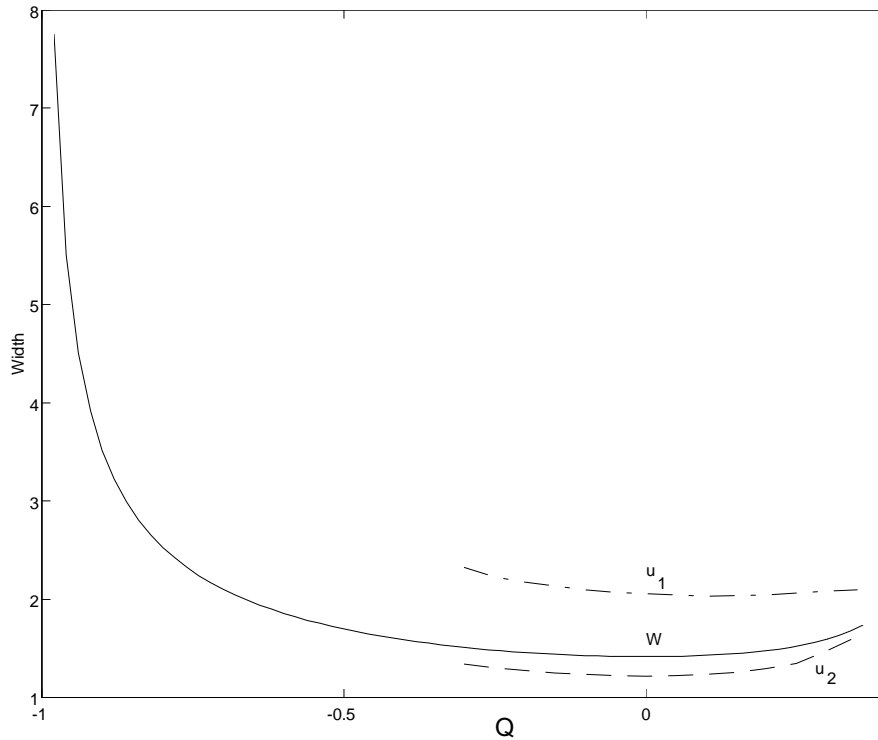


Figure 2.3: The width parameter,  $W$ , cf. Eq. (2.11), versus the control parameter  $Q$ .

From these plots, it can be seen that, at  $Q = 3/8$ ,  $\theta = \pi/4$ , the solution coincides with the exact symmetric solution, given by Eqs. (2.3)&(2.10) for the same value of  $Q$ . At the other bifurcation point,  $Q = -1$ ,  $\theta = \pi/4$ , the variational solution describes an antisymmetric soliton with a vanishing amplitude  $A$  and a diverging width,  $W$ . At  $Q = 0$ ,  $\theta = 0$ , the variational solution goes over into the exact solution for one waveguide, Eqs. (2.3)&(2.10), while in the other waveguide, the field is absent. In Figs. 2.1 to 2.3, the dashed curves are those obtained from direct numerical analysis, which will be discussed later.

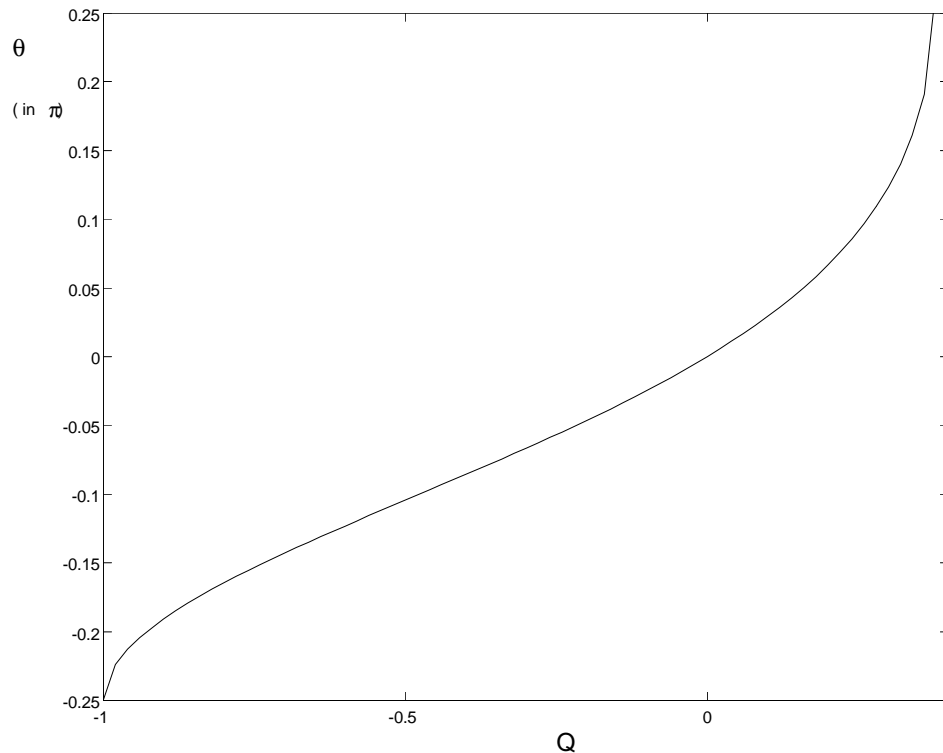


Figure 2.4: The parameter  $\theta$ , cf. Eq. (2.11), versus the control parameter  $Q$ .

### 2.3.2 Zero-mode Analysis

The value of the control parameter  $Q$  at the bifurcation point can be found *exactly* by a zero-mode analysis. A zero-mode analysis is to search for the perturbation eigenmode which will grow at the expense of the symmetric soliton solution to transform into the corresponding asymmetric solution. The point at which the zero-mode begins to appear denotes where the symmetric solution starts to become unstable; thus, this point is the bifurcation point.

We look for an antisymmetric eigenmode perturbation such that

$$\delta u = \delta u_1 = -\delta u_2,$$

$$\delta v = \delta v_1 = \delta v_2. \quad (2.22)$$

These zero mode perturbations need to be antisymmetric so as to imply a transition of the symmetric soliton solution to the asymmetric ones as a consequence of the bifurcation. These perturbations appear on the background of the exact *symmetric* solution of modelling equations, Eqs. (2.2),

$$u_o \equiv u_{1o} = u_{2o} = \frac{3}{\sqrt{2}}(1 - Q)\operatorname{sech}^2\left(\frac{1 - Q}{2}x\right), \quad (2.23)$$

$$v_o \equiv v_{1o} = v_{2o} = \frac{u_o}{\sqrt{2}},$$

cf. Eq. (2.3)&(2.10), so that

$$u_1 = u_o + \delta u,$$

$$u_2 = u_o - \delta u,$$

$$v_1 = v_o + \delta v, \quad (2.24)$$

$$v_2 = v_o - \delta v.$$

Substituting Eqs. (2.24) into Eqs. (2.2), we get two linearized equations for the zero-modes,

$$\frac{1}{2}(\delta u)'' - (1 + Q)\delta u + u_o\delta v + \frac{1}{\sqrt{2}}u_o\delta u = 0,$$

$$\frac{1}{2}(\delta v)'' - (1 + Q)\delta v + u_o\delta u = 0. \quad (2.25)$$

To obtain an exact solution to Eqs. (2.25), we can try the solution in the form

$$\delta u = a \operatorname{sech}^\gamma\left(\sqrt{\frac{1 - Q}{2}}x\right),$$

$$\delta v = b \operatorname{sech}^\gamma\left(\sqrt{\frac{1 - Q}{2}}x\right), \quad (2.26)$$

where  $a, b$ , and  $\gamma$  are unknown parameters to be determined. Direct substitution of Eqs. (2.26) into Eqs. (2.25) leads to

$$\sqrt{\frac{1+Q}{1-Q}} = \frac{3}{2}, \quad (2.27)$$

or  $Q = 5/13$ . Furthermore, it can be deduced that  $b = a/\sqrt{2}$ , and  $a$  is an infinitesimal perturbation amplitude, which can take on arbitrary value. The corresponding value of  $\gamma$  is evaluated to be 3, giving

$$\delta u = \sqrt{2}\delta v = a \operatorname{sech}^3\left(\frac{2}{\sqrt{13}}x\right). \quad (2.28)$$

One can also compare the approximate and exact values of  $Q_{cr}$ , the value of  $Q$  at the bifurcation point, i.e., respectively,  $3/8 = 0.375$  and  $5/13 = 0.3846$ . The relative error of the simple VA in predicting the bifurcation point is just 2.5%, which is quite acceptable.

### 2.3.3 Numerical Check of VA results

In this subsection, I will describe the numerical analysis to find the stationary solution, which serves as a check of the results obtained from the VA. The numerical method adopted is the shooting method; see e.g. [52].

If the solution to the two modelling equations, Eqs. (2.4), is to describe a soliton, it has to be localized. Thus, it will satisfy the boundary conditions that

$$u_1(+\infty) = u_1(-\infty) = 0, \quad \text{and} \quad u_2(+\infty) = u_2(-\infty) = 0. \quad (2.29)$$

So, to obtain a stationary solution numerically for Eqs. (2.4), together with Eqs. (2.29), we need a boundary value problem solver. The shooting method was used here.

Since we are interested in soliton solutions which are even functions, we can reduce the integration domain to just one half, moving the left boundary from

$x = -\infty$  to  $x = 0$ . Since the solution constitutes of even functions, At  $x = 0$ ,  $u_1'(0) = u_2'(0) = 0$ , whereas  $u_1(0)$  and  $u_2(0)$  are unknown. The method is to make a guess of the values of  $u_1(0)$  and  $u_2(0)$ , say,

$$u_1(0) = u_{1g}, \text{ and } u_2(0) = u_{2g} \quad (2.30)$$

and use an initial value integrator to integrate Eqs. (2.4) from  $x = 0$  to a sufficiently large value of  $x$ , say,  $x_r$ . We will then refine the guess of  $u_{1g}$  and  $u_{2g}$  such that

$$u_1(x_r) \approx 0, \text{ and } u_2(x_r) \approx 0. \quad (2.31)$$

The initial value integrator used here was the fourth-order Runge-Kutta method.

To implement the Runge-Kutta method, we need to reduce the ordinary differential equations, Eqs. (2.4), to a first order system,

$$\begin{aligned} u_1' &= w_1 \equiv f_1(u_1, u_2, w_1, w_2), \\ u_2' &= w_2 \equiv f_2(u_1, u_2, w_1, w_2), \\ w_1' &= 2u_1 - \sqrt{2}u_1^2 - 2Qu_2 \equiv f_3(u_1, u_2, w_1, w_2), \\ w_2' &= 2u_2 - \sqrt{2}u_2^2 - 2Qu_1 \equiv f_4(u_1, u_2, w_1, w_2). \end{aligned} \quad (2.32)$$

Then, difference equations are derived for Eqs. (2.32) by replacing the derivatives by differences. For example, the simplest method is to replace, say,  $u_1'$  by  $[u_1(x+h) - u_1(x)]/h$ , where  $h$  is the grid size. The idea of the Runge-Kutta method is to use multiple iterations to get better and better estimates of the slopes, viz.,  $f_1$ ,  $f_2$ ,  $f_3$  and  $f_4$  to be used in the difference equations. The fourth-order Runge-Kutta formulae in [53] was adopted.

For the system of equations, Eqs. (2.32), the set of difference equations used for the numerical integration to progress from the  $k$ -th grid point to the  $(k+1)$ -th grid

point, thus, is

$$\begin{aligned}
s_{11} &= h f_1(u_{1k}, u_{2k}, w_{1k}, w_{2k}), \\
s_{12} &= h f_2(u_{1k}, u_{2k}, w_{1k}, w_{2k}), \\
s_{13} &= h f_3(u_{1k}, u_{2k}, w_{1k}, w_{2k}), \\
s_{14} &= h f_4(u_{1k}, u_{2k}, w_{1k}, w_{2k})
\end{aligned} \tag{2.33}$$

for the first iteration;

$$\begin{aligned}
s_{21} &= h f_1\left(u_{1k} + \frac{1}{2}s_{11}, u_{2k} + \frac{1}{2}s_{12}, w_{1k} + \frac{1}{2}s_{13}, w_{2k} + \frac{1}{2}s_{14}\right), \\
s_{22} &= h f_2\left(u_{1k} + \frac{1}{2}s_{11}, u_{2k} + \frac{1}{2}s_{12}, w_{1k} + \frac{1}{2}s_{13}, w_{2k} + \frac{1}{2}s_{14}\right), \\
s_{23} &= h f_3\left(u_{1k} + \frac{1}{2}s_{11}, u_{2k} + \frac{1}{2}s_{12}, w_{1k} + \frac{1}{2}s_{13}, w_{2k} + \frac{1}{2}s_{14}\right), \\
s_{24} &= h f_4\left(u_{1k} + \frac{1}{2}s_{11}, u_{2k} + \frac{1}{2}s_{12}, w_{1k} + \frac{1}{2}s_{13}, w_{2k} + \frac{1}{2}s_{14}\right)
\end{aligned} \tag{2.34}$$

for the second iteration;

$$\begin{aligned}
s_{31} &= h f_1\left(u_{1k} + \frac{1}{2}s_{21}, u_{2k} + \frac{1}{2}s_{22}, w_{1k} + \frac{1}{2}s_{23}, w_{2k} + \frac{1}{2}s_{24}\right), \\
s_{32} &= h f_2\left(u_{1k} + \frac{1}{2}s_{21}, u_{2k} + \frac{1}{2}s_{22}, w_{1k} + \frac{1}{2}s_{23}, w_{2k} + \frac{1}{2}s_{24}\right), \\
s_{33} &= h f_3\left(u_{1k} + \frac{1}{2}s_{21}, u_{2k} + \frac{1}{2}s_{22}, w_{1k} + \frac{1}{2}s_{23}, w_{2k} + \frac{1}{2}s_{24}\right), \\
s_{34} &= h f_4\left(u_{1k} + \frac{1}{2}s_{21}, u_{2k} + \frac{1}{2}s_{22}, w_{1k} + \frac{1}{2}s_{23}, w_{2k} + \frac{1}{2}s_{24}\right)
\end{aligned} \tag{2.35}$$

for the third iteration;

$$\begin{aligned}
s_{41} &= h f_1(u_{1k} + s_{31}, u_{2k} + s_{32}, w_{1k} + s_{33}, w_{2k} + s_{34}), \\
s_{42} &= h f_2(u_{1k} + s_{31}, u_{2k} + s_{32}, w_{1k} + s_{33}, w_{2k} + s_{34}), \\
s_{43} &= h f_3(u_{1k} + s_{31}, u_{2k} + s_{32}, w_{1k} + s_{33}, w_{2k} + s_{34}), \\
s_{44} &= h f_4(u_{1k} + s_{31}, u_{2k} + s_{32}, w_{1k} + s_{33}, w_{2k} + s_{34})
\end{aligned} \tag{2.36}$$

for the fourth iteration.  $u_{1k}$ ,  $u_{2k}$ ,  $w_{1k}$ ,  $w_{2k}$  are the values of  $u_1$ ,  $u_2$ ,  $w_1$ , and  $w_2$  respectively at the  $k$ -th grid point. Finally, the values  $u_{1(k+1)}$ ,  $u_{2(k+1)}$ ,  $w_{1(k+1)}$ , and  $w_{2(k+1)}$  at the  $(k+1)$ -th grid point are given by:

$$\begin{aligned} u_{1(k+1)} &= u_1 + \frac{1}{6}(s_{11} + 2s_{21} + 2s_{31} + s_{41}) \\ u_{2(k+1)} &= u_2 + \frac{1}{6}(s_{12} + 2s_{22} + 2s_{32} + s_{42}) \\ w_{1(k+1)} &= w_1 + \frac{1}{6}(s_{13} + 2s_{23} + 2s_{33} + s_{43}) \\ w_{2(k+1)} &= w_2 + \frac{1}{6}(s_{14} + 2s_{24} + 2s_{34} + s_{44}) \end{aligned} \quad (2.37)$$

### 2.3.4 Comparison of Results

The variational analysis and the numerical analysis succeeded to find asymmetric solitary wave solutions for the system of two linearly coupled second-harmonic-generating waveguides considered. The agreement between the results obtained by the independent methods is very good. This can be seen in Fig. 2.1, 2.2, & 2.3, where we show plots of the bifurcation diagram, peak values and widths of the asymmetric solitons as a function of the controlling parameter  $Q$ . The solid lines are the predictions from the VA, while the dashed lines show the results from the numerical analysis.

We have directly compared the peak values of the variables  $u_1$  and  $u_2$  for the whole range of the control parameter  $Q$ , as predicted by VA and as given by the shooting method. Within the interval  $0.3 < Q < 0.35$ , they prove to be fairly close. The worst case error is about 8%, which happens at the smaller of the peak values of  $u_1$  and  $u_2$  when they are strongly asymmetric; i.e.,  $Q$  is close to 0. It is interesting to add that, in this case, the larger peak value achieves the best agreement between VA and the shooting method; the error is less than 0.04%.

For Fig. 2.1, to be consistent with the definition in Eq. (2.21), the asymmetry parameter  $\Theta$  for the numerical analysis results is defined as:

$$\Theta = \frac{u_{1m}^2 - u_{2m}^2}{u_{1m}^2 + u_{2m}^2}. \quad (2.38)$$

The agreement between the bifurcation curves as obtained from the VA and the shooting method can be seen to be very good.

From Fig. 2.2, it can be seen that  $u_1$  (and thus also  $v_1$ ) has the maximum peak value, whereas  $u_2$  and  $v_2$  are 0 at  $Q = 0$ . While the peak values approach each other (for FH and SH separately) as  $Q$  increases towards the larger bifurcation point,  $5/13$ ; all the peak values approach 0, as  $Q \rightarrow 1$ . On the other hand, from Fig. 2.3, the widths diverge as  $Q \rightarrow 1$ . Thus, in this limit of  $Q \rightarrow 1$ , the solitons disappear. While the agreements in the peak values of the waves between VA and numerical analyses are good, it can be seen from Fig. 2.3 that the agreement in the widths from the two different analyses is not. (In Fig. 2.3, the dashed and dot-dashed lines show the FWHM widths of the numerical obtained waves  $u_1$  and  $u_2$ .) This is because of a classical difficulty in variational analysis that when hyperbolic secant functions are used as ansatz, only a single width factor can be used for the different waves, which is quite a big drawback of the method, which cannot provide for the fact that the different waves in the system can have different widths.

Very close to the bifurcation point at  $Q = 5/13$ , the shooting method becomes unstable, and easily snaps to produce the symmetric soliton solutions on the symmetric branch, for the same value of  $Q$ . Numerical analyses stopped short before reaching and producing the exact location of the bifurcation point there; thus, the dashed curves in Figs. 2.1 - 2.3 do not end at the bifurcation point at  $Q = 5/13$ , which has been found exactly. However, there is no doubt that the bifurcation takes

place as predicted by VA.

Another point that needs to be mentioned is that for  $Q < 0.3$ , the shooting method has never produced solitary wave solutions. Instead, it generated periodic waves. Since the subject of the work is soliton, and periodic wave are usually unstable, thus, all the dashed curves for numerical results terminate at  $Q = 0.3$  for Figs. 2.1 - 2.3. It has been suspected that another bifurcation is amenable for the termination of the numerically found branch of the asymmetric soliton solution at  $Q$  close to  $0.3$ . However, it has later been found that this phenomenon was just an artifact of the numerical method used, and is not a real reflection of the property of the system. The shooting method became unstable for large negative value of  $Q$ . Thus, in later chapters, the shooting method was abandoned, and another method was used to seek for the stationary solutions. Stationary solutions of asymmetric solitons beyond  $Q < 0.3$  were found by this method; which will be elaborated in the next chapter.

Finally, as a particular example of comparing the results obtained, we display in Fig. 2.5 the VA predicted and numerically found shapes of the asymmetric soliton at  $Q = 0.1$ . The disagreement can be seen largest at around the skirts of the waveforms.

## 2.4 Stability of the Solitons

To verify the stability of the stationary solitons found in the preceding section, direct numerical simulations of the full system of partial differential equations (PDEs) (2.1) was performed. The numerical method adopted was the Split step Fourier method, which is also known as the beam propagation method (BPM). To perform the

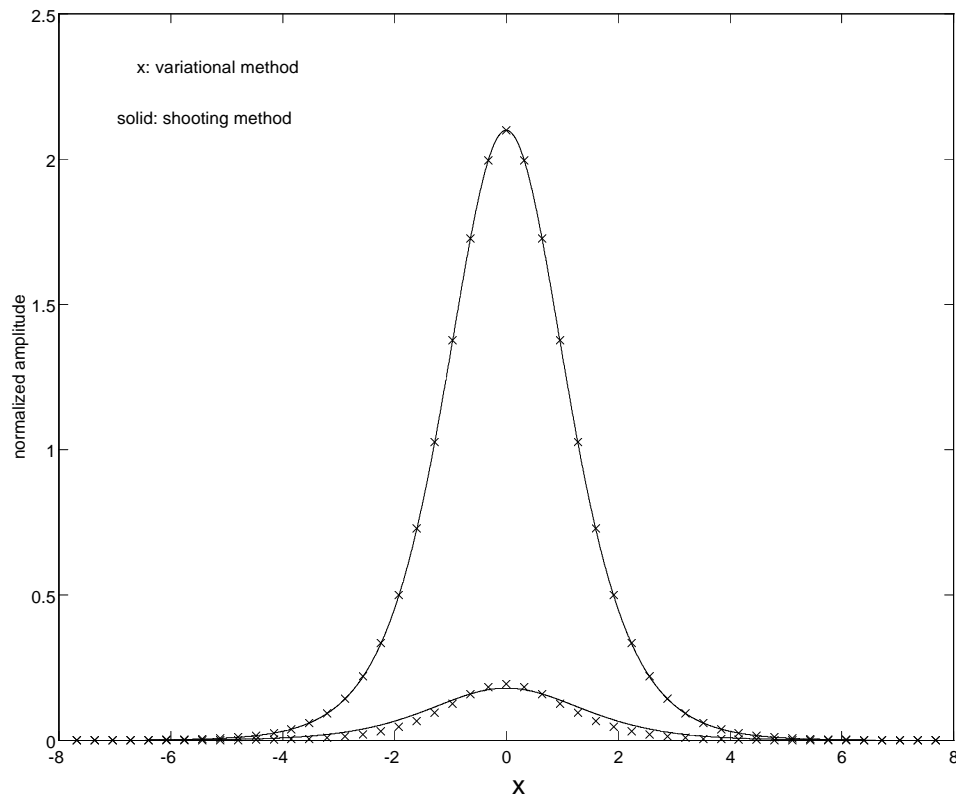


Figure 2.5: The shape of the asymmetric soliton at  $Q = 0.1$ . Shown are the FH components  $u_{1,2}$ : the analytical prediction (crosses) and the results obtained by means of the shooting method (solid).

numerical stability analysis, we use slightly perturbed stationary solutions, which were obtained by means of what was outlined in the previous section, as initial conditions for the BPM simulations. The propagation of these inputs was observed for a sufficient long distance in  $z$ . If there is any large scale change of the slightly perturbed soliton, or perhaps disintegration, its instability is indicated.

### 2.4.1 Beam Propagation Method

The beam propagation method is presently the most widely used tool for the investigation of complex photonic structures. It is a versatile instrument to calculate the wave propagation through optical circuits. It was first proposed [54]-[56] to calculate the propagation of an optical beam through a medium with small variations of the refractive index. The method consists basically of propagating the input beam over a small distance through homogeneous space and then correcting for the refractive index variations seen by this beam during the propagating step, which amounts to the application of the lens law. In nonlinear optics, the beam propagation method has also been adopted to apply to problems for which it was not originally conceived. The propagation equations in nonlinear optics usually do not lend themselves to analytic solutions. Thus, a numerical approach is often necessary. Beam propagation method, which is known as Split step Fourier method in these applications, becomes a popular choice to study the dynamic evolution of nonlinear wave, such as solitons.

The split step Fourier method can be classified to belong to the category of pseudospectral methods. In comparing with finite difference methods, its advantage in speed can be attributed in part to the use of the Fast Fourier Transform (FFT) algorithm.

In general, diffraction (or dispersion) and nonlinearity act together along the length of the waveguide structure in which the optical wave propagates. The basic idea of the Split step Fourier method is by assuming that, over a small distance  $dz$  in which the optical field propagates, the diffraction and nonlinear effects can be pretended to act independently. If the propagation step size  $dz$  is small enough, the

accuracy of the approximate solution so obtained can be quite good. Specifically, the propagation of the optical field in a segment from  $z$  to  $z + dz$  is carried out in two sub-steps. In the first sub-step, the nonlinearity acts alone, and diffraction is ignored; in the second sub-step, diffraction acts alone, and nonlinearity is ignored.

For Eqs. (2.1) the principle amounts to breaking up the equations, for the first sub-step, into

$$i\frac{\partial u_1}{\partial z} + i\delta\frac{\partial u_1}{\partial x} + \frac{1}{2}\frac{\partial^2 u_1}{\partial x^2} = 0, \quad (2.39)$$

$$2i\frac{\partial v_1}{\partial z} + 2i\delta\frac{\partial v_1}{\partial x} + \frac{1}{2}\frac{\partial^2 v_1}{\partial x^2} = 0, \quad (2.40)$$

$$i\frac{\partial u_2}{\partial z} - i\delta\frac{\partial u_2}{\partial x} + \frac{1}{2}\frac{\partial^2 u_2}{\partial x^2} = 0, \quad (2.41)$$

$$2i\frac{\partial v_2}{\partial z} - 2i\delta\frac{\partial v_2}{\partial x} + \frac{1}{2}\frac{\partial^2 v_2}{\partial x^2} = 0. \quad (2.42)$$

For the second sub-step, the remaining parts of Eqs. (2.1) give

$$i\frac{\partial u_1}{\partial z} - qu_1 + u_1^*v_1 + Qu_2 = 0, \quad (2.43)$$

$$2i\frac{\partial v_1}{\partial z} - v_1 + \frac{1}{2}u_1^2 + Kv_2 = 0, \quad (2.44)$$

$$i\frac{\partial u_2}{\partial z} - qu_2 + u_2^*v_2 + Qu_1 = 0, \quad (2.45)$$

$$2i\frac{\partial v_2}{\partial z} - v_2 + \frac{1}{2}u_2^2 + Kv_1 = 0. \quad (2.46)$$

Eqs. (2.39-2.42) can be solved using the Fourier transform method, giving

$$\begin{aligned} u_1(x, z + dz) &= \mathcal{F}^{-1} \exp \left[ i \left( \frac{1}{2} k_x^2 + \delta k_x \right) dz \right] \mathcal{F} u_1(x, z), \\ v_1(x, z + dz) &= \mathcal{F}^{-1} \exp \left[ i \left( \frac{1}{4} k_x^2 + \delta k_x \right) dz \right] \mathcal{F} v_1(x, z), \\ u_2(x, z + dz) &= \mathcal{F}^{-1} \exp \left[ i \left( \frac{1}{2} k_x^2 - \delta k_x \right) dz \right] \mathcal{F} u_2(x, z), \\ v_2(x, z + dz) &= \mathcal{F}^{-1} \exp \left[ i \left( \frac{1}{4} k_x^2 - \delta k_x \right) dz \right] \mathcal{F} v_2(x, z), \end{aligned} \quad (2.47)$$

where  $k_x$  is the Fourier space variable conjugated to  $x$ ;  $\mathcal{F}$  and  $\mathcal{F}^{-1}$  are, respectively, the direct and inverse Fourier transform operators, which are implemented numerically using the FFT algorithm.

For the second sub-step, Eqs. (2.43-2.46) are ordinary differential equations (ODEs) and were solved numerically in this work using a third order Runge-Kutta scheme. The integration of Eqs. (2.43-2.46) completes a single propagation step of  $dz$ , and the two sub-step procedure can then repeated to cover the whole propagation length of the waveguide structure under investigation.

In the actual implementation of this procedure, there is a slight modification of the procedure outlined above. Instead of including the nonlinearity sub-step at the segment boundary, its effect is included in the middle of each segment. So, in summary, the propagation in each segment is first carried out for half  $dz$  of the diffraction sub-step. Then, it is followed by the propagation of the whole  $dz$  nonlinear sub-step, and is finally completed by the remaining half  $dz$  diffraction sub-step. The reason for adopting this modification is that accuracy can be greatly improved. (See the discussion in [57].)

### 2.4.2 Error Analysis

As a characteristic of  $\chi^{(2)}$  systems, the evolution of perturbed optical field will exhibit conspicuous internal vibrations [58, 59], which may be difficult to differentiate from those introduced by the global errors due to, e.g., using excessively coarse step size in the numerical scheme. Thus, an error analysis was performed to identify and characterize any global errors (mainly discretization errors) and artifacts that may be introduced by the numerical schemes.

As it was long established that, for a single waveguide case (which corresponds to  $Q = 0$  in our system), an exact stable analytical soliton solution exists [50, 51]. Thus, it is convenient to do the error analysis here at  $Q = 0$ , where the characteristic of the real system is known. There are two main parameters for the numerical Split step Fourier method, viz., the number of FFT points in doing the Fourier transform steps, and the propagation step size  $dz$ . So, the error analysis was done with respect to these two parameters.

BPM simulation runs were first performed for 4 different choices of the number of FFT points: 256, 512, 1024, and 2048 points, with a propagation distance of  $\pi$ . It was observed that, other than the 256 point FFT simulation which showed distortion of the optical waveforms, which developed into vibrations, FFT simulations with the other 3 larger number of FFT points produced very similar results, showing stable propagation of the exact analytical solution inputs. Thus, it can be concluded that using 1024 FFT points should give quite accurate simulation results, with still an acceptable high speed of computer runs.

Then, BPM simulation runs were performed for a propagation distance of  $\pi/2$ , when the propagation step size  $dz$  was varied from 0.05 to 0.0001. For  $dz = 0.05$ , the evolution of the exact analytical soliton solution developed into vibrations, which showed that such a coarse step size will introduce instability into the numerical scheme. Thus, finer step size should be used. For finer step sizes, there were no conspicuous difference in the results, showing no internal vibration of the exact analytical solution. However, they all showed a drooping of the peak values as the waves propagate, indicating a global error introduced by the numerical scheme. This drooping of the peak value, nevertheless, is smaller and smaller when the step size  $dz$  gets finer and finer. In Fig. 2.6, a plot of the fractional drooping error introduced

by the finite step size as a function of the step size  $dz$  (in base 10 logarithmic scale) was shown. The slope of the error curve is about  $-1$ , showing that the error due to the step size  $dz$  is of the order of  $\mathcal{O}(dz)$ . With an idea of the global error which can be introduced, simulation runs were performed with either a step size of 0.0005 or 0.001 (for probing runs). Use of the more accurate finer step size of 0.0001 was prohibited by the excessive lengthy simulation time needed.

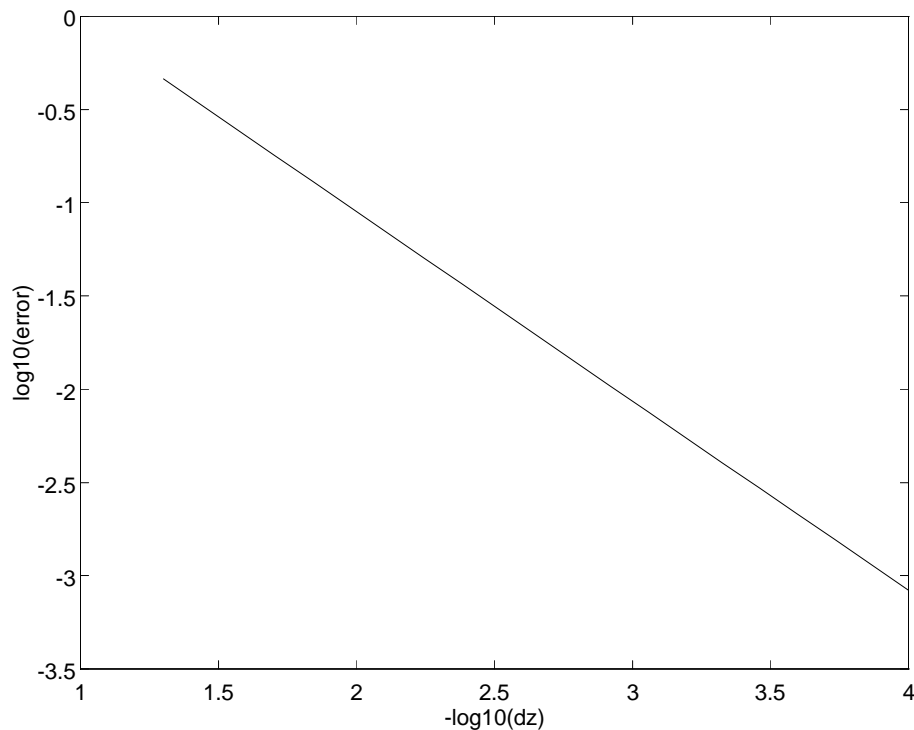


Figure 2.6: The fractional drooping error introduced by the finite step size as a function of the step size  $dz$  (in log scale).

### 2.4.3 Stability of the Asymmetric and Symmetric Solitons

With the potential errors that may be introduced by the numerical method characterized, it is ready to investigate the stability of the stationary soliton solutions

found in the last section. The initial conditions used in the PDE simulations of the solitons were slightly different from the stationary solutions found by the shooting method: the peak values of the waves were taken as given by the shooting method, but for the pulse shapes, the VA analytical expressions, Eqs. (2.11) were used. The aim in choosing the initial conditions in this mixed form was twofold: first, it is much easier to insert the initial conditions into the numerical code when they are known in an analytical form; second, a small deviation of the initial conditions from the (practical) exact solitary-wave shape generated by the shooting method seeds a small perturbation which is necessary to observe the dynamics.

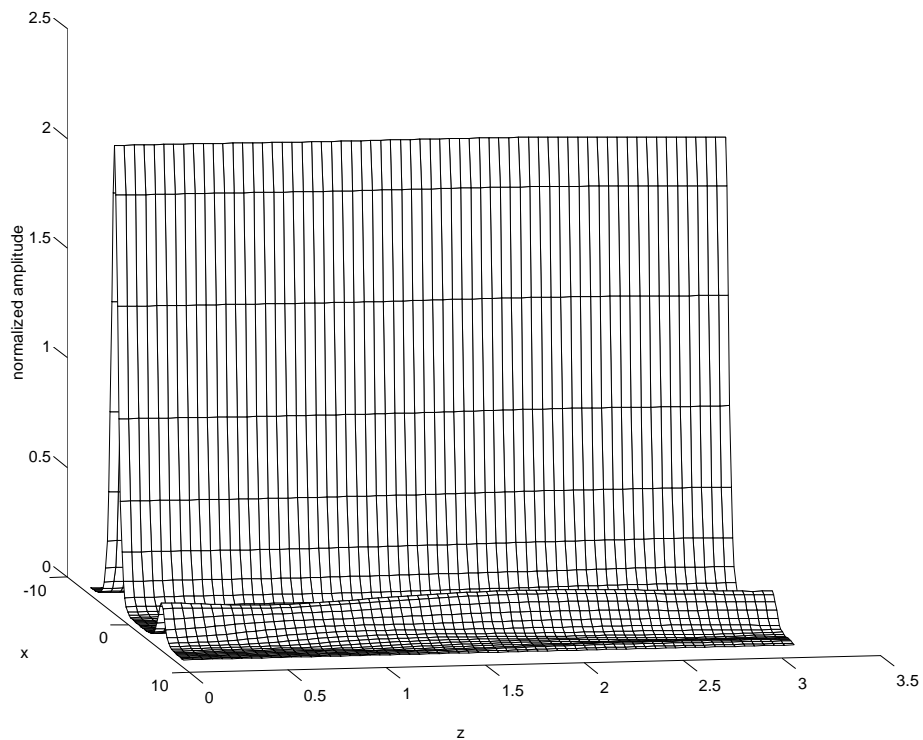


Figure 2.7: An example of the evolution of a slightly perturbed asymmetric soliton at  $Q = 0.1$ .

Shown are the fundamental harmonics in both waveguides.

In all the cases in which the asymmetric stationary solitons were found by the

shooting method, the PDE simulations have demonstrated their stability. A typical example is displayed, for  $Q = 0.1$  in Fig. 2.7. In this figure, two well separated solitons are seen. The first one is the larger  $u_1$  component of the stationary soliton, while the second soliton is represented by the smaller  $u_2$  component of essentially the same solution. (Recall that at  $Q = 0.1$ , the solution is strongly asymmetric.) The peak values of the components of the perturbed soliton undergo minor fluctuations (within 1%). The fluctuations show no sign of decay, but they are not growing either. This has been checked by making some runs for much longer propagation distance. Thus, it may be concluded that all the stationary asymmetric solitons are, in effect, neutrally (or marginally) stable.

We also ran simulations with large initial perturbations of the asymmetric solitons. From these runs, we can formulate an inference that strongly perturbed solitons demonstrate persistent internal vibrations, without being destroyed by the perturbations, but also without emitting conspicuous amounts of radiations.

We also checked numerically the stability of the exact symmetric solutions for  $Q$  beyond the bifurcation point at  $Q_{cr} = 5/13$ . First of all, one should expect that, for  $Q < Q_{cr}$ , the symmetric soliton must be destabilized by the bifurcation producing the stable asymmetric solitons. As is illustrated by Fig. 2.8, this is indeed the case. Moreover, the instability evolution illustrated by Fig. 2.8 demonstrates a trend to rearrange the unstable symmetric soliton into a stable asymmetric one existing at the same value of  $Q$ . This process is, though, quite slow, because it gives rise to strong internal vibrations of the solitary wave, for which, in accord with a rather general property of the SHG systems mentioned above at the beginning of this section, the damping is very weak.

At  $Q > Q_{cr}$ , the symmetric solitons are stable. An example, shown in Fig. 2.9 for

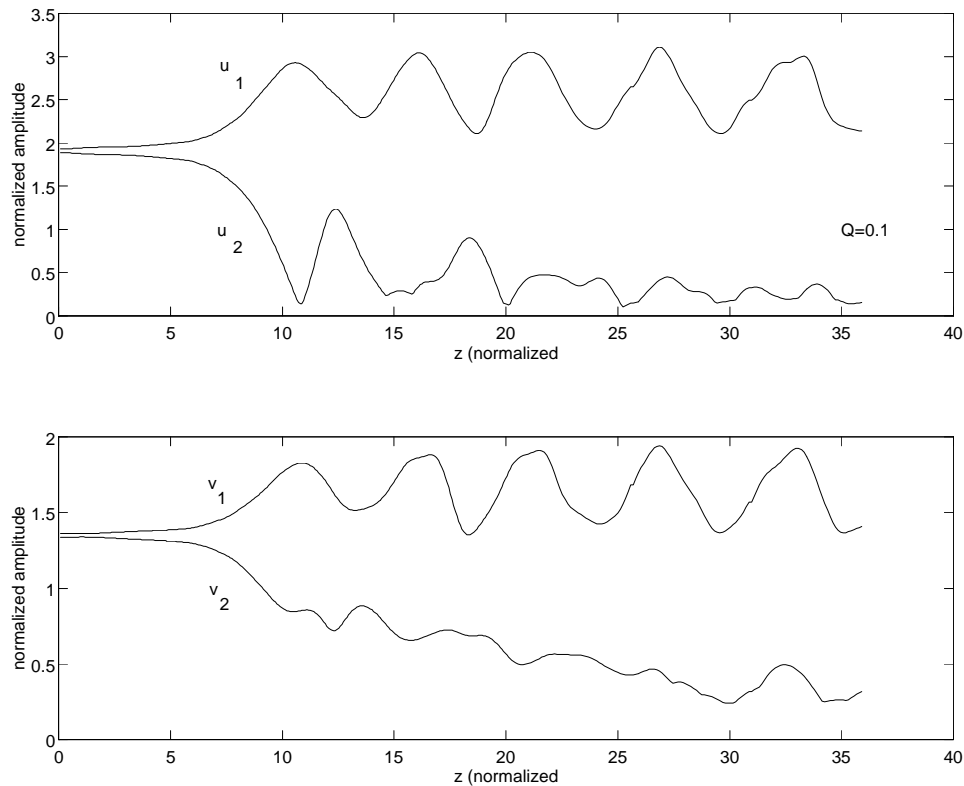


Figure 2.8: Evolution of the peak values of the components  $u_{1,2}$  and  $v_{1,2}$  illustrating the instability of the symmetric soliton at  $Q = 0.1$ .

$Q = 0.4$ , shows that the initially introduced perturbations trigger internal vibrations of the solitary wave around the stationary symmetric solution. Very little damping can be seen, but the vibrations are not growing either. Thus, we can conclude that the symmetric solitons here are also, effectively, neutrally stable, as the asymmetric solitons that exist beyond the bifurcation point,  $Q < Q_{cr}$ .

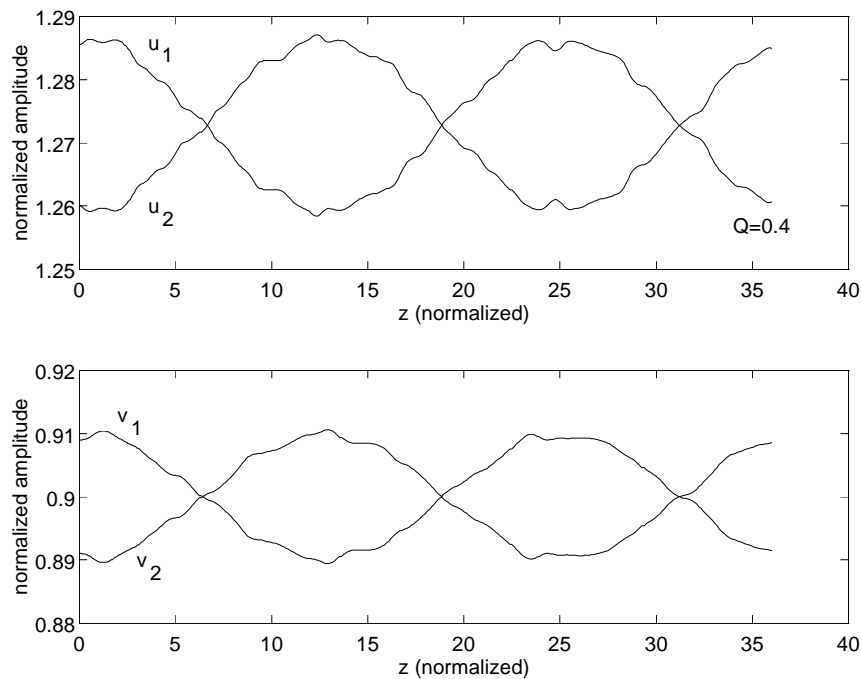


Figure 2.9: Evolution of the peak values of the components  $u_{1,2}$  and  $v_{1,2}$  for  $Q = 0.4$ . In this case, the symmetric soliton is (neutrally) stable.

## 2.5 Summary

In this chapter, we have formulated and analyzed a model which describes two linearly coupled quadratically nonlinear waveguides. The model includes two equations for the fundamental harmonics, and two equations for the second harmonics. We considered in detail the important special case of closely coupled waveguides, no walkoff and fully matched harmonics, when the only control parameter is the coupling constant, the same for both harmonics. It was demonstrated that, alongside the obvious symmetric solitons, the model supports asymmetric solitary waves. A bifurcation point at which the asymmetric solutions appear was found using both the variational analysis, and the exact mathematical analysis. The variational

approximation also gives a full description of the solutions in an analytical form. Comparison with numerical results obtained using the shooting method has demonstrated that this approximation provides a fairly good accuracy in a part of the range where existence of the stationary asymmetric solitons was predicted, while in another part of this range, where  $Q < 0.3$ , asymmetric solitary wave solutions were not found, although periodic solutions can be easily obtained. The reason is the instability of the numerical method in this range of  $Q$  values. Then, direct simulations of the full PDEs have shown that the asymmetric solitons, whenever they exist, are always neutrally stable. On the contrary, the symmetric solitons are also neutrally stable only to the right of the bifurcation point at  $5/13$ , where the asymmetric solitons do not exist. To the left of this bifurcation point, the symmetric soliton is found to be unstable, demonstrating a trend to rearrange itself into the stable asymmetric soliton that exists at the same value of the coupling constant  $Q$ .

Note, from Eqs. (2.1), that the coupling constants  $Q$  and  $K$  are the fractional change in the wave envelopes per unit diffraction length, which, for quadratic nonlinear waveguides, are typically in the centimeter range. From Eqs. (2.10)&(2.20), the limits of the existence range of solitary wave solutions,  $-1 < Q < 1$ , correspond to complete coupling from one waveguide to another.

In the next chapter, we will investigate the system when the assumption of closely coupled waveguides is removed. It leads to a much richer bifurcation phenomenon.

# Chapter 3

## Coupled Quadratically Nonlinear Waveguides

### (The General Case)

#### 3.1 Introduction

In the last chapter, solitons in a model of parallel-coupled waveguides with quadratic nonlinearity were studied. However, only a very limited situation was considered there. The most essential limitation is the assumption that the coupling constants between the fundamental harmonics (FH) and between the second harmonics (SH) are equal. This assumption implies that the separation between the two waveguides is small, so that the FHs and the SHs are equally coupled. Evidently, this is very restrictive. In this chapter, the aim is to extend the study of the solitons in parallel-coupled quadratically nonlinear waveguides, by removing this restriction, which corresponds, physically, to varying the separation between the two cores. We denote

the FH and SH coupling constants as  $Q$  and  $K$ . So, in this chapter, we consider the case  $Q \neq K$ . Consideration of the general case of unequal couplings is of principal interest, because it has no analog in terms of the single waveguides. The main issues to be considered are the asymmetric solitons and bifurcations which give rise to them, and the stability of the asymmetric and symmetric solitons. In this chapter, it will be shown that the bifurcation discussed in the last chapter is extended for this more general case, and the result needs to be formulated in the form of three dimensional bifurcation diagrams.

## 3.2 Mathematical Model

The general model to describe the copropagation of FH  $u$  and SH  $v$  in the linearly coupled waveguides was put forward in the last chapter. It is repeated here, for convenience of reference,

$$\begin{aligned}
 i\frac{\partial u_1}{\partial z} + i\delta\frac{\partial u_1}{\partial x} + \frac{1}{2}\frac{\partial^2 u_1}{\partial x^2} & \quad qu_1 + u_1^*v_1 = & \quad Qu_2, \\
 2i\frac{\partial v_1}{\partial z} + 2i\delta\frac{\partial v_1}{\partial x} + \frac{1}{2}\frac{\partial^2 v_1}{\partial x^2} & \quad v_1 + \frac{1}{2}u_1^2 = & \quad Kv_2, \\
 i\frac{\partial u_2}{\partial z} + i\delta\frac{\partial u_2}{\partial x} + \frac{1}{2}\frac{\partial^2 u_2}{\partial x^2} & \quad qu_2 + u_2^*v_2 = & \quad Qu_1, \\
 2i\frac{\partial v_2}{\partial z} + 2i\delta\frac{\partial v_2}{\partial x} + \frac{1}{2}\frac{\partial^2 v_2}{\partial x^2} & \quad v_2 + \frac{1}{2}u_2^2 = & \quad Kv_1,
 \end{aligned} \tag{3.1}$$

where the symbols carry the same meaning as in the last chapter. In the discussion of this chapter, we still keep the assumptions that  $\delta = 0$ , and  $q = 1$ , which means that we are still considering the no walkoff and fully phase matching cases. Removal of these assumptions to consider the effects of walkoff and phase mismatch will be deferred to the next chapter.

In this chapter, our analysis imposes no technical restrictions on the values of the

coupling constants  $K$  and  $Q$  in Eqs. (3.1). However, there is a physical limitation  $|K| \leq |Q|$ : it is very unlikely that the SH coupling can be stronger than the FH coupling. With regard to this restriction, the range  $K > 5/13$  was not considered, because only evident symmetric solutions exist there. In the negative  $K$  domain, we will limit our investigation to  $K > -1$ , which is another boundary for the existence of asymmetric solitons.

### 3.3 Stationary Solution

To obtain stationary solutions, one should drop the  $z$ -derivative terms in Eqs. (3.1), and set all the variables real. (We also put  $\delta = 0$ , and  $q = 1$ .) Thus, we obtain

$$\begin{aligned}
 \frac{1}{2} \frac{\partial^2 u_1}{\partial x^2} + u_1 + u_1 v_1 + Q u_2 &= 0, \\
 \frac{1}{2} \frac{\partial^2 u_2}{\partial x^2} + u_2 + u_2 v_2 + Q u_1 &= 0, \\
 \frac{1}{2} \frac{\partial^2 v_1}{\partial x^2} + v_1 + \frac{1}{2} u_1^2 + K v_2 &= 0, \\
 \frac{1}{2} \frac{\partial^2 v_2}{\partial x^2} + v_2 + \frac{1}{2} u_2^2 + K v_1 &= 0.
 \end{aligned} \tag{3.2}$$

As in the previous chapter, the analysis consists of two independent parts. First, analytic approximate results were sought for, using the variational analysis (VA) approach; however, different from the VA in last chapter, instead of using a  $\text{sech}^2$  function as ansatz, the more general Gaussian ansatz is used in this chapter. The second part of the analysis, which serves as a check of the approximate results obtained by VA, is a numerical analysis using a modified version of the method of lines (see, e.g., [53]. It is also called the relaxation method elsewhere [52].), instead of using the Shooting method used in the last chapter. The reasons for making these changes will be elaborated below in the following subsections.

### 3.3.1 Variational Analysis

The difference of the variational analysis in this chapter from that in the last chapter is that we use the Gaussian ansatz. When  $K = Q$ , the relations between the FH and SH waves are

$$v_{1,2} = \pm \frac{1}{\sqrt{2}} u_{1,2}. \quad (3.3)$$

However, since we allow the waveguides to have different coupling constants for FH and SH, Eq. (3.3) is no longer true. FH and SH waves will thus have different widths. Moreover, as discussed in the last chapter, and shown in Fig. 2.3, the widths of the solitons estimated by VA using a  $\text{sech}^2$  ansatz do not agree very well with those obtained numerically by the shooting method. This is because of the inherent weakness of using the  $\text{sech}^2$  ansatz that only a single width parameter can be used. Thus, it is necessary to use another ansatz for the more general case considered here in order to allow for different widths of all the four components of the soliton. It has to be mentioned here that the Gaussian ansatz was earlier successfully applied to description of solitons in a single-core quadratically nonlinear waveguide [39].

The basic idea of the variational analysis is to make use of the Hamilton's principle that the solution exists at the point where the action given by the time integral of the Lagrangian is at its extremum. As what has been discussed in detail in Sec. 2.3.1 in the last chapter, this corresponds to demanding the variations of the effective Lagrangian with respect to each of the parameters to be zero.

As mentioned above, in this analysis, we use the more general Gaussian ansatz, and it is

$$\begin{aligned} u_1 &= A_1 \exp\left(\frac{1}{2}\alpha_1 x^2\right), \\ u_2 &= A_2 \exp\left(\frac{1}{2}\alpha_2 x^2\right), \end{aligned}$$

$$\begin{aligned} v_1 &= B_1 \exp\left(\frac{1}{2}\beta_1 x^2\right), \\ v_2 &= B_2 \exp\left(\frac{1}{2}\beta_2 x^2\right), \end{aligned} \quad (3.4)$$

where  $A_1$ ,  $A_2$ ,  $B_1$ , and  $B_2$  are the amplitudes, and  $\alpha_1$ ,  $\alpha_2$ ,  $\beta_1$ , and  $\beta_2$  are the width parameters of the FH and SH of the soliton solution sought for. The subscripts 1 and 2 pertain to the two cores.

Following the theory as described in Sec. 2.3.1, the Lagrangian density of Eqs. (3.2) is

$$\begin{aligned} \mathcal{L} &= \frac{1}{4} \left[ (u_1')^2 + (u_2')^2 + (v_1')^2 + (v_2')^2 \right] - \frac{1}{2} (u_1^2 + u_2^2) - \frac{1}{2} (v_1^2 + v_2^2) \\ &\quad + Qu_1u_2 + Kv_1v_2 + \frac{1}{2}u_1^2v_1 + \frac{1}{2}u_2^2v_2, \end{aligned} \quad (3.5)$$

where the prime stands for  $d/dx$ .

Inserting Eqs. (3.4) into Eq. (3.5), we calculate the effective Lagrangian  $L$ ,

$$\begin{aligned} \frac{2}{\sqrt{\pi}}L &\equiv \frac{2}{\sqrt{\pi}} \int_{-\infty}^{+\infty} \mathcal{L} dx = \\ &\quad \frac{1}{4}A_1^2\sqrt{\alpha_1} - \frac{1}{4}A_2^2\sqrt{\alpha_2} - \frac{1}{4}B_1^2\sqrt{\beta_1} - \frac{1}{4}B_2^2\sqrt{\beta_2} - A_1^2\alpha_1^{\frac{1}{2}} - A_2^2\alpha_2^{\frac{1}{2}} \\ &\quad - B_1^2\beta_1^{\frac{1}{2}} - B_2^2\beta_2^{\frac{1}{2}} + 2A_1A_2Q\sqrt{\frac{2}{\alpha_1 + \alpha_2}} + 2B_1B_2K\sqrt{\frac{2}{\beta_1 + \beta_2}} \\ &\quad + A_1^2B_1\sqrt{\frac{2}{2\alpha_1 + \beta_1}} + A_2^2B_2\sqrt{\frac{2}{2\alpha_2 + \beta_2}}. \end{aligned} \quad (3.6)$$

The variational equations are obtained by demanding the variations of the effective Lagrangian  $L$  with respect to each of  $A_{1,2}$ ,  $B_{1,2}$ ,  $\alpha_{1,2}$ , and  $\beta_{1,2}$  to be zero. Then, we obtain the following eight equations:

$$\frac{2}{\sqrt{\pi}} \left( \frac{\partial L}{\partial A_1} \right) = \frac{1}{2}A_1\alpha_1^{\frac{1}{2}} - 2A_1\alpha_1^{\frac{1}{2}} + 2A_2Q\sqrt{\frac{2}{\alpha_1 + \alpha_2}} + 2A_1B_1\sqrt{\frac{2}{2\alpha_1 + \beta_1}} = 0, \quad (3.7)$$

$$\frac{2}{\sqrt{\pi}} \left( \frac{\partial L}{\partial A_2} \right) = \frac{1}{2}A_2\alpha_2^{\frac{1}{2}} - 2A_2\alpha_2^{\frac{1}{2}} + 2A_1Q\sqrt{\frac{2}{\alpha_1 + \alpha_2}} + 2A_2B_2\sqrt{\frac{2}{2\alpha_2 + \beta_2}} = 0, \quad (3.8)$$

$$\frac{2}{\sqrt{\pi}} \left( \frac{\partial L}{\partial B_1} \right) = \frac{1}{2} B_1 \beta_1^{\frac{1}{2}} \quad 2B_1 \beta_1^{\frac{1}{2}} + 2B_2 K \sqrt{\frac{2}{\beta_1 + \beta_2}} + A_1^2 \sqrt{\frac{2}{2\alpha_1 + \beta_1}} = 0, \quad (3.9)$$

$$\frac{2}{\sqrt{\pi}} \left( \frac{\partial L}{\partial B_2} \right) = \frac{1}{2} B_2 \beta_2^{\frac{1}{2}} \quad 2B_2 \beta_2^{\frac{1}{2}} + 2B_1 K \sqrt{\frac{2}{\beta_1 + \beta_2}} + A_2^2 \sqrt{\frac{2}{2\alpha_2 + \beta_2}} = 0, \quad (3.10)$$

$$\begin{aligned} \frac{2}{\sqrt{\pi}} \left( \frac{\partial L}{\partial \alpha_1} \right) &= \frac{1}{8} A_1^2 \alpha_1^{\frac{1}{2}} + \frac{1}{2} A_1^2 \alpha_1^{\frac{3}{2}} \quad \sqrt{2} A_1 A_2 Q (\alpha_1 + \alpha_2)^{\frac{3}{2}} \\ &\quad \sqrt{2} A_1^2 B_1 (2\alpha_1 + \beta_1)^{\frac{3}{2}} = 0, \end{aligned} \quad (3.11)$$

$$\begin{aligned} \frac{2}{\sqrt{\pi}} \left( \frac{\partial L}{\partial \alpha_2} \right) &= \frac{1}{8} A_2^2 \alpha_2^{\frac{1}{2}} + \frac{1}{2} A_2^2 \alpha_2^{\frac{3}{2}} \quad \sqrt{2} A_1 A_2 Q (\alpha_1 + \alpha_2)^{\frac{3}{2}} \\ &\quad \sqrt{2} A_2^2 B_2 (2\alpha_2 + \beta_2)^{\frac{3}{2}} = 0, \end{aligned} \quad (3.12)$$

$$\begin{aligned} \frac{2}{\sqrt{\pi}} \left( \frac{\partial L}{\partial \beta_1} \right) &= \frac{1}{8} B_1^2 \beta_1^{\frac{1}{2}} + \frac{1}{2} B_1^2 \beta_1^{\frac{3}{2}} \quad \sqrt{2} B_1 B_2 K (\beta_1 + \beta_2)^{\frac{3}{2}} \\ &\quad \frac{\sqrt{2}}{2} A_1^2 B_1 (2\alpha_1 + \beta_1)^{\frac{3}{2}} = 0, \end{aligned} \quad (3.13)$$

$$\begin{aligned} \frac{2}{\sqrt{\pi}} \left( \frac{\partial L}{\partial \beta_2} \right) &= \frac{1}{8} B_2^2 \beta_2^{\frac{1}{2}} + \frac{1}{2} B_2^2 \beta_2^{\frac{3}{2}} \quad \sqrt{2} B_1 B_2 K (\beta_1 + \beta_2)^{\frac{3}{2}} \\ &\quad \frac{\sqrt{2}}{2} A_2^2 B_2 (2\alpha_2 + \beta_2)^{\frac{3}{2}} = 0. \end{aligned} \quad (3.14)$$

Because these algebraic equations cannot be solved analytically, we resort to the numerical Newton-Raphson method to find the solutions for the 8 parameters  $A_1$ ,  $A_2$ ,  $B_1$ ,  $B_2$ ,  $\alpha_1$ ,  $\alpha_2$ ,  $\beta_1$ , and  $\beta_2$ . The Newton-Raphson method will be described briefly in the next subsection.

### 3.3.2 Newton-Raphson method

The Newton-Raphson method is a well-known method for solving nonlinear algebraic equations. Good reference to this method can be found in, e.g., [53, 60]. For the self-consistency of this thesis, we will describe it briefly here.

Let  $f(s)$  be a real-valued scalar function and the method is used to solve the equation

$$f(s) = 0. \quad (3.15)$$

If we expand  $f(s)$  in Taylor series about  $s = s_m$ , we will have

$$f(s) = f(s_m) + f'(s_m)(s - s_m) + \frac{1}{2}f''(s_m)(s - s_m)^2 + \cdots = 0, \quad (3.16)$$

where the prime here denotes  $d/ds$ . Newton-Raphson method arises from linearizing  $f(s)$ , i.e., replacing  $f(s)$  by a linear approximation consisting of the first two terms in its Taylor expansion. From Eq. (3.16), it can be seen that

$$s_{m+1} = s_m - \frac{f(s_m)}{f'(s_m)}, \quad (3.17)$$

where  $s_m$  and  $s_{m+1}$  here denote the values of  $s$  at the  $m$ -th and the  $(m + 1)$ -th iterations. It can be shown that this process of iteration gives second-order convergence to the true root of  $s$ . However, there is a catch in using the Newton-Raphson method: the method is a local method; convergence is second-order only if the initial guess of  $s$  is *close enough* to the true root.

The same idea can be extended to solve a system of equations such as Eqs. (3.7-3.14). If we write

$$\tilde{f}(\tilde{s}) = 0 \quad (3.18)$$

where  $\tilde{f}$  is a vector function,  $\tilde{f}(\tilde{s}) = [f_1(\tilde{s}), \dots, f_8(\tilde{s})]^T$ ; the  $f_1, \dots, f_8$  stands for the functions in Eqs. (3.7-3.14), and  $\tilde{s} = (A_1, A_2, B_1, B_2, \alpha_1, \alpha_2, \beta_1, \beta_2)^T$ . Expanding  $\tilde{f}(\tilde{s})$  around an approximation  $\tilde{s}_m$  using a linear approximation of  $\tilde{f}(\tilde{s})$  will give

$$\tilde{f}(\tilde{s}_m) + \tilde{J}(\tilde{s}_m)(\tilde{s}_{m+1} - \tilde{s}_m) = 0, \quad (3.19)$$

where  $\tilde{J}(\tilde{s})$  is the Jacobian matrix

$$\tilde{J} = \begin{bmatrix} \frac{\partial f_1}{\partial A_1} & \cdots & \frac{\partial f_1}{\partial \beta_2} \\ \vdots & \ddots & \vdots \\ \frac{\partial f_8}{\partial A_1} & \cdots & \frac{\partial f_8}{\partial \beta_2} \end{bmatrix} \quad (3.20)$$

If the initial guess  $\tilde{s}_o$  is sufficiently close to the true solution, the method converges very rapidly (also with quadratic convergence as the scalar case).

### 3.3.3 Numerical Analysis

As mentioned in the last chapter, the Shooting method introduces numerical instability in the range of the coupling constant  $Q < 0.3$ . It failed to produce the stationary soliton solutions in that parameter range; thus, another numerical method is adopted in the work described in this chapter. The method is a modified version of the method of lines (which is also called the relaxation method in [52]).

First, we discretize the transverse space variable  $x$ . We replace the integration domain  $dm$  of  $x$  by a set of  $n$  points:

$$x_k = (k-1)h, \quad k = 1, 2, \dots, n, \quad h \equiv \frac{dm}{n-1}. \quad (3.21)$$

Along each of the lines  $(x_k, z)$  for  $z \geq 0$ , we denote the values of  $u_1$  by  $u_{1k}$  (and similarly for  $u_2$  and  $v_1, v_2$ ). Then, the finite-difference approximation is used for  $\partial^2 u / \partial x^2$ :

$$\frac{\partial^2 u}{\partial x^2} = \frac{u_{k-1} - 2u_k + u_{k+1}}{h^2},$$

the error of the numerical scheme being  $O(h^2)$ .

With this approximation, we transform the system of ODEs, Eqs. (3.2) to a system of finite-difference nonlinear algebraic equations,

$$\mathcal{F} = 0, \quad (3.22)$$

where  $\mathcal{F}$  is a system of  $4n \times 1$  vector functions defined by

$$\mathcal{F}_k = \begin{cases} \frac{1}{2} \left( \frac{w_{k-1} - 2w_k + w_{k+1}}{h^2} \right) & w_k + w_k^* w_{2n+k} + Q w_{n+k} & \text{for } 1 \leq k \leq n, \\ \frac{1}{2} \left( \frac{w_{k-1} - 2w_k + w_{k+1}}{h^2} \right) & w_k + w_k^* w_{2n+k} + Q w_{k-n} & \text{for } (n+1) \leq k \leq 2n, \\ \frac{1}{2} \left( \frac{w_{k-1} - 2w_k + w_{k+1}}{h^2} \right) & w_k + \frac{1}{2} w_k^2_{2n} + K w_{k+n} & \text{for } (2n+1) \leq k \leq 3n, \\ \frac{1}{2} \left( \frac{w_{k-1} - 2w_k + w_{k+1}}{h^2} \right) & w_k + \frac{1}{2} w_k^2_{2n} + K w_{k-n} & \text{for } (3n+1) \leq k \leq 4n. \end{cases} \quad (3.23)$$

In Eq. (3.23), we have denoted

$$w_k \equiv \begin{cases} u_{1k} & \text{for } 1 \leq k \leq n, \\ u_{2(k-n)} & \text{for } (n+1) \leq k \leq 2n, \\ v_{1(k-2n)} & \text{for } (2n+1) \leq k \leq 3n, \\ v_{2(k-3n)} & \text{for } (3n+1) \leq k \leq 4n, \end{cases}$$

Of course, the  $w_{k-1}$  and  $w_{k+1}$  terms have to be equated to zero in Eq. (3.22) at the boundaries of the integration domain to get the correct boundary conditions for the solitary wave solutions.

Now, as a system of nonlinear algebraic equations, Eq. (3.22) can again be solved by the Newton-Raphson method. The corresponding Jacobian matrix is obtained by calculating  $\partial \mathcal{F}_j / \partial w_k$ , where  $1 \leq j \leq 4n$ , and  $1 \leq k \leq 4n$ . It is a  $4n \times 4n$  matrix. Further technical details on how to obtain the solutions from here onward will not be elaborated.

### 3.3.4 Discussion of Results

First, we will display results for the stationary solitons obtained by means of VA. We should stress, however, that, except for a peculiar narrow parametric region described below, the variational results are always fairly close to the direct numerical ones. A detailed comparison will be given at the end of this subsection.

We have found that the asymmetric soliton solutions exist only in the regions  $R$  and  $S$  in the  $(K, Q)$  plane as shown in Fig. 3.1. The solid lines mark the loci of the bifurcation points, whereas the dotted lines are  $Q = \pm K$ , which mark off the physically unrealistic regions where the SH coupling is larger than the FH coupling (i.e.,  $|K| > |Q|$ ). Thus, in the two triangular regions delineated by the dotted lines and the vertical axes, the asymmetric solitons do exist, but are physically unrealistic. It is to be repeated here that the range of existence of the asymmetric solitons is found to be

$$1 < K < 0.385. \quad (3.24)$$

The upper limit was found exactly as  $5/13$  in the last chapter, which is approximated by 0.385.

The variational results allow us to construct two *three-dimensional* bifurcation diagrams shown in Figs. 3.2 and 3.3, for FH and SH respectively. They are plots, vs. the coupling constants  $K$  and  $Q$ , of the effective asymmetry parameters  $\Theta_{\text{F}}$  and  $\Theta_{\text{S}}$  defined as follows:

$$\Theta_{\text{F}} = \frac{u_1^2}{u_1^2 + u_2^2} \frac{u_2^2}{u_1^2 + u_2^2}, \quad (3.25)$$

$$\Theta_{\text{S}} = \frac{v_1^2}{v_1^2 + v_2^2} \frac{v_2^2}{v_1^2 + v_2^2}, \quad (3.26)$$

where  $u_{1,2}$  and  $v_{1,2}$  without the argument  $x$  are the peak values of the corresponding waves. Note that the middle portions of the curved surfaces, corresponding to the unphysical situation with  $|K| > |Q|$ , have been chopped off. We stress that, although it is shown in Figs. 3.2 and 3.3 that both  $\Theta_{\text{F}}$  and  $\Theta_{\text{S}}$  are zero in these regions, asymmetric solitons do exist in these regions as mathematical objects.

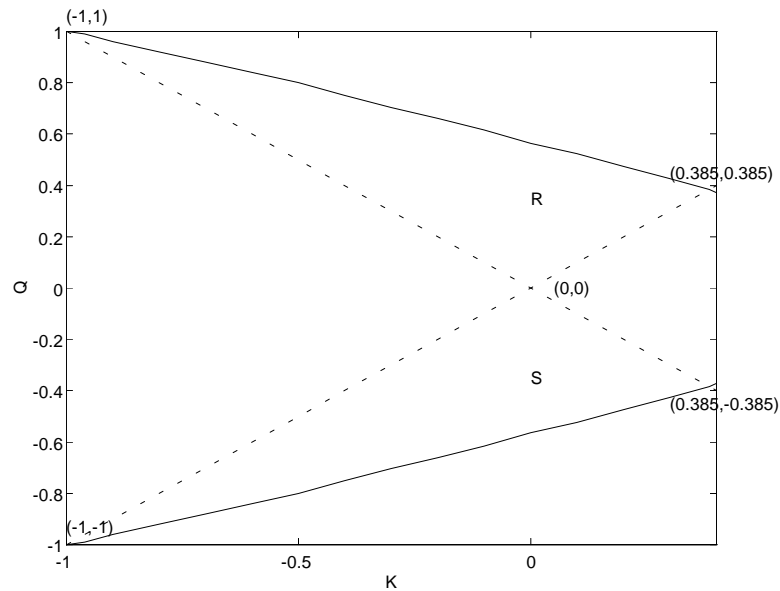


Figure 3.1: The bifurcation regions. Asymmetric solitons exist in the regions marked by R and S. The corners of the regions are at  $(-1, \pm 1)$ ,  $(0, 0)$  and  $(0.385, \pm 0.385)$ . The dotted lines are the lines  $Q = \pm K$ , to separate the unphysical area where  $|K| > |Q|$ . The solid lines are the loci of the bifurcation points found numerically.

In general, at all values of  $K$ , the FH fields of the asymmetric solitons are more asymmetric at small  $|Q|$ . In fact, at  $|Q| = |K| = 0$ , the two waveguides become decoupled, and the field in the second waveguide is absent (we adopt a convention to allocate the number 1 to the waveguide carrying larger fields, i.e.,  $u_1 \geq u_2$  and  $v_1 \geq v_2$ ). As  $|Q|$  increases from zero, the asymmetry of the FH fields monotonically decreases; on the other hand, the asymmetry of the SH fields at first gets even stronger, and then rapidly decreases as the bifurcation point is approached. The asymmetric solutions finally merge with the symmetric ones at

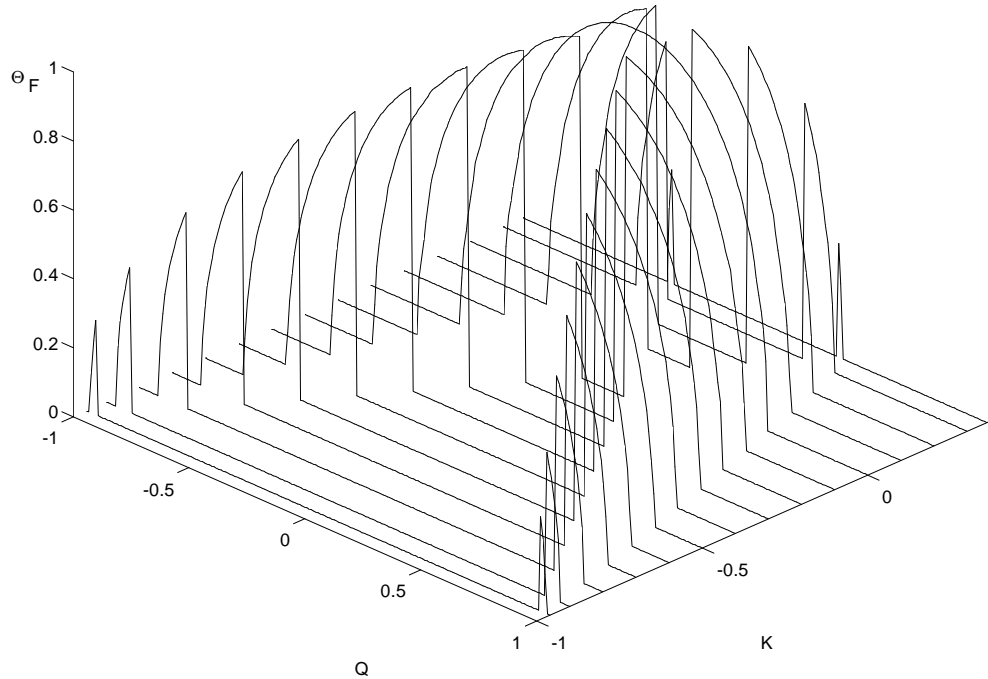


Figure 3.2: The bifurcation diagram for the fundamental harmonics. The middle portions are chopped off since  $|K| > |Q|$  there.

the bifurcation points. These trends are more evident for more negative  $K$ . Close to  $K = -1$ , the SH fields attain the strongest asymmetry at very sharp parts of the bifurcation diagram (Fig. 3.3). As  $K$  becomes more and more negative, the bifurcation points spread apart towards larger values of  $|Q|$ .

The characteristics of the asymmetric solutions can be further clarified by looking at Figs. 3.4 and 3.5, which are plots of the peak values of  $u_{1,2}$  and  $v_{1,2}$  versus  $Q$ , with  $K$  fixed as a parameter. (In both Figs. 3.4 and 3.5, the solid lines are for the waves in waveguide 1 and the dotted lines are for the waves in waveguide 2.) For

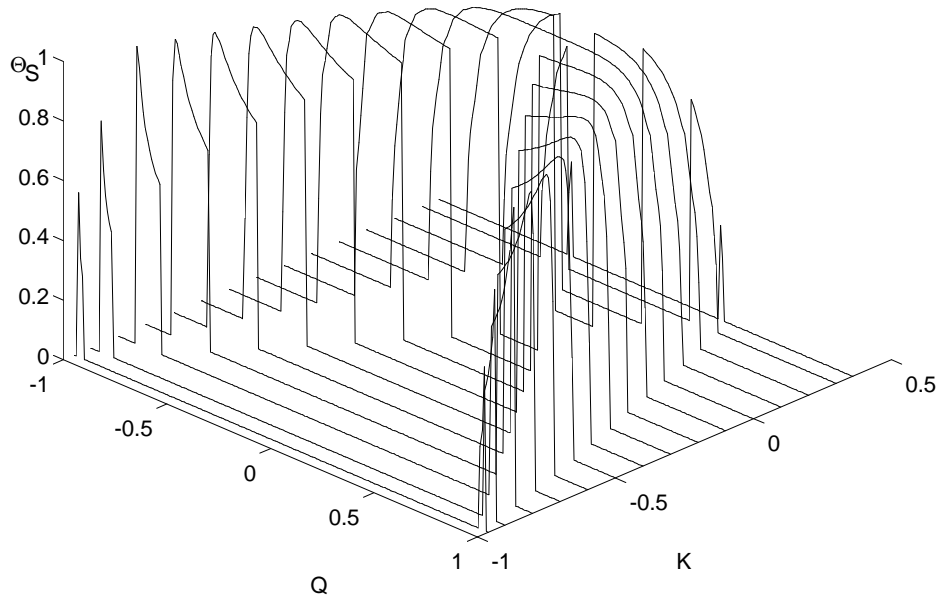


Figure 3.3: The bifurcation diagram for the second harmonics. The middle portions are chopped off since  $|K| > |Q|$  there.

both FH and SH fields in the waveguide 1, as  $K$  decreases (but remains positive), the fields become larger, and they reach a maximum at  $K = 0$ . Then, as  $K$  keeps on decreasing further to negative values, the fields become smaller. The FH field decreases towards zero as  $K \rightarrow -1$ . In the waveguide 2, both FH and SH decrease as  $K$  decreases. We adopt a convention that the amplitudes of the fields in the waveguide 2 are negative when they have the sign opposite to that in the waveguide 1. So, the amplitude of the SH field in the waveguide 2 assumes a larger absolute value when  $K$  is getting more negative.

In fact, at  $Q = 0$ , when  $K \rightarrow -1$ , the absolute peak values of both  $v_1$  and  $v_2$  approach the same value, but they are of opposite sign, whereas  $u_1$  approaches zero

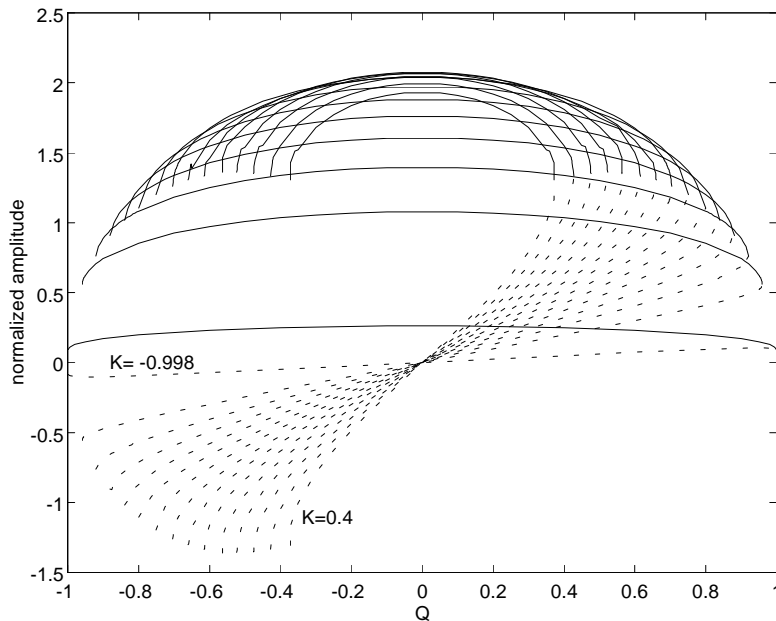


Figure 3.4: The peak values of  $u_{1,2}$  vs  $Q$ , with  $K$  as a parameter. The solid lines stand for  $u_1$ , and the dotted lines are for  $u_2$ .  $K$  takes the values:  $K = 0.4, 0.3, \dots, 0.8, 0.9, 0.998$ .

and  $u_2$  is identically zero, so, that the soliton becomes anti-symmetric, with the dominant SH field. However, since this is an unphysical case, we will not discuss it further.

An noteworthy point is that when  $K$  is negative, the field  $v_2$  changes its sign from positive to negative as  $|Q|$  decreases past a certain value (depending on the value of  $K$ ). When this sign reversal takes place, the field  $v_2$  is essentially non-Gaussian over a narrow range of  $Q$ , and has a very small value (see Fig. 3.6). Coincidentally, these non-Gaussian solutions correspond to the sharp portions of the strongest asymmetry in the bifurcation diagram for SH (Fig. 3.3). Thus, VA based on the Gaussian ansatz is inappropriate in this narrow parametric region, but it proves to be appropriate in all the other cases.

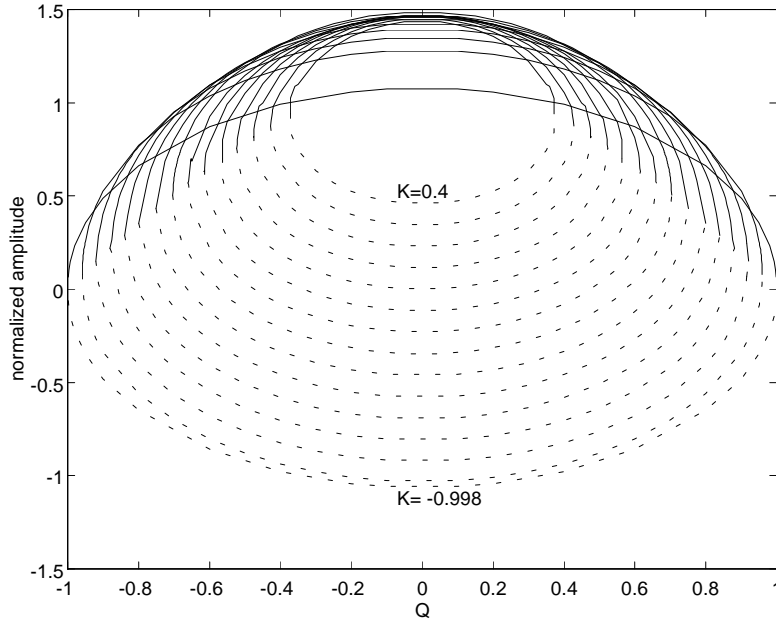


Figure 3.5: The peak values of  $v_{1,2}$  vs  $Q$ , with  $K$  as a parameter. The solid lines stand for  $v_1$ , and the dotted lines are for  $v_2$ .  $K$  takes the values:  $K = 0.4, 0.3, \dots, 0.8, 0.9, 0.998$ .

The widths of the components of the soliton solutions also vary with  $K$  and  $Q$ . Fig. 3.7 shows the plot of the spot size  $W_1$  vs.  $K$  and  $Q$  for the component  $u_1$ , which is defined as follows:

$$W_1 = 1/\sqrt{\alpha_1}, \quad (3.27)$$

$\alpha_1$  being the width parameter according to Eq. (3.4). In general, the spot size increases towards infinity as  $K \rightarrow -1, |Q| \rightarrow 1$ . As the peak values of the fields are simultaneously approaching zero there, this implies that the solutions are spreading out indefinitely in this limit.

Before proceeding to comparison of the analytical results obtained by means of VA and numerical findings, it is relevant to mention that, in order to validate our numerical results, we compared them as produced by different methods. As a

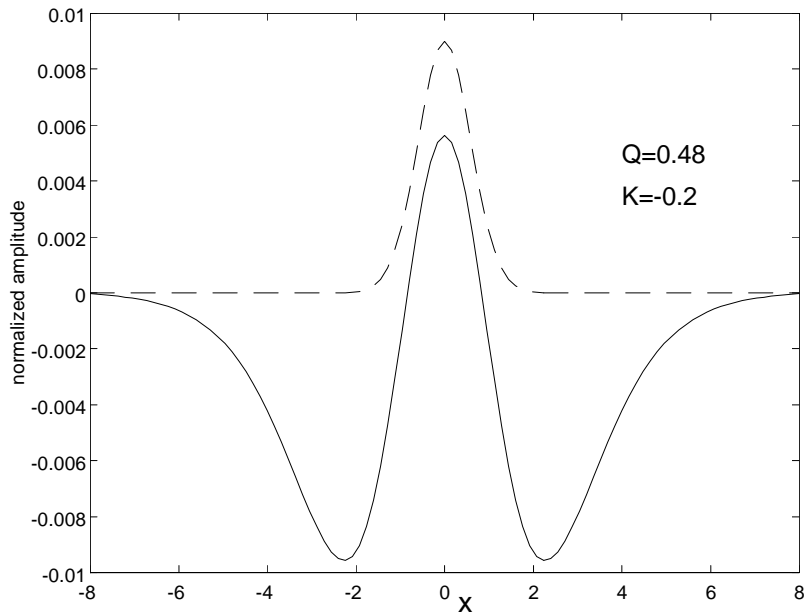


Figure 3.6: The shape of the SH component  $v_2$  of the asymmetric soliton at  $Q = 0.48$  and  $K = -0.2$ , where the sign reversal of  $v_2$  occurs. The solid line is the actual non-Gaussian shape of the soliton obtained by the numerical method. The dashed line is the prediction of the variational approximation. Since the variational approximation uses the Gaussian ansatz, it fails to predict the correct shape in a narrow parametric region around this point.

typical example, we can mention what was obtained for the peak values  $u_1$  of the FH in the waveguide 1. In the limit case  $K = Q$ , we compared the results obtained from the modified method of lines with those produced by the shooting method described in the last chapter. The modified method of lines used 101 lines; i.e., the discrete grid in the  $x$  domain has 101 points. The results were compared for the range of  $Q$  from 0.2 to 0.3, the worst discrepancy being 1.7% at  $Q = 0.2$ ; otherwise, the discrepancies are all under 1%.

To check the relevance of the results obtained by means of VA, we compared them with those produced by two versions of the modified numerical method of lines,

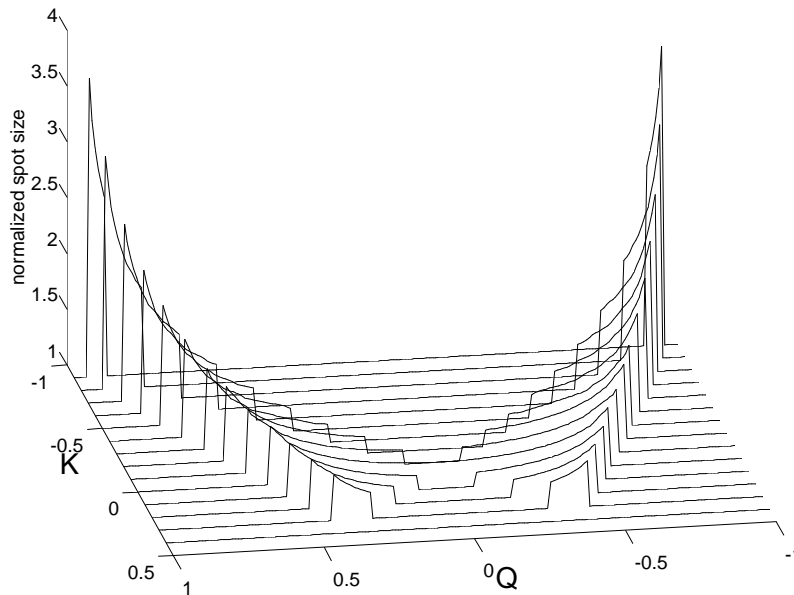


Figure 3.7: The spot size of  $u_1$  of asymmetric solitons versus  $K$  and  $Q$ . The middle portion has been chopped off because  $|K| > |Q|$  there. Also, note that the other flat portion of the plot outside the curved surface has no meaning, since data were not gathered for symmetric solitons there.

using, respectively, 101 and 161 lines (the latter number was a technical limit set by the computer used), for  $K$  and  $Q$  taking on different values. In this relation, it is relevant to note, first of all, that the modified methods of lines using, respectively, 101 and 161 lines agree very well with each other, the worst discrepancy being 0.24%. Based on this, we believe that our numerical scheme is reliable.

Comparison between the variational and direct numerical results shows that their differences range from about 2% to about 6%. Generally, the discrepancies are larger very close to the bifurcation points. This is understandable because, as shown in Figs. 3.2 through 3.5, the fields change rapidly with  $Q$  near these points. Particular results of the comparison are displayed in Table 3.1.

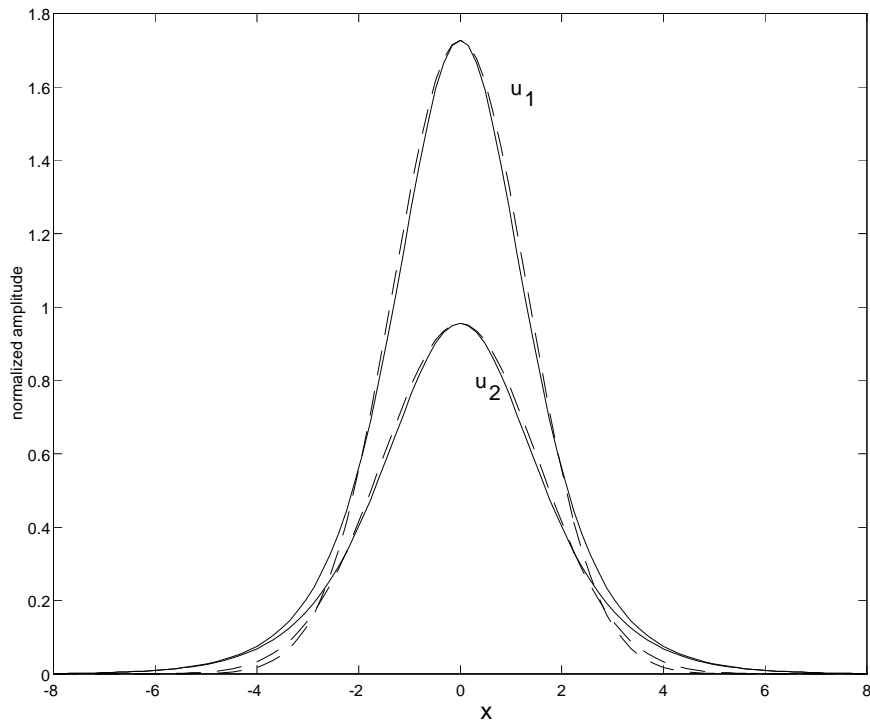


Figure 3.8: The shape of the asymmetric soliton at  $K = 0$ ,  $Q = 0.5$ . Shown are the FH components  $u_{1,2}$ . The solid line is the result obtained from the numerical method, and the dashed line is generated by the variational approximation.

As a typical case, we show in Fig. 3.8 the shape of the asymmetric soliton at  $K = 0$  and  $Q = 0.5$ , as obtained from both VA and the modified method of lines. It can be seen that the agreement is very good; the largest deviations are at the skirts of the soliton. The shape produced by VA is narrower there, which is a natural drawback of the Gaussian ansatz. This feature is generic for all the values of  $K$  and  $Q$ .

	Discrepancies							
$K$	0.7		0.4		0.0		0.3	
$Q$	0.8	0.874†	0.5	0.725†	0.05	0.56†	0.35	0.425†
ML‡	0.03%	0.01%	0.06%	0.04%	0.08%	0.09%	0.08%	0.24%
VA‡	2.9%	5.3%	2.4%	2.9%	2.1%	3.2%	2.3%	5.5%

†: these columns correspond to points close to the bifurcation points

‡: method of lines, using 101 lines

‡: variational method.

Table 3.1: Sensitivity Analysis (discrepancies when compared with method of lines using 161 lines)

### 3.4 The Stability Analysis

In this section, we will study stability of the stationary solutions found in the previous section. The Jacobian matrices obtained in Subsection (3.3.3) were used for a straightforward linear stability analysis, by evaluating its eigenvalues, which is a well-established method, see, e.g., [61] for details.

We use the results of the method based on 101 lines, which means discretizing the variable  $x$  at 101 points. The corresponding Jacobian matrices will thus have 404 eigenvalues. If any of these eigenvalues is positive, the stationary solution is regarded to be unstable. Since the calculation of the eigenvalues is straightforward (being a standard feature of the software used), the linear stability was tested for all the stationary solutions found.

Without exception, all the stationary solutions considered (including the symmetric ones) have at least one positive eigenvalue. This, however, does not mean

that all the solutions are truly unstable. Indeed, in the conservative system, the stability may be only neutral, implying the existence of at least one zero eigenvalue in the linear stability analysis. This fact was observed, for the limit case  $K = Q$ , in the last chapter, in the form of very persistent, nongrowing and nondecaying, internal vibrations of the asymmetric soliton generated by a small perturbation in the initial conditions. In the numerical computations, however, the zero eigenvalue can easily turn out to be a tiny positive one because of the numerical errors. On the other hand, this implies that the straightforward numerical calculation of the stability eigenvalues does not provide for the final answer, and direct simulations of the PDE's (3.1) with perturbed initial conditions are necessary. The stability was thus tested directly by means of the Split-step Fourier method.

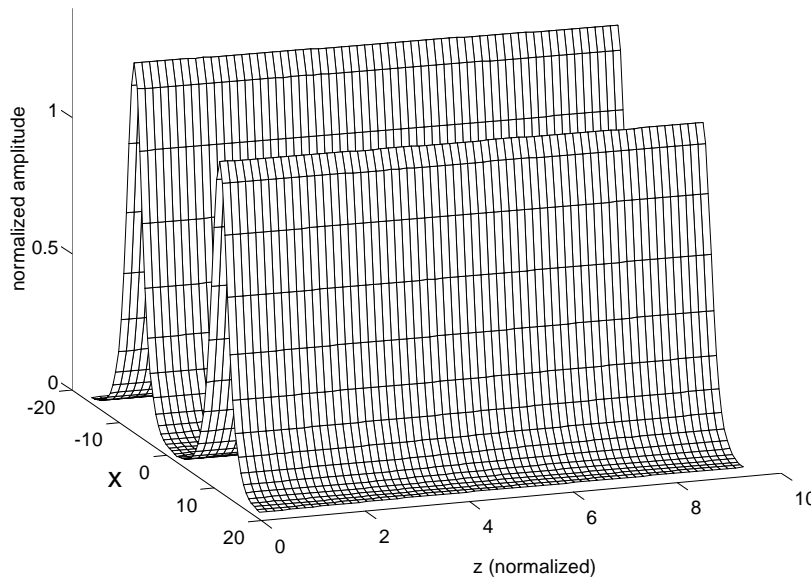


Figure 3.9: Evolution of a slightly disturbed asymmetric soliton at  $Q = 0.7$  and  $K = 0.3$ . Shown are the fundamental harmonic fields in both waveguides. Distance of propagation simulated was  $3\pi$ .

The conventional method of lines, that was used above to produce the stationary soliton solutions, can also be used to solve the PDE's. However, we did not use this method to tackle the stability problem, because, when formulated as above to obtain the stationary solutions, the method turns out to be very inefficient for the PDE integration. Instead, we used the split-step Fourier method. The study of the stability was performed at various points in the parametric space where the asymmetric solitons exist. The selected points were

$$(K, Q) = (0.3, 0.7); (0.1, 0.4); (0, 0.4); (0, 0.56); (0, 0.566); \\ (0.2, 0.45); (0.3, 0.4).$$

They were chosen so that areas close to and far from the bifurcation points, as well as the regions with positive and negative values of the coupling constants, were all tested.

The results of this analysis are in complete agreement with the inferences formulated in the last chapter: *All* the asymmetric solitons were found to be neutrally stable. This means that, slightly perturbed, the solitons will undergo minor fluctuations around the stationary solutions over very long distances. The fluctuations do not have any sign of decay, but they are not growing either. This is exactly the same behaviour as observed in the last chapter. A quite typical example of the evolution of a slightly perturbed asymmetric soliton is displayed in Fig. 3.9, which depicts a case of  $Q = 0.7$  and  $K = 0.3$ . This figure displays simultaneously the FH components of the soliton in both waveguides.

We also checked the stability of the symmetric solitons which coexist with the asymmetric ones. Exactly as expected, the symmetric solitons are *always* destabilized by the bifurcation. This is illustrated by Fig. 3.10. It shows that the unstable

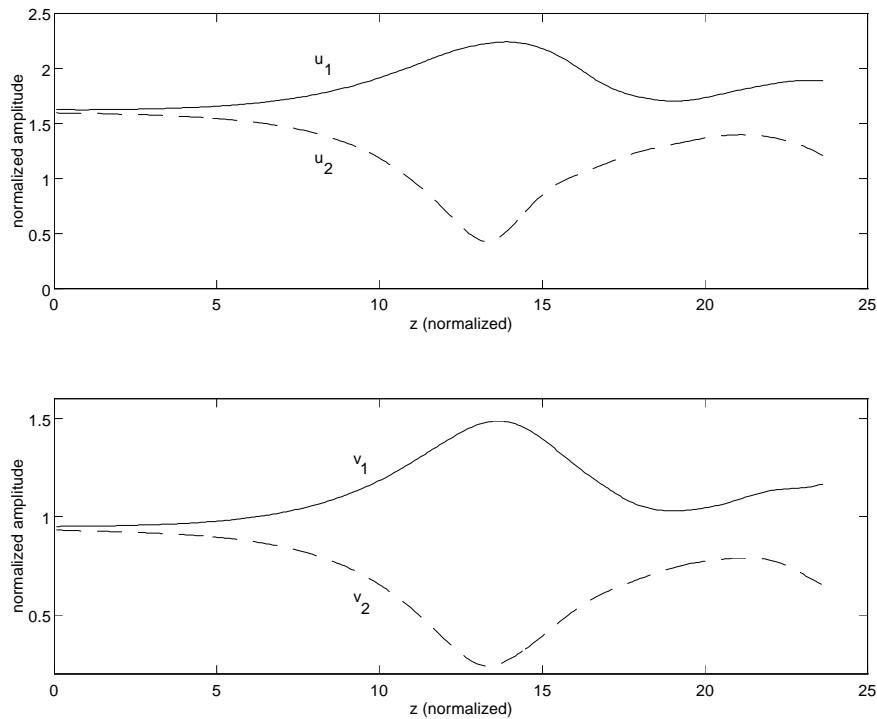


Figure 3.10: Evolution of the peak values of the unstable symmetric soliton at  $Q = 0.4$  and  $K = 0$ . This figure illustrates evolution towards the stable asymmetric soliton.

symmetric soliton suffers spontaneous symmetry breaking and shows a trend to rearrange itself into a stable asymmetric soliton which exists at the same values of the coupling constants. However, damping of the internal vibrations of the resultant strongly perturbed soliton is so weak that there is no sign of settling down even after a long distance.

For unstable symmetric solitons closer to bifurcation points, simulations show that the process of evolution is even slower. As depicted in Fig. 3.11, even after a long distance, the separation of the symmetric soliton is still quite barely noticeable. Comparison of Figs. 3.10 and 3.11 shows that symmetric solitons further away from bifurcation points are more unstable than those closer to bifurcation points.

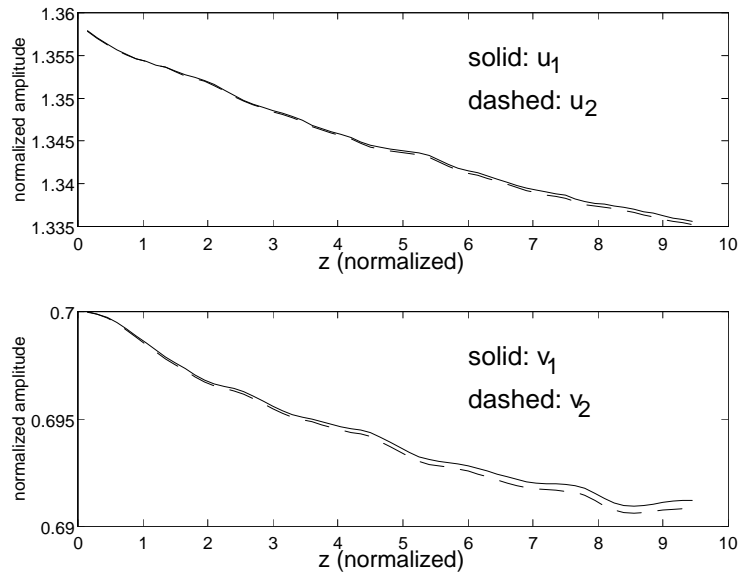


Figure 3.11: The evolution of the peak values of an unstable symmetric soliton at  $Q = 0.566$  and  $K = 0$ , (close to a bifurcation point). The evolution towards the asymmetric soliton state is very slow.

### 3.5 Conclusion

In this chapter, we reported results of analytical and numerical consideration of solitons in a system of two linearly coupled second-harmonic-generating waveguides. We consider the system with arbitrary coupling constants for the fundamental and second harmonics. Two regions of existence of nontrivial asymmetric soliton states, along with bifurcation lines at which they bifurcate from obvious symmetric solitons, are identified. The analytical approach is based on the variational approximation, which, different from the last chapter, used a Gaussian ansatz. It provides better

flexibility in allowing one to use different widths for the different component waves. This variational analysis is then followed by direct numerical solution of the stationary ordinary differential equations. The analytical and numerical results are found to be in fairly good agreement, except for a very narrow parametric region, where the second-harmonic component of the soliton is changing its sign, having a non-monotonous shape. We further establish the stability of the asymmetric solitons, simulating the corresponding partial differential equations, and simultaneously show that the co-existing symmetric solitons are unstable. In the next chapter, we will analyze in detail effects of a walkoff (spatial misalignment) between the two cores. We will also consider cases when the phase mismatch inside each waveguide to be arbitrary.

# Chapter 4

## Secondary Effects

### 4.1 Introduction

Coupled waveguides can have important applications in photonics, e.g., as all-optical switches [62, 63]. It has also been proposed to use dual core fiber coupler as soliton compressor and splitter, achieving smaller pedestal [64], as nonlinear optical loop mirror with self-switching [65].

For couplers in quadratically nonlinear medium, systematic theoretical results for solitons in a model of parallel-coupled identical waveguides have been reported very recently [66, 67]. The detailed results of this investigation were elaborated in the previous two chapters. In this chapter, we will begin by considering the case when the optical solitons do not have their wave vectors in parallel directions, i.e., there is a spatial walkoff, manifested as the terms,  $+i\delta u_x$  and  $-i\delta u_x$ . (The walkoff parameter  $\delta$  was put to zero in the two previous chapters.) The inclusion of these “walkoff” terms in the investigation of solitons in cubic nonlinear medium appeared in a number of papers, e.g., [68, 69, 70]. Such terms can also be found

in the investigations of *gap solitons* [71, 72, 73], in which such terms represent the grating induced dispersion or diffraction, although then, the material second-derivative dispersion or diffraction terms,  $u_{xx}$ , need to be dropped off because they are much weaker in comparison.

For  $\chi^{(2)}$  solitons in a single waveguide, investigations were carried out with the phase mismatch as a varying parameter [58, 74, 75, 76], and a stability threshold in terms of the phase mismatch parameter is known. In this chapter for coupled  $\chi^{(2)}$  waveguides, we will also investigate the case when the assumption of fully phase match as in the last two chapters is dropped.

Usually, in the study of optical couplers, the two cores of the coupler are assumed to be identical. However, in reality, the cores will seldom be identical, and, furthermore, a fiber with dissimilar cores can easily be fabricated and may even find interesting applications [17, 18].

It had been shown that the asymmetric couplers, with one linear core, and one nonlinear core, with either quadratic or cubic nonlinearity, are superior in performance, when compared with symmetric couplers with identical cores [45, 77]. The asymmetric couplers do not exhibit the undesirable throughput oscillations, which are found in symmetric couplers.

An application was also proposed to use asymmetric couplers as logic gates [78]. The asymmetric coupler there consisted of two single-mode fibers with different cubic nonlinearity constants, which were implemented by using fiber cores of the same material but different core radii.

In [79], soliton solutions were considered to equations describing a pair of tunnel-coupled asymmetric cubic nonlinear optical fibers, the asymmetry being a phase-velocity mismatch between them. Two bifurcations were found: one involved a ter-

mination of a branch whose solitons have components of the opposite sign; the other linked with the occurrence of a hysteresis-type behavior of another branch, whose solitons have the same signs of their components. The hysteresis-type behaviour of the second bifurcation might be of interest for applications, such as switching.

For other applications, it has been suggested to use asymmetric coupler as all-fiber Brewster window [80], as highly broadband splitter [81, 82]. Using an asymmetric coupler geometry, it has been shown that a higher efficiency can be achieved in designing a semiconductor ring laser [83].

From this survey, it can be seen that asymmetric coupler is a very useful configuration. So, in the last part of this chapter, we will investigate solitons in asymmetric couplers with quadratic nonlinearity. We will consider two types of asymmetry: one case is that the phase mismatch parameters between the fundamental harmonic and the second harmonic in the two cores are different; the other case is that one core is nonlinear, while the other core is linear.

## 4.2 Effects of Spatial Walkoff

A general model to describe the co-propagation of FH  $u$  and SH  $v$  in the linearly coupled waveguides was put forward in the last two chapters, and is repeated here for convenience:

$$iu_{1z} + i\delta u_{1x} + \frac{1}{2}u_{1xx} \quad qu_1 + u_1^*v_1 = \quad Qu_2, \quad (4.1)$$

$$2iv_{1z} + 2i\delta v_{1x} + \frac{1}{2}v_{1xx} \quad v_1 + \frac{1}{2}u_1^2 = \quad Kv_2, \quad (4.2)$$

$$iu_{2z} \quad i\delta u_{2x} + \frac{1}{2}u_{2xx} \quad qu_2 + u_2^*v_2 = \quad Qu_1, \quad (4.3)$$

$$2iv_{2z} \quad 2i\delta v_{2x} + \frac{1}{2}v_{2xx} \quad v_2 + \frac{1}{2}u_2^2 = \quad Kv_1, \quad (4.4)$$

where all the symbols carry the same meanings as before.

In this section, we will concentrate on the effects of the spatial walkoff terms. The study is by means of direct PDE simulations (using the Split-step Fourier method as discussed in Section (2.4.1)), keeping the walkoff terms in Eqs. (4.1) - (4.4), which had been omitted in previous chapters.

Firstly, we demonstrate that the asymmetric solitons are *not* destabilized by the walkoff effect if the walkoff is small enough. In Fig. 4.1, we illustrate the evolution of an asymmetric soliton under the action of a small walkoff. In this case,  $K = 0$ ,  $Q = 0.5$ , and  $\delta = 0.05$ . For typical nonbirefringent Group III-V semiconductor crystals, with a refractive index of 3.5, coherence length of around  $10 - 100\mu m$ , and a typical wavelength of about  $1\mu m$ , [84], this corresponds to an actual misalignment of around  $0.11 - 0.34$  degrees between the beams in the two waveguides (This physical value can be deduced from the normalized value of  $\delta$  by reversing the normalization procedure as described in Section (1.4.2) of Chapter 1). Actually, available experimental techniques allow us to make the misalignment essentially smaller than this, so these values are quite relevant to estimate limits of the soliton's stability against the walkoff. The total distance of travel simulated was  $3\pi$ .

In Fig. 4.2, we illustrate the evolution of another soliton when the walkoff is larger. In this case,  $\delta = 0.5$ ,  $K = Q = 0.7$ . The total distance of travel simulated is  $\pi$ . It can be seen that the shapes of the soliton components get distorted, and skew to one side. It can be also seen that the smaller of the soliton components in the two waveguides gets trapped by the larger soliton component and pulled to travel in the same direction.

In Fig. 4.3, we summarize the distortion effect inflicted on the soliton as both the

walkoff parameter  $\delta$  and the coupling constants,  $K$  and  $Q$  are varied (we consider here the case  $K = Q$ ). We quantify the distortion by defining

$$D = \frac{\int_{W_1} |u_1^2 - u_{1i}^2| d\zeta}{\int_{W_1} u_{1i}^2 d\zeta}, \quad (4.5)$$

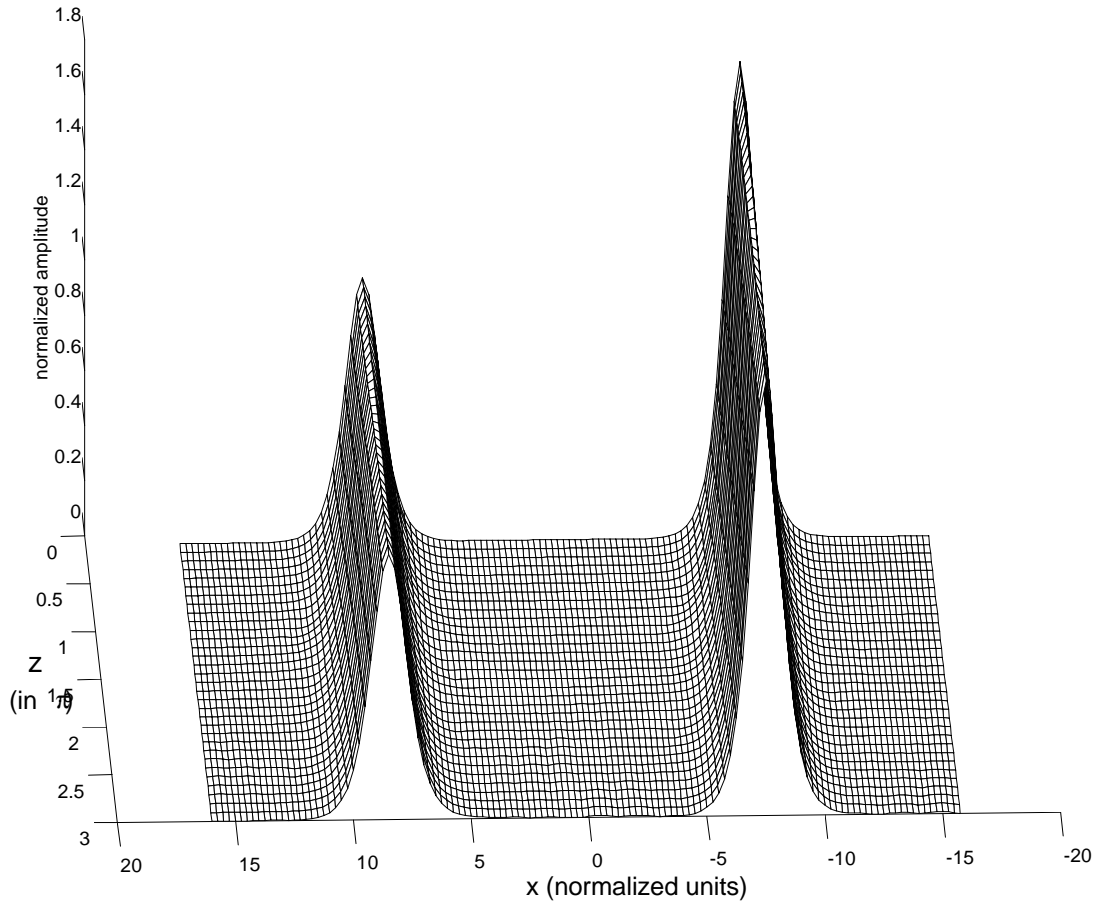


Figure 4.1: Evolution of the asymmetric soliton at  $Q = 0.5$ ,  $K = 0$  under the influence of the walkoff effect with  $\delta = 0.05$ . Only the FH components are shown. The slanting propagation directions are due to the walkoff terms. Distance of propagation simulated was  $3\pi$ .

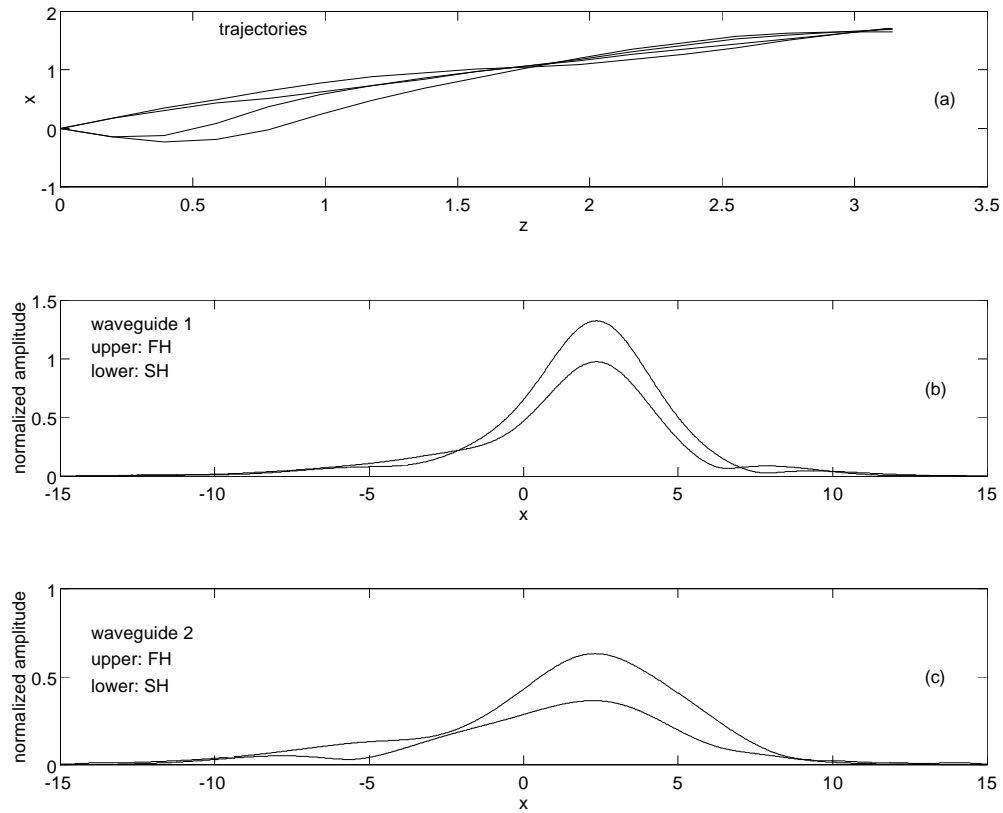


Figure 4.2: Evolution of soliton when walkoff is larger.

(a) Trajectories of the peak values of the soliton components. Initially, the upper two traces are those of the FH and SH in waveguide 1, and the lower two traces are those in waveguide 2. It can be noted that they travel in opposite directions. However, the smaller waves in waveguide 2 are finally pulled by the larger waves in waveguide 1 and trapped to follow their direction of travel. (b) The shapes of the soliton components in waveguide 1 and (c) the shapes of the soliton components in waveguides 2, after propagating over a normalized distance of  $\pi$ . In this analysis,  $K = Q = 0.7$ ,  $q = 1$ , and  $\delta = 0.5$ . It can be seen that the walkoff distorts the soliton, making the waveforms to skew to one side.

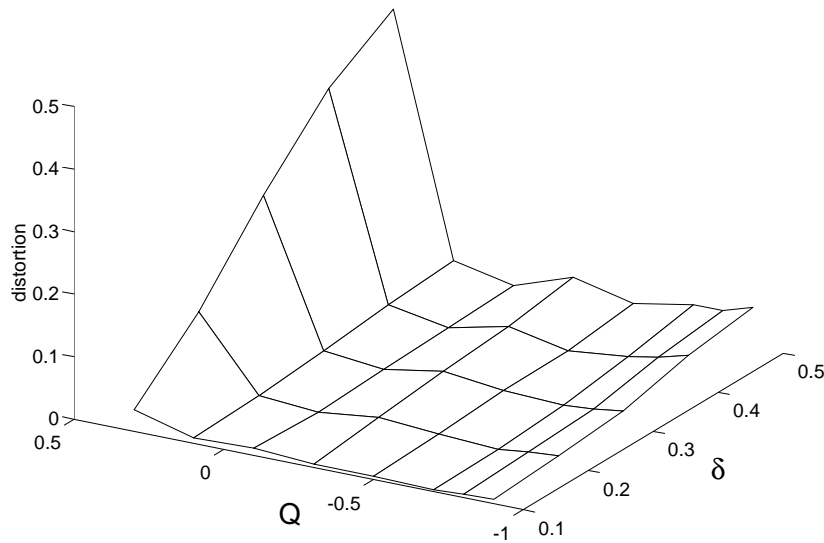


Figure 4.3: Distortion as a function of walkoff parameters  $\delta$  and coupling constant  $Q$ . In this analysis,  $K = Q$ , and distortion is shown after a propagation distance of  $\pi$ . In general, the distortion is larger for larger walkoff, and stronger coupling (where the solitons get more symmetric).

where the integrations are confined within the beam width (the spot size),  $W_1$ , as defined in Eq. (3.27) in Chapter 3.  $u_1$  is the FH in waveguide 1 after the propagation distance of  $\pi$ , and  $u_{1i}$  is the same wave field at the input ( $z = 0$ ). The integrations are done with respect to the transverse coordinate,  $\zeta$ , in the reference frame which travels together with  $u_1$ .

It can be seen that, in general, the distortion becomes larger as  $\delta$  gets larger. Also, distortion is larger for larger absolute values of the coupling constants. This trend is very prominent for positive  $Q$ : as one sees in Fig. 4.3, the distortion produced by a fixed value of  $\delta$  steeply increases with the increase of  $Q > 0$ , quickly leading to destruction of the soliton. Because the solitons become more symmetric

with the increase of the absolute values of the coupling constants, we can interpret this trend as an effect of pulling apart of two soliton components (referring to the two cores) having nearly equal energies.

We also considered the walkoff-induced deformation of the stable symmetric solitons, existing before the bifurcation. For instance, in the case  $K = Q = 0.4$ , we observed that, in the presence of quite a strong walkoff,  $\delta = 0.4$ , both components of the soliton developed conspicuous side lobes after having travelled a long distance,  $z = 3\pi$ . As walkoff becomes even larger, at  $\delta = 0.6$ , the components in the two cores get pulled apart into the lobes, and they are no longer trapped together to travel in the same direction, which we interpret as destruction of the soliton at some  $\delta$  between 0.4 and 0.6.

### 4.3 Effects of Varying the Phase Mismatch

Effects produced by varying the mismatch parameter  $q$  are important in practice, and they turn out to be rather easy to investigate. Running the numerical analysis, using the relaxation method (see descriptions in Section (3.3.2) & (3.3.3)) with different values of  $q$ , we have found that, as it gets smaller, the regions where asymmetric solitons can exist shrink; the opposite happens when  $q$  gets larger. In fact, as  $q$  gets larger, the asymmetry gets larger very rapidly ( $\Theta_F$  and  $\Theta_S$ , which were defined in Eqs. (3.25) & (3.26) of the last chapter, become very close to 1 ). This means the fields stay largely in one waveguide and are absent in the other; there is negligible coupling, thus, the two waveguides get effectively decoupled at a large phase mismatch.

Fig. 4.4 shows the plots of the asymmetry parameters,  $\Theta_{F,S}$ , versus the FH

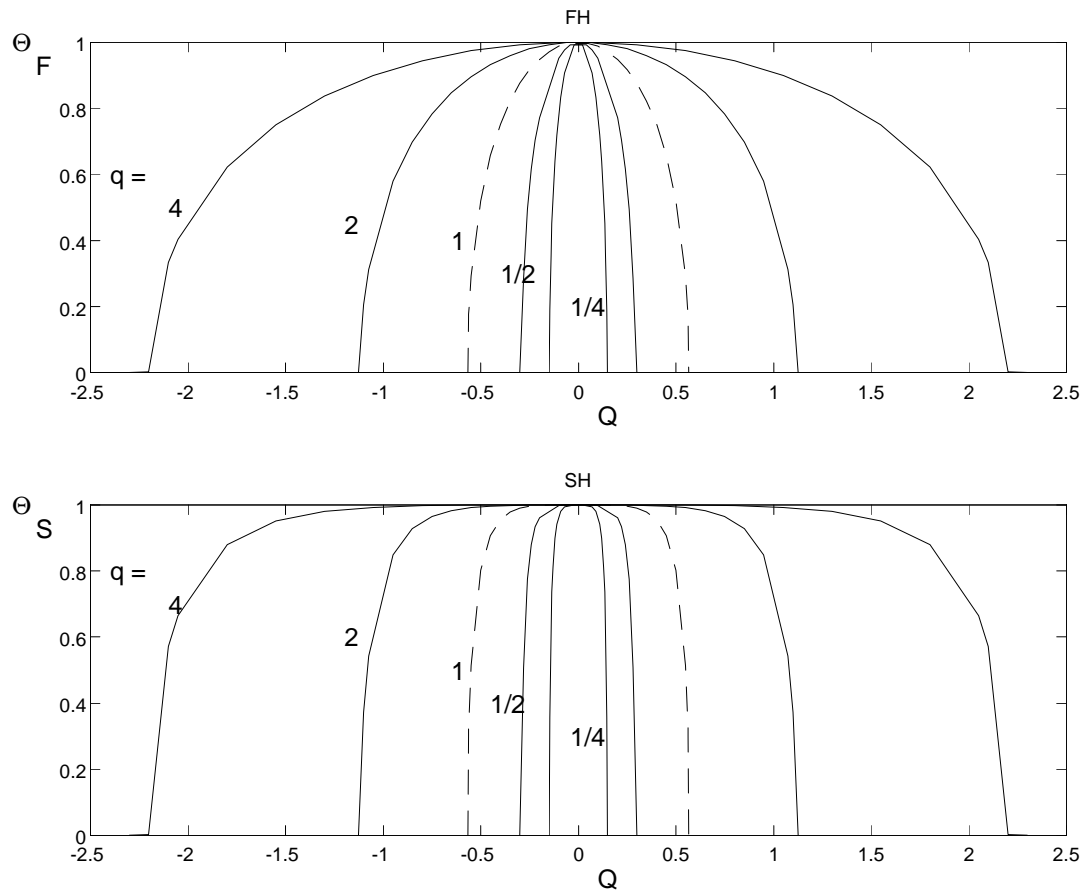


Figure 4.4: The asymmetry parameter,  $\Theta_{F,S}$ , as functions of the FH coupling constant  $Q$ .

coupling constant  $Q$  for a fixed value of the SH coupling constant  $K$  of 0, with the phase mismatch  $q$  as a changing parameter, taking on values 0.25, 0.5, 1, 2, and 4. It can be seen that the regions where the asymmetric solitons exist expand as  $q$  gets larger. Note that the dashed curves, corresponding to  $q = 1$ , are cross-sections of the bifurcation diagrams shown in Figs. 3.2 and 3.3 in the last chapter. Similar analyses had been done for  $K = 0.5$  and  $K = 0.3$ . The results are not displayed here as they do not produce anything essentially different. To show the effect of even larger values of  $q$ , we include Figs. 4.5 and 4.6, for the cases  $K = Q$  and  $K = 0$ , respectively, which show that the asymmetry stays relatively constant as  $q$

is increased beyond about 4.

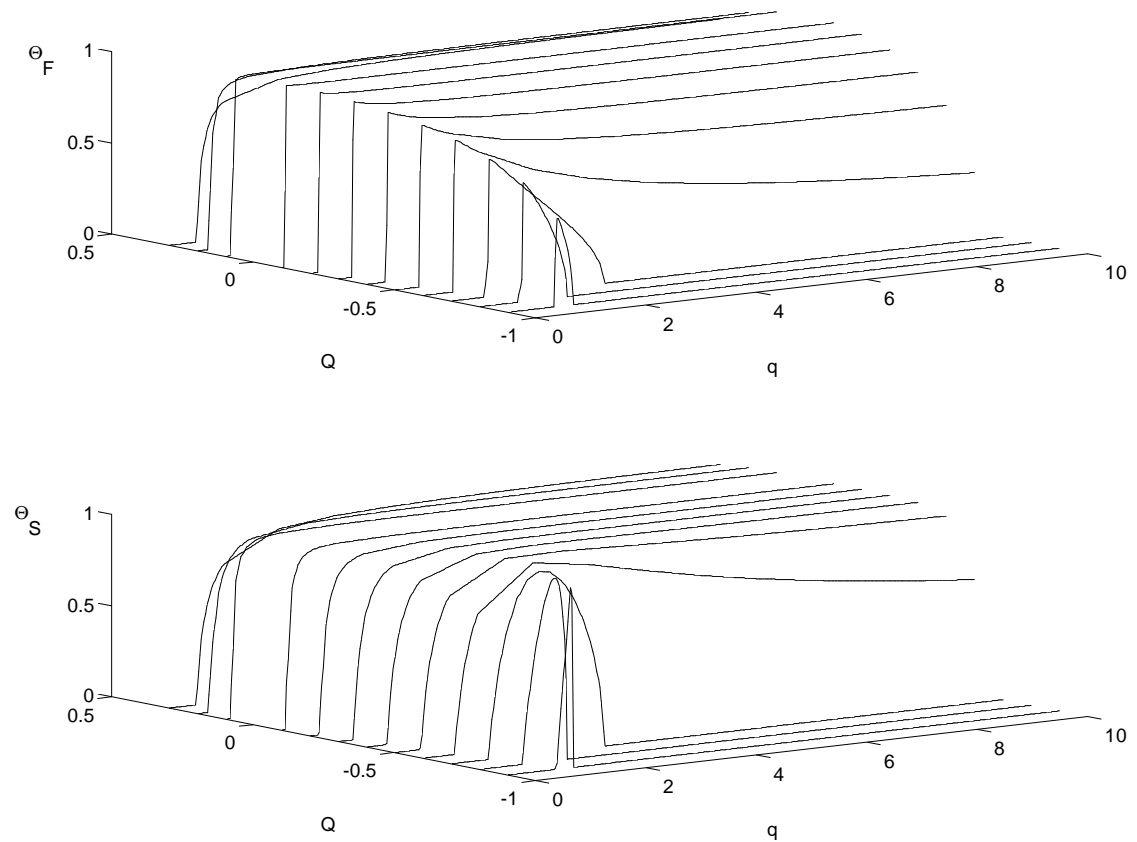


Figure 4.5: The bifurcation diagrams as a function of the coupling constant  $Q$  and phase mismatch  $q$  for the case  $K = Q$ .

The case of very small values of  $q$  can be easily considered by means of an approximation for the single-core waveguides (one should bear in mind that our parameter  $q$ , entering the FH equations, is the inverse of the frequently defined mismatch parameter  $\alpha$  in the equation for SH, see e.g. [76]). Namely, one assumes that, in Eqs. (4.2) and (4.4), it is possible to neglect all the terms but the last two terms on the left-hand sides, so that SH can be eliminated in favor of FH:  $v_n \approx \frac{1}{2}u_n^2$  ( $n = 1, 2$ ). Substitution of this into Eqs. (4.1) and (4.3) immediately yields a system

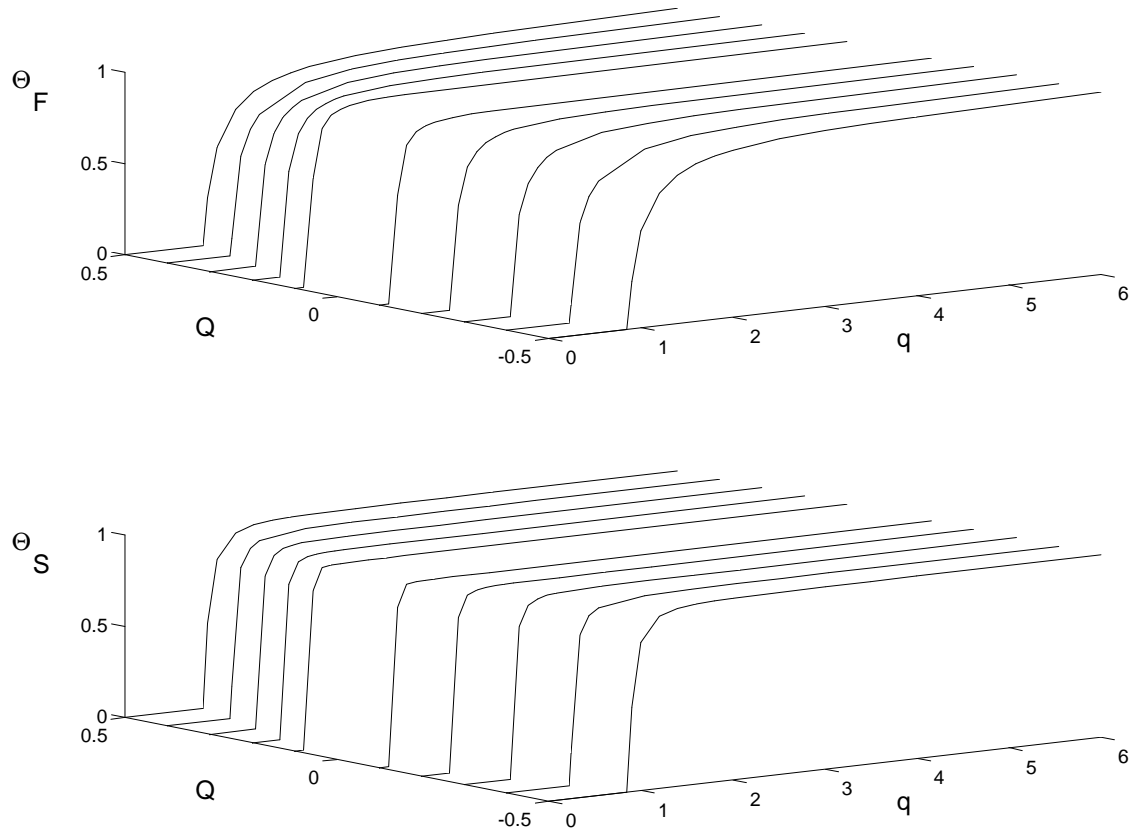


Figure 4.6: The bifurcation diagrams as a function of the coupling constant  $Q$  and phase mismatch  $q$  for the case  $K = 0$ .

of two linearly coupled *cubic* nonlinear Schrödinger equations for the FH fields  $u_n$ , which is identical to that considered in detail earlier in the context of the twin-core nonlinear optical fibers [17, 24].

## 4.4 Asymmetric Coupler

In this section, we consider solitons in asymmetric couplers with the quadratic nonlinearity. Since the two crucial length scales (the diffraction and coupling lengths)

are on the same order of magnitude (a few millimeters) [24, 43], which applies to the asymmetric couplers as well, so a soliton in this system is a physically realistic object. We will be dealing with two different types of dissimilarity between the cores. First, we study couplers with cores which have different intrinsic phase mismatches between the fundamental harmonic (FH) and the second harmonic (SH). Here, we consider two limiting cases, viz., those when the cores are closely spaced or, on the contrary, are widely separated. This kind of asymmetric coupler can be fabricated quite easily. One way to do so is to give the waveguides different cross-sectional shapes, while keeping their effective cross-sectional areas equal, so that they have equal nonlinear constants, which will be assumed below.

Then, we consider another type of the asymmetry, namely, a limiting case when one of the cores is purely linear, while the other one has the quadratic nonlinearity. This case can also be readily realized, by simply using different materials for the two cores. It was found that for cw beams in such a coupler, complete switching can be achieved without the detrimental oscillations observed in the coupler with the identical nonlinear cores [77].

We will present detailed bifurcation diagrams for solitons existing in these couplers. These diagrams are of twofold interest, as a description of a fundamental physical object, and, also, for understanding the switching properties of the asymmetric couplers in the soliton regime when they are used as optical switches.

#### 4.4.1 Mathematical Model

A general model which describes the stationary distribution of FH and SH amplitudes in two coupled quadratically nonlinear waveguides was put forward in the two

previous chapters, and repeated in Section (4.2). In this section, the equations are slightly modified as below (so that the frequently used phase mismatch parameters  $\alpha_{1,2}$  in the equations for SH are used instead of the parameter  $q$  which was used previously):

$$i(u_1)_z + \frac{1}{2}(u_1)_{xx} \quad u_1 + u_1^*v_1 = Qu_2, \quad (4.6)$$

$$2i(v_1)_z + \frac{1}{2}(v_1)_{xx} \quad \alpha_1v_1 + \frac{1}{2}u_1^2 = Kv_2, \quad (4.7)$$

$$i(u_2)_z + \frac{1}{2}(u_2)_{xx} \quad u_2 + u_2^*v_2 = Qu_1, \quad (4.8)$$

$$2i(v_2)_z + \frac{1}{2}(v_2)_{xx} \quad \alpha_2v_2 + \frac{1}{2}u_2^2 = Kv_1. \quad (4.9)$$

We will, first of all, investigate the effect of the asymmetry due to different phase mismatch between the two harmonics in each core, i.e.,  $\alpha_1 \neq \alpha_2$ . We will analyze in detail two limiting cases of the closely spaced or widely separated cores, the former being dealt with by setting the FH and SH coupling constants  $Q$  and  $K$  equal, while the latter is accounted for by neglecting the  $K$  in comparison with  $Q$ , i.e., setting  $K = 0$  (see Ch. 3). The other case which is worthy special consideration is that when one core is quadratically nonlinear while the other one is purely linear [77]. In this case, we simply omit the nonlinear terms in Eqs. (4.8) & (4.9), keeping arbitrary couplings constants  $Q$  and  $K$ .

#### 4.4.2 Results

A peculiarity of the  $\chi^{(2)}$  models is that they are far from any integrable limit, so that almost no property of the soliton solutions can be obtained in an analytical form, the only exception being the particular exact solution in the single-core model at  $\alpha = 1$ , found long ago by Karamzin and Sukhorukov [50, 51]. That is why general

results can only be obtained numerically [43], or, sometimes, in a semianalytical approximate form based on the variational approach. For the first time, the variational approximation was applied to the  $\chi^{(2)}$  model in the work [39], and in [66, 67], it was quite efficiently developed for the solitons in the symmetric  $\chi^{(2)}$  coupler. This had been elaborated in the last two chapters. However, the variational approximation gets messy for more sophisticated models containing a large number of parameters. Therefore, in the present work, we have carried out the analysis using direct numerical techniques. We used the same finite difference scheme as before (see Sections (3.3.2) & (3.3.3)) to trace out all the stationary spatial-soliton solutions. The stability of the solitons can be partially predicted, using the standard theorems of the bifurcation theory [86]; however, in this work, we further tested the stability by means of direct simulations, using the well-known Beam Propagation Method (BPM) (see Section (2.4.1)).

In view of the necessity to analyze the soliton solutions in the  $\chi^{(2)}$  models by numerical methods, and because of the presence of several physically meaningful control parameters, as done in earlier chapters, I present the results here in the form of plots, *bifurcation diagrams*, showing the dependence of the important parameters of the solitons (e.g., the energy ratios  $\Theta_{F,S}$ ) vs. the control parameters. The bifurcation diagrams display both a smooth variation of established solutions with the change of the control parameters, and the *bifurcations*, i.e., qualitative rearrangements of the solutions at some critical points. The bifurcations are of major interest not only by themselves, but for applications too, as a bifurcation exactly indicates *switching* in the corresponding nonlinear optical device.

#### 4.4.2.1 Different Phase Mismatch, Closely Placed Cores

As a reference, the phase mismatch factor for waveguide 2 was kept constant,  $\alpha_2 \equiv 1$ , while the control parameter  $\alpha_1$ , the phase mismatch in the first waveguide, was varied from 0.25 to 8. Typical results for  $\alpha_1 > 1$  are depicted in Fig. 4.7, which are plots of the asymmetry parameters  $\Theta_F$  and  $\Theta_S$  vs. the coupling constant  $Q$  (recall that the closely spaced cores imply  $K = Q$ ). It is obvious that  $\Theta_F = \Theta_S = 1$  at  $Q = 0$ , because the fields are absent in one of the waveguides in the absence of the linear coupling. As expected from the bifurcation theory, the branches of the bifurcation diagram for the symmetric coupler (the dotted line in Fig. 4.7) unfold to closed loops above the horizontal axis, and to open curves below it. (Typical examples of similar unfolding of bifurcation diagrams can be found in e.g., [61].) As  $\alpha_1$  gets larger, the branches deviate more from the dotted lines.

The same bifurcation diagram for  $\alpha_1 < 1$  is shown in Fig. 4.8, for a (typical) particular value  $\alpha_1 = 0.25$  (while  $\alpha_2$  is kept at 1). The unfolding is different from that in Fig. 4.7, mainly at large negative values of  $Q$ . The loops for FH get open and those for SH cross. The finite-difference scheme that was used to obtain the soliton states becomes inaccurate at large negative values of  $Q$ . The reason is that the widths of the soliton diverges as  $Q \rightarrow -1$ , hence the size of the integration domain needs to be expanded. With a fixed number of the grid points, this implies deterioration of the accuracy. However, because it is clear that the soliton disappears in the limit  $Q \rightarrow -1$ , getting infinitely broad, we did not try to trace this with a great accuracy.

The bifurcation diagram for  $\alpha_1 = 0.5$  has also been obtained; however, it is not displayed here, because it looks quite similar to that shown in Fig. 4.8, but with a

smaller deviation from the bifurcation diagram of the fully symmetric coupler.

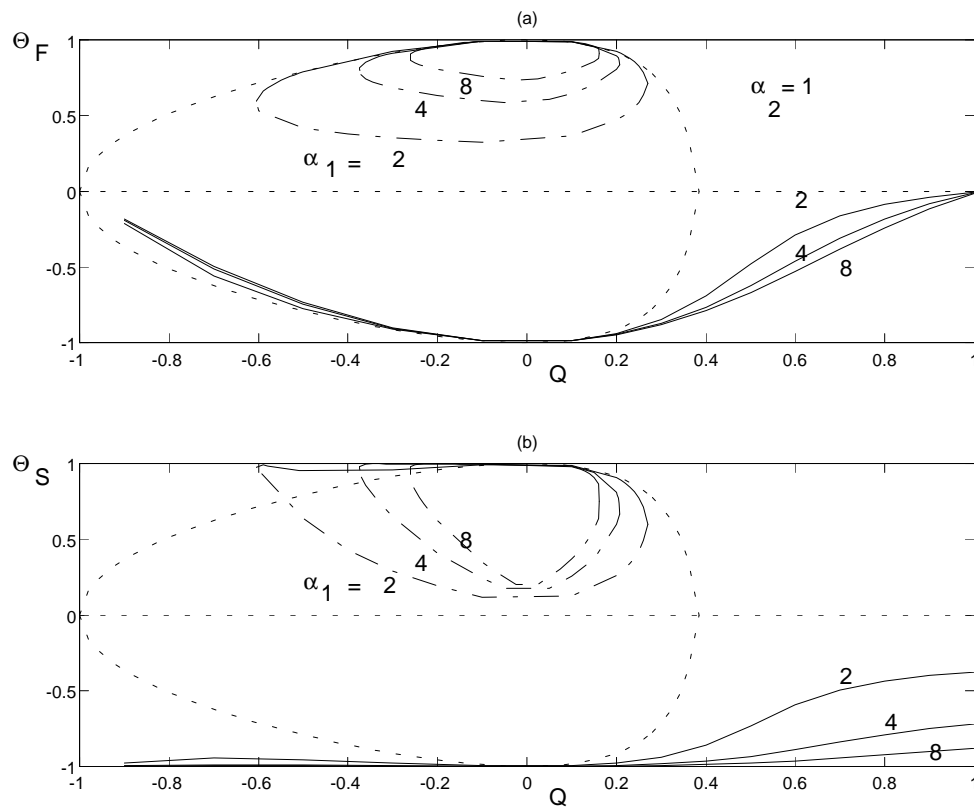


Figure 4.7: Bifurcation diagrams for closely placed asymmetric cores

(the case  $K = Q$ ) with a difference in the phase mismatch: (a) the FH component; (b) the SH component. The phase mismatch factor of core 1,  $\alpha_1$ , takes on the value 2, 4, and 8, while in the second core we set  $\alpha_2 \equiv 1$ . The bifurcation diagram for the corresponding symmetric coupler is also included as a reference (by the dotted lines).

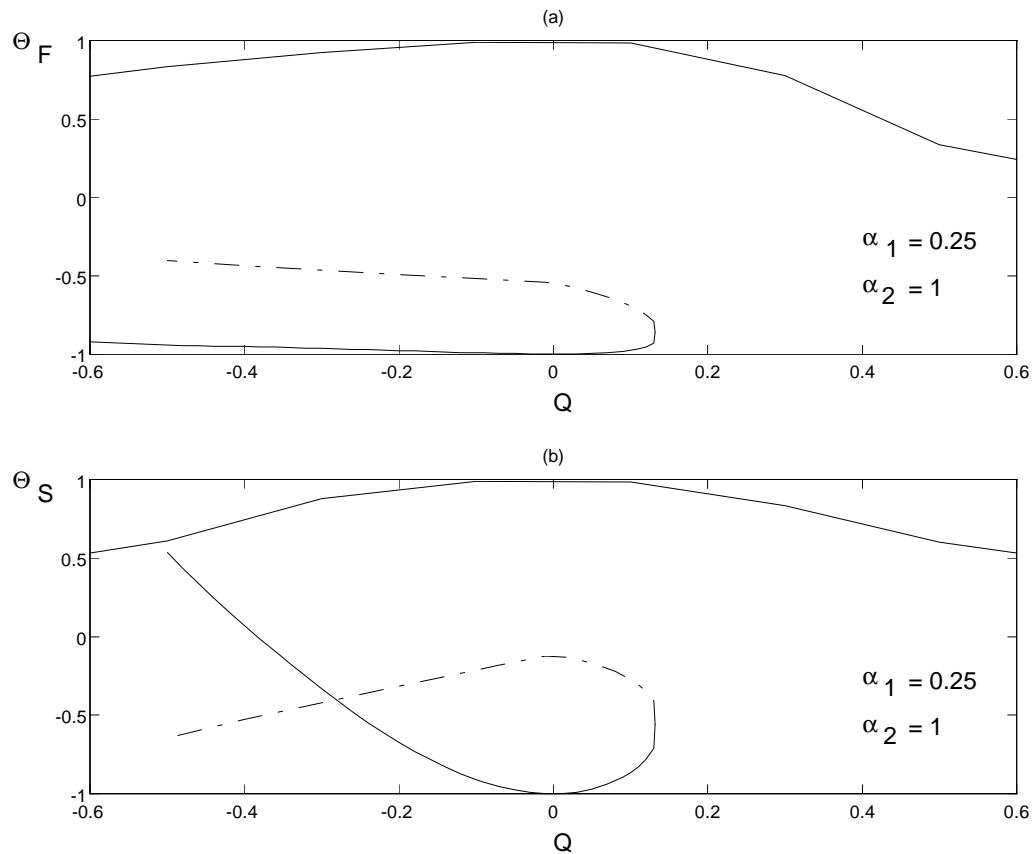


Figure 4.8: Bifurcation diagrams for closely placed asymmetric cores (the case  $K = Q$  and  $\alpha_1 = 0.25$ ): (a) the FH component; (b) the SH component.

#### 4.4.2.2 Different Phase Mismatch, Widely Separated Cores

In this case, we set  $K = 0$ . Similar to the previous case of  $K = Q$ , the phase-mismatch factor for waveguide 2,  $\alpha_2$ , was kept constant, while the one for waveguide 1,  $\alpha_1$ , is varied. The unfolding of the bifurcation diagram, starting from that corresponding to the fully symmetric coupler, is shown for this case in Fig. 4.9. The unfolding looks as expected from the bifurcation theory. It can be seen that, here, the bifurcation diagrams are all symmetric about  $Q = 0$ .

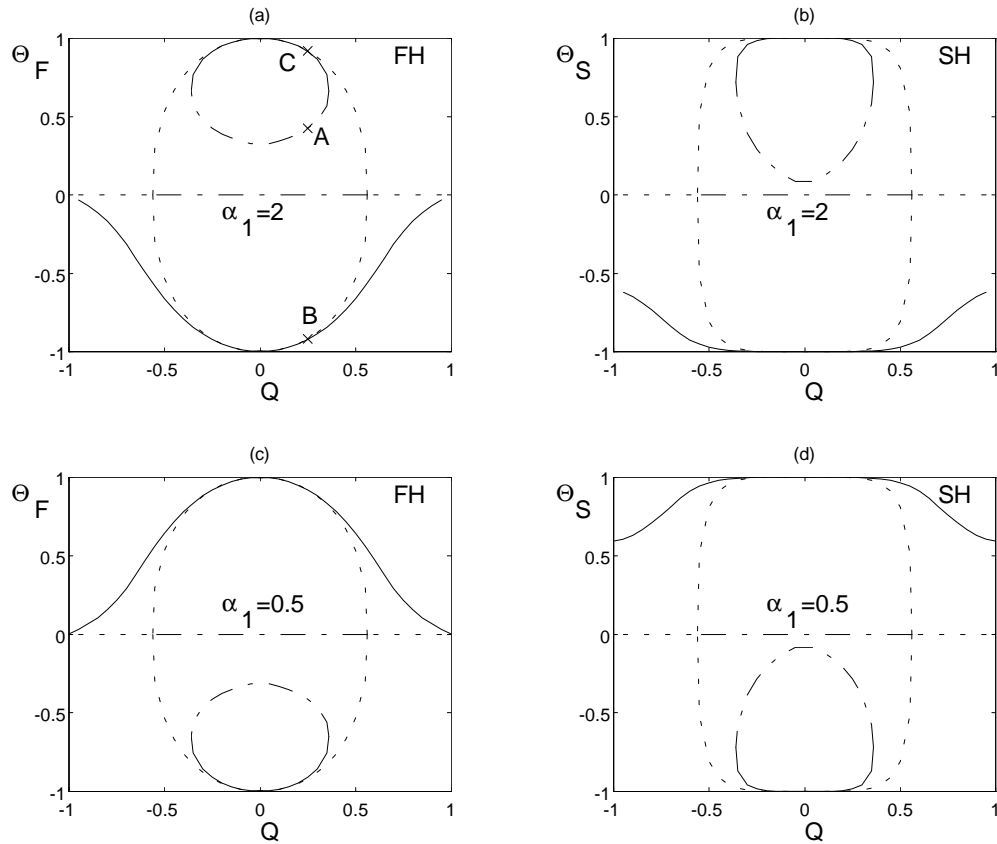


Figure 4.9: Bifurcation diagrams for widely separated asymmetric cores (the case  $K = 0$ ) with different phase mismatch:

(a)  $\alpha_1 = 2$ ,  $\alpha_2 = 1$ , the FH component; (b)  $\alpha_1 = 2$ ,  $\alpha_2 = 1$ , the SH component; (c)  $\alpha_1 = 0.5$ ,  $\alpha_2 = 1$ , the FH component; (d)  $\alpha_1 = 0.5$ ,  $\alpha_2 = 1$ , the SH component. The bifurcation diagram for the corresponding symmetric coupler is also included as a reference (by the dotted lines).

#### 4.4.2.3 Stability of the Solitons and Dynamical Rearrangement of Unstable Solitons

In Figs. 4.7 - 4.9, the solution branches which are expected to be unstable on the basis of the general principles of the bifurcation theory [86] are shown by the dot-

dashed lines. The corresponding stability results are natural extensions of those obtained in the previous chapters for the symmetric coupler. To verify this, direct BPM simulations were run at a number of points in the parametric space. It has been found that the solutions which were expected to be stable or unstable on the basis of the general principles, always agree with the predictions. It has also been found that nonlinear development of the instability of unstable soliton states tends to rearrange the unstable solitons into the stable ones existing at the same values of the parameters. As an example, in Fig. 4.10 we show the evolution (solid lines) of an unstable soliton (corresponding to the point A in Fig. 4.9a), with a visible trend to rearrange it into its stable counterpart (corresponding to the point B in Fig. 4.9a), for the case  $K = 0$  (the widely separated cores). In Fig. 4.10, we have also showed the evolution (dotted lines) of the same soliton input into another stable soliton (corresponding to the point C in Fig. 4.9a) when the asymmetry of the coupler is nullified; i.e.,  $\alpha_1 = \alpha_2 = 1$ . This demonstrates the potential use of the proposed  $\chi^{(2)}$  coupler as an optical switching device, provided that the asymmetry of the coupler may be controlled electronically (e.g., by means of the piezoelectric effect). Finally, we note that conspicuous internal vibrations observed during the evolution are characteristic of  $\chi^{(2)}$  systems [59].

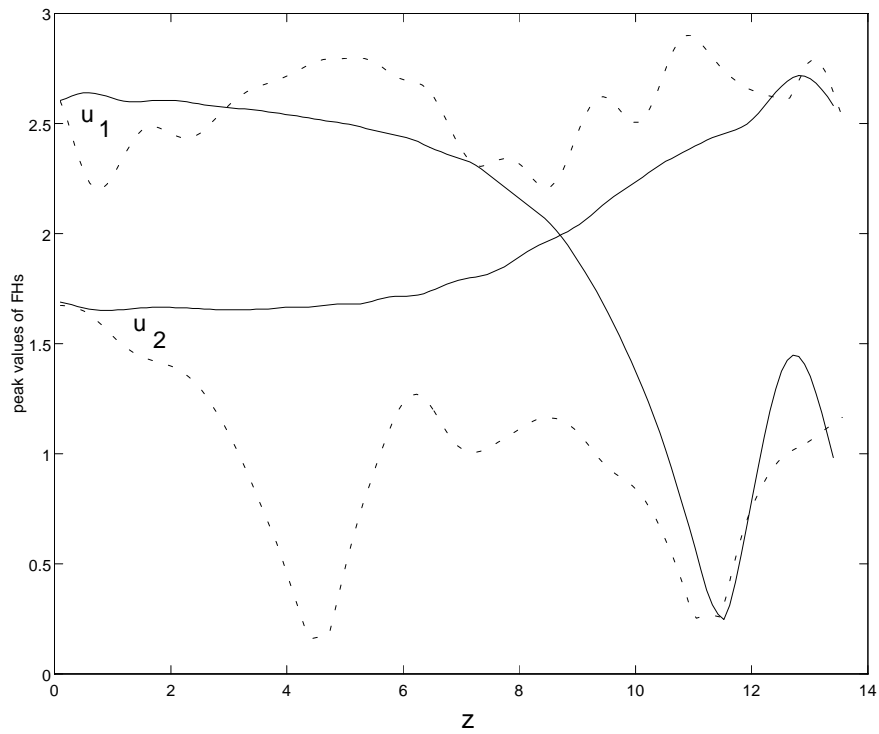


Figure 4.10: The evolution of soliton states

Solid lines: the evolution of an unstable soliton state into the corresponding stable soliton, for widely separated cores (the case  $K = 0$ ), with  $\alpha_1 = 2$ ,  $\alpha_2 = 1$ , and  $Q = 0.25$ . Dotted lines: the evolution of the same soliton input when the asymmetry of the coupler is nullified; i.e.,  $\alpha_1 = \alpha_2 = 1$ . Only the evolution of the FH waves is shown here (the SH waves follow the same trend and are not shown).

### 4.4.3 Solitons in the Coupler with One Linear and One Non-linear Cores

The special case of the coupler in which one core is linear is of interest by itself (see results below which show that soliton-like localized wave with no effective diffraction can be present in a linear core) and for applications [77]. Recall that the corresponding model is obtained from the general system (4.6) - (4.9) by dropping the nonlinear terms in Eqs. (4.8) and (4.9). The results were obtained for the case of no phase mismatch, viz.,  $\alpha_1 = \alpha_2 = 1$ . It immediately follows from the linear equations (4.8) and (4.9) that, if also  $K = Q$  (the case of small separation between the cores), the FH and SH asymmetries are strictly equal,  $\Theta_F = \Theta_S$ . For this case, the results are summarized in Fig. 4.11, in the form of the plot of  $\Theta_F$  vs.  $Q$ . A noteworthy feature of the solution is that, as the linear coupling,  $|Q|$ , tends to the value 1, the solitons in both cores tend to become identical. (Note that the word “solitons” is used loosely here for the linear core to mean localized waves with no effective diffraction; rather than to refer to the definition that soliton is formed by a balance between diffraction and nonlinearity, which obviously is absent in the linear core.) Also, the numerical solutions demonstrate that the solitons can only be obtained when the nonlinear core dominates, which is quite natural, as the solitons cannot exist without the nonlinearity. When  $K = 0$  (the case of the widely separated cores), the solutions do not have any SH components in the linear core, i.e.,  $\Theta_S = 1$ . Otherwise, there is only a small qualitative difference between this case and the previous one,  $K = Q$ .

As concerns the stability, it has been found, by means of the direct BPM simulations, that *all* the soliton solutions for both cases  $K = Q$  and  $K = 0$  are stable.

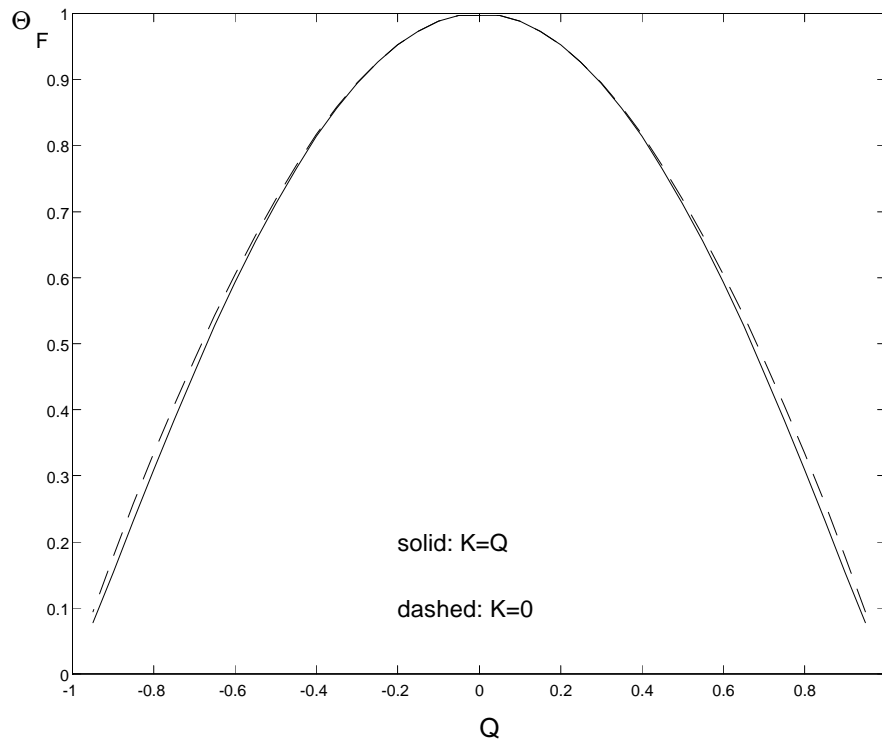


Figure 4.11: Plots of the asymmetric parameter,  $\Theta_F$ , vs. the linear coupling constant,  $Q$ ,

for the closely placed waveguides (the case  $K = Q$ ; the solid line), and for the widely separated waveguides (the case  $K = 0$ ; the dashed line). One waveguide is linear and the other one is quadratically nonlinear. In the case  $K = Q$ ,  $\Theta_F \equiv \Theta_S$ , and in the case  $K = 0$ ,  $\Theta_S = 1$ .

## 4.5 Conclusion

In this Chapter, we analyze, in detail, effects of a walkoff (spatial misalignment) between the two cores. We demonstrate that the asymmetric solitons remain stable if walkoff is small. When the walkoff becomes larger, the solitons get strongly distorted, and finally destructed when walkoff.

We also investigated effects when the phase mismatch parameter was varied. As the phase mismatch parameter,  $q$ , gets smaller than 1, the regions where the asymmetric solitons exist shrink, whereas these regions expand when  $q$  gets larger than 1. However, as  $q$  increases beyond about 4, the asymmetry stays more or less constant, especially for the case  $K = 0$ .

Then, by means of direct numerical methods, we study spatial solitons and their stability in a pair of asymmetric linearly coupled waveguides with the intrinsic quadratic nonlinearity. Two cases are considered in detail, viz., when the coupling constants at the fundamental and second harmonics are equal, and when the coupling at the second harmonic is absent. These cases correspond to the physical situations in which the coupled waveguides are, respectively, closely or widely separated. Two different kinds of the asymmetry between the waveguides are considered. The first of them corresponds to a difference in the phase mismatch between the fundamental and second harmonics in the two cores. Unfoldings of the previously known bifurcation diagrams for the symmetric coupler are studied in detail at various values of the asymmetry parameter, and stability of different branches of the solutions are tested. Simulations of dynamical evolution of unstable solitons demonstrates a trend of their rearrangement into stable solitons coexisting with them. The second kind of the asymmetry is the special case when one waveguide is linear, while

the other one possesses the quadratic nonlinearity. In contrast to the case when both waveguides are nonlinear, in this case the soliton solutions for the two limiting cases of the closely and widely separated waveguides are not much different. All the solitons in this system are found to be stable. The obtained results, and especially bifurcations between solitons of different types, suggest straightforward applications to the all-optical switching. For example, the numerical experiment as depicted in Fig. (4.10) indicates the use of that device as an electronically controlled demultiplexer.

# Chapter 5

## Coupled Waveguides with Bragg Gratings

### 5.1 Introduction

A soliton is a localized pulse of wave, which gains its stability by a balance of the effect of the nonlinearity of the medium, which tends to concentrate the energy of the pulse and the effect of group velocity dispersion (for temporal soliton), or normal diffraction (for spatial soliton), which tends to disperse the energy of the pulse. Gap solitons are also localized wave structure, but in a medium which has a periodic variation in the linear optical properties, i.e., with a grating, over a length scale on the order of the wavelength of light. The balance will then be between the nonlinearity and the effective dispersion (or diffraction) due to the photonic band gap structure that results from the periodic variation in the linear dielectric constant. Qualitatively, the grating dispersion is due to the fact that, close to the Bragg resonance, light is slowed down because of the multiple Fresnel reflections off

the rulings of the grating. This slowdown of the group velocity of light, however, has a strong frequency dependence, leading to the strong dispersion. A recent experimental study [87] has demonstrated that the effective Bragg-grating dispersion may be *six orders* of magnitude larger than that in uniform fiber. A detailed account of the interplay between the counterpropagation of forward and backward waves, and the resulting opening up of a gap in the system's linear spectrum (the photonic bandgap) can be found in [88, 89].

Since the grating structure can easily be engineered, also the effective dispersion (diffraction) due to the grating is always much stronger than the normal material dispersion (diffraction) [75], medium with a grating structure offers ideal premises to generate solitons, with properties which are easily controlled by proper design of the grating structure. Since the soliton period is inversely proportional to the dispersion, the strong dispersion implies gap solitons can be observed in gratings of only a few centimeters in length; however, the strong dispersion also implies that the required optical intensities to generate solitons are correspondingly higher than in uniform media. This is because the effect of the nonlinearity needed to balance the dispersion must be much larger, but the strength of the nonlinearity is unaffected by the grating.

Early investigations of nonlinear periodic structures included the studies of the stationary properties and dynamics of fields in such structures [90, 91]. The term "gap soliton" was first used by Chen and Mills [92], who showed that electric field in such periodic structure can exhibit solitonic behaviour, using numerical techniques. Further discussion of the implications of modulation instability in nonlinear periodic structures for the existence of gap soliton can be found in [93]. In subsequent researches, it was shown that wave envelope functions in nonlinear periodic

structures do really have analytical solitary-wave solutions [71, 72, 94], following the pattern of the classical exact soliton solution to the massive Thirring model (MTM) [95, 96] (this approach is referred to below as the MTM approach). The solutions have two parameters: the first one determines the soliton's velocity, which can be anywhere between zero and the speed of light in the bare medium, while the second one is a detuning parameter which determines the width, height, and spectrum of the soliton. In another limit, where the nonlinear terms can be treated as small perturbations, linear approximation can be assumed to represent the solutions by Bloch functions (BF), which are the eigenfunctions of the periodic linear media [88]. By applying perturbation method to take the nonlinearity as slow modulations of the Bloch functions, the wave envelope function can be shown to satisfy the nonlinear Schrödinger equation [97]-[99]. The solution is then well known [100]. We refer to this approach as the BF approach below. In [101]-[103], they used the name "Bragg Grating Solitons" for the gap soliton solutions, where such an approach is applicable, which have the spectral contents concentrated close to the edge of the photonic band gap. A detailed comparison of the two approaches can be found in [89].

Many structures can be used for the experimental observation of gap solitons. These include thin-film stacks, planar waveguides with a surface corrugation, and optical fibers with a grating grown or written in them. Among these, optical fiber is the most attractive because its low loss allows very long interaction lengths, which thus reduce the nonlinearity required. A recent experimental achievement was the observation of Bragg grating solitons in optical fiber with gratings written on it, using the phase mask scanning technique [87, 104]. Earlier observation of gap soliton propagation in optical fiber gratings was reported in [105].

On the other hand, research efforts also diverted into investigation of gap solitons in a nonlinear optical systems with other nonlinearities. Recently, theoretical results have been reported for the model with the quadratic (second-harmonic-generation) nonlinearity [106]-[111], as well as for the self-induced transparency in the extended Bragg reflector (resonant interaction between the counterpropagating waves and two-level atoms) [112].

However, in these earlier works, gap solitons were investigated in a *single* waveguide. In this work, we study gap solitons in a system of two linearly coupled waveguides with Bragg gratings, which have never been studied before. The system which we study here may find a broad field of applications, as it combines properties of the solitons in both the dual-core nonlinear fibers and in the nonlinear single-core ones with the Bragg gratings.

## 5.2 Background Theory

To give a qualitative description of the background physics of gap solitons propagating through periodic structures, let us consider a grating in an optical fiber, which points in, says, the  $z$ -direction. The refractive index profile is as shown in Fig. 5.1. For simplicity (also in practice), we can assume the modulation amplitude  $\Delta n$  of the refractive index to be small, or  $\Delta n \ll \bar{n}$ ,  $\bar{n}$  being the average refractive index. This means that the grating is shallow. The period of the periodic refractive index modulation is  $d$ . The key property of gratings is that at wavelength  $\lambda \sim \lambda_o$ , where

$$\lambda_o = 2\bar{n}d, \quad (5.1)$$

exactly half a wavelength fits into each period of the grating. At this “Bragg condition”, light which is reflected off the interfaces which are an integer number of

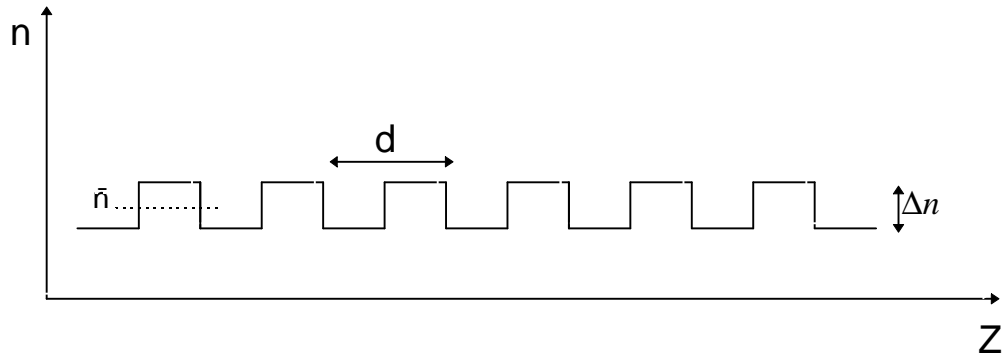


Figure 5.1: The refractive index profile of a Bragg grating structure.

periods apart are all in phase. The reflected wave will then be very strong, and for a grating of sufficient length, the reflectivity can be almost one. Higher-order Bragg reflection also can occur at shorter wavelengths. At wavelengths far from this Bragg condition, the light reflected off the various interfaces is mutually out of phase. As a consequence, the light then propagates through the medium essentially with transmissivity close to unity.

Rather than as a function of wavelength, Eq. (5.1) can be re-written as a function of the frequency  $\omega$ ,

$$\omega_o = \frac{\pi c_o}{\bar{n}d}, \quad (5.2)$$

where  $\omega_o$  is the Bragg frequency, and  $c_o$  is the speed of light in vacuum.

We also define here the wave number  $k_o$  at the Bragg condition,

$$k_o \equiv \frac{\pi}{d}. \quad (5.3)$$

The range of frequencies  $\Delta\omega$  around  $\omega_o$ , over which light is Bragg-reflected is

given by [89]:

$$\frac{\Delta\omega}{\omega_o} \sim \frac{\Delta n}{\bar{n}}. \quad (5.4)$$

Let us denote the upper edge of this frequency range by  $\omega_u$ , and the lower edge by  $\omega_l$ . We consider the nonlinearity to be of Kerr (cubic) type; i.e., the refractive index is intensity-dependent,

$$n(I) = n_1 + n_2 I. \quad (5.5)$$

$I$  is the local light intensity,  $n_1$  is the linear refractive index, and  $n_2$  is the nonlinear index coefficient. For simplicity, we take the nonlinearity to be positive, so that the refractive index increases with intensity. From Eq. (5.2), it can be seen that the Bragg frequency  $\omega_o$  will decrease with intensity  $I$ . So, light with high intensity at frequency around  $\omega_u$  will detune itself from the Bragg condition, and can propagate through the medium unimpeded, while light with low intensity at the same frequency will be Bragg-reflected. Now, let us consider a light pulse with frequency  $\omega_u$ , present in the nonlinear periodic medium. It can be seen that light in the middle of the pulse with high intensity can propagate freely in the medium, while light at the leading and trailing skirts of the pulse, where intensity is low, will be Bragg-reflected back towards the middle of the pulse. From this simple qualitative description, it can be deduced that once a high intensity light pulse is created inside such nonlinear periodic medium, it tends to stay together, and travels through the medium as a soliton.

## 5.3 Coupled-Mode Equations for a Single Nonlinear Waveguide

For a single nonlinear waveguide with a grating in it, let us consider the light wave to travel in the  $z$ -direction. As usual, we can assume that the medium is non-magnetic, and the light is linearly polarized. We can start the derivation of the modelling equations from Eq. (1.23) in Chapter 1, which I write again here as,

$$\nabla \times \nabla \times E = \frac{1}{c_0^2} \frac{\partial^2}{\partial \tau^2} E - \mu_o \frac{\partial^2}{\partial \tau^2} P \quad (5.6)$$

(Note that the symbol  $\tau$  is used instead here to denote the “time” variable, reserving  $t$  for the normalized time later.) Following the same assumptions leading to Eq. (1.34), Eq. (5.6) becomes

$$\frac{\partial^2}{\partial z^2} E - \frac{\epsilon(z)}{c_0^2} \frac{\partial^2}{\partial \tau^2} E - \mu_o \frac{\partial^2}{\partial \tau^2} P^{NL} = 0. \quad (5.7)$$

Since what we consider here is temporal soliton, as contrast to spatial soliton considered in Section (1.4.1), the second derivative terms with respect to the transverse coordinates  $x$ , and  $y$  are absent here. Also, in Section (1.4.1), the dielectric constant  $\epsilon \equiv (1 + \chi)$  was a function of  $y$  only to account for the refractive index profile of the slab waveguide. Here, for a waveguide with a grating, the dielectric constant will then be a function of  $z$  to model the periodic variation due to the grating. Specifically, we write

$$\epsilon(z) = \bar{n}^2 + \varepsilon(z), \quad (5.8)$$

where we consider  $\varepsilon(z)$  to have a period of  $d$ , i.e., period of the grating. Expanding  $\varepsilon$  in a Fourier series, we have

$$\varepsilon(z) = \sum_m \varepsilon_m \exp(2ik_o m z). \quad (5.9)$$

Since the average value of the dielectric constant has been denoted explicitly as  $\bar{n}^2$ ,  $m = 0$  is excluded from the summation. We will restrict ourselves to consider only light at frequencies  $\omega$  around the Bragg condition at  $\omega_o$ , cf. Eq. (5.2).

We look for solutions of the form:

$$E(z, \tau) = E_+(z, \tau)e^{i(\omega_o\tau - k_o z)} + E_-(z, \tau)e^{i(\omega_o\tau + k_o z)} + c.c., \quad (5.10)$$

where  $E_+$  and  $E_-$  denote the fields travelling to the right (forward direction) and left (backward direction), and they vary weakly with  $z$  and  $\tau$ . c.c. stands for complex conjugates.

We then insert Eq. (5.8),(5.9)&(5.10) into Eq. (5.7). Note that in taking second derivatives, those terms involving  $k_o^2 E_{\pm}$  and  $\omega_o^2 E_{\pm}$  will cancel because of the linear dispersion relation. Those terms involving  $\partial^2 E_{\pm}/\partial z^2$ , and  $\partial^2 E_{\pm}/\partial \tau^2$  can be neglected because we assume  $E_+$  and  $E_-$  to be slowly varying. Also, The contribution from the nonlinear polarization is assumed to be of the same order as the second derivatives of the linear terms, so that only the lowest order terms due to the nonlinearity are kept. This is justifiable, since this is the physical requirement of a balance between nonlinearity and dispersion for obtaining soliton solutions (see, e.g., discussion in [8]). Thus, we get

$$\begin{aligned} & \left[ +i\frac{\partial E_+}{\partial z} + i\frac{\bar{n}}{c_0}\frac{\partial E_+}{\partial \tau} + \kappa E_- + s|E_+|^2 E_+ + 2\chi|E_-|^2 E_+ \right] e^{i(\omega_o\tau - k_o z)} \\ & + \left[ i\frac{\partial E_-}{\partial z} + i\frac{\bar{n}}{c_0}\frac{\partial E_-}{\partial \tau} + \kappa E_+ + s|E_-|^2 E_- + 2\chi|E_+|^2 E_- \right] e^{i(\omega_o\tau + k_o z)} \\ & + c.c. = 0, \end{aligned} \quad (5.11)$$

where  $s$  and  $\chi$  are given by [8, 10, 113, 114]:

$$s = \frac{3}{4} \frac{\omega_o^2}{k_o c_0^2} Q_{eff}^S \chi^{(3)}(\omega; \omega, -\omega, \omega) \quad (5.12)$$

and

$$\chi = \frac{3}{4} \frac{\omega_o^2}{k_o c_0^2} Q_{eff}^\times \chi^{(3)}(\omega; \omega, \omega, \omega). \quad (5.13)$$

$Q_{eff}^S$  and  $Q_{eff}^\times$  are the effective modal overlap integrals for self-phase modulation and cross-phase modulation respectively, cf. Eq. (1.42). Usually, these two integrals are the same. We label them separately because, in some mode-coupling problems, the mode overlap is more complicated, and they can be different. Finally, we have

$$\begin{aligned} +i \frac{\partial E_+}{\partial z} + i \frac{\bar{n}}{c_0} \frac{\partial E_+}{\partial \tau} + \kappa E_- + s |E_+|^2 E_+ + 2 \chi |E_-|^2 E_+ &= 0 \\ i \frac{\partial E_-}{\partial z} + i \frac{\bar{n}}{c_0} \frac{\partial E_-}{\partial \tau} + \kappa E_+ + s |E_-|^2 E_- + 2 \chi |E_+|^2 E_- &= 0. \end{aligned} \quad (5.14)$$

where

$$\kappa = \frac{\omega_o \tilde{\epsilon}}{2 \bar{n} c_0}, \quad (5.15)$$

and  $\tilde{\epsilon} \equiv \epsilon_1 - \epsilon_{-1}$ .

Note that all the non-phase-matched terms and terms involving components of higher spatial frequencies in Eq. (5.9) have been ignored, keeping only the lowest order Fourier terms  $\epsilon_1$  and  $\epsilon_{-1}$ . This is acceptable because, if the grating is shallow, i.e.,  $\epsilon_m / \bar{n}^2$  being small, all the higher terms will be of order  $\kappa^2$  and negligible, cf. Eq.(5.15).

Note that the  $\kappa E_\pm$  terms in Eq. (5.14) represent the linear couplings between the forward moving and the backward moving waves due to the grating. From Eq. (5.15), it can be seen that the coupling strength depends on the Bragg frequency, and the fractional refractive index modulation depth.

These coupled-mode equations are for a single waveguide with grating. We will re-visit these equation in Section (5.5), where we will add in the coupling terms due to tunnel-coupling between two parallel closely spaced waveguides.

## 5.4 Scope of Investigation

In this Chapter, the discussion will be on the investigation of solitons (strictly speaking, solitary waves, SW's) in a model of two linearly coupled waveguides with the Kerr nonlinearity and resonant gratings in both of them, i.e., a hybrid of the well-known nonlinear optical coupler [15, 115] with the Bragg grating. This chapter differs from the previous ones in that all previous chapters deal with waveguides with quadratic nonlinearity. However, the treatment of coupled waveguides with Bragg gratings and *quadratic* nonlinearity will need a model of totally eight equations, which is much more involved. Since coupled waveguides with the Kerr nonlinearity and resonant gratings have not been studied before, such a study will give new and useful informations on the interplay of Bragg reflection and linear tunnel coupling between cores. The linear couplings between the forward and backward Bragg-scattered waves will induce an effective dispersion, which, similar to the single waveguide case, is much stronger than the intrinsic material dispersion. The material dispersion can thus be neglected.

In such a system, we will show that a bifurcation occurs which transforms the obvious symmetric solitons into nontrivial asymmetric ones for quiescent (standing) solitons. This resembles the well-known bifurcation in the dual-core nonlinear optical fiber (without the gratings but with the material dispersion taken into regard), see [17, 20, 23]. The solutions are found by the same approach as in earlier chapters, first in an approximate analytical form by means of the variational approximation and, then independently, by direct finite-difference numerical simulations. We further establish the stability of the asymmetric solitons by direct simulations, while showing that the symmetric solitons coexisting with the asymmetric ones are al-

ways unstable, using the BPM. Symmetric solitons are stable only if there is no co-existing asymmetric ones.

Next, we consider travelling SW's. In order to display the results, we fix the frequency detuning, while the strength of the coupling between the two cores and the velocity of the moving soliton are varied. In this case, the solutions are found only by direct numerical methods, revealing that moving asymmetric solitons exist and are stable. Similar to the case of the quiescent SW's, the symmetric solitons coexisting with the asymmetric ones prove to be always unstable.

## 5.5 The Mathematical Techniques

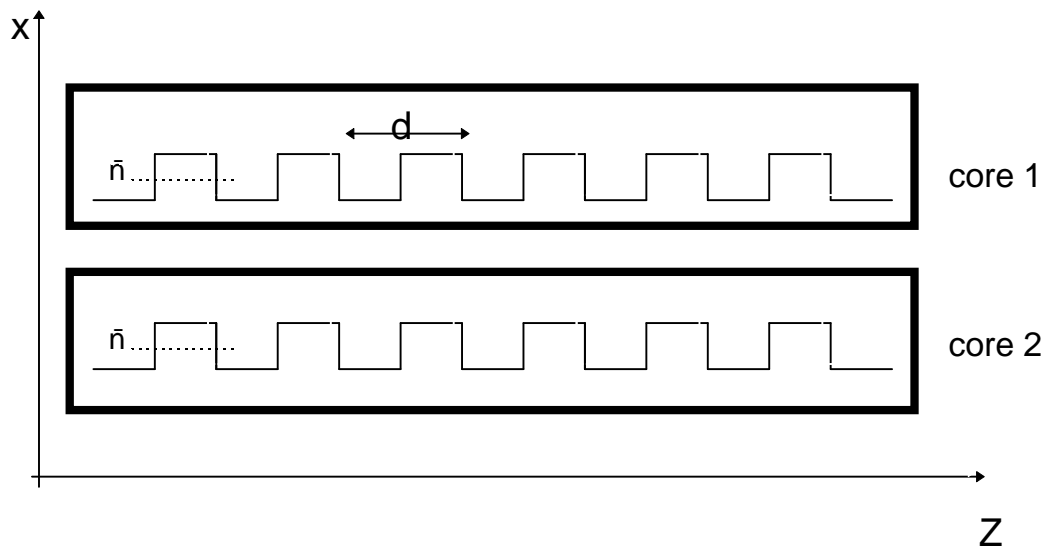


Figure 5.2: Schematic diagram of one implementation of the model using nonlinear dual-core fibres with gratings.

In Fig. 5.2, we show a schematic diagram of the most straightforward implementation of the model introduced in this work, using dual-core nonlinear fibres with

gratings.

The electric fields  $E$  in two coupled nonlinear waveguides with the Bragg gratings are looked for in the form (cf. Eq. (5.10)):

$$\begin{aligned} E_1(z, \tau) &= \mathcal{E}_{1+}(z, \tau)e^{i(\omega_0\tau - k_0z)} + \mathcal{E}_1(z, \tau)e^{i(\omega_0\tau + k_0z)} + \text{c.c.}, \\ E_2(z, \tau) &= \mathcal{E}_{2+}(z, \tau)e^{i(\omega_0\tau - k_0z)} + \mathcal{E}_2(z, \tau)e^{i(\omega_0\tau + k_0z)} + \text{c.c.} \end{aligned} \quad (5.16)$$

Here, the subscript 1 and 2 pertain to the two cores. The  $\mathcal{E}_{1\pm}$  and  $\mathcal{E}_{2\pm}$  are slowly varying envelope functions.

Starting from the Maxwell equations, following the same approach as in Section 5.3, the following evolution equations for the field envelopes can be derived, cf. Eq. (5.14), (see also [89, 116, 11]):

$$\begin{aligned} +i\frac{\partial\mathcal{E}_{1+}}{\partial z} + i\frac{\bar{n}}{c_0}\frac{\partial\mathcal{E}_{1+}}{\partial\tau} + \kappa\mathcal{E}_1 + |\mathcal{E}_{1+}|^2\mathcal{E}_{1+} + 2|\mathcal{E}_1|^2\mathcal{E}_{1+} + K\mathcal{E}_{2+} &= 0 \\ i\frac{\partial\mathcal{E}_1}{\partial z} + i\frac{\bar{n}}{c_0}\frac{\partial\mathcal{E}_1}{\partial\tau} + \kappa\mathcal{E}_{1+} + |\mathcal{E}_1|^2\mathcal{E}_1 + 2|\mathcal{E}_{1+}|^2\mathcal{E}_1 + K\mathcal{E}_2 &= 0 \\ +i\frac{\partial\mathcal{E}_{2+}}{\partial z} + i\frac{\bar{n}}{c_0}\frac{\partial\mathcal{E}_{2+}}{\partial\tau} + \kappa\mathcal{E}_2 + |\mathcal{E}_{2+}|^2\mathcal{E}_{2+} + 2|\mathcal{E}_2|^2\mathcal{E}_{2+} + K\mathcal{E}_{1+} &= 0 \\ i\frac{\partial\mathcal{E}_2}{\partial z} + i\frac{\bar{n}}{c_0}\frac{\partial\mathcal{E}_2}{\partial\tau} + \kappa\mathcal{E}_{2+} + |\mathcal{E}_2|^2\mathcal{E}_2 + 2|\mathcal{E}_{2+}|^2\mathcal{E}_2 + K\mathcal{E}_1 &= 0 \end{aligned} \quad (5.17)$$

The only difference of Eq. (5.17) from Eq. (5.14) is the linear tunnel-coupling terms (the sixth terms) between waves in the two separate cores. Since tunnel-coupling is independent of the presence of the gratings, the derivation of these terms is no difference from that in Chap. 2 (see discussion there).

The third terms in the equations account for the linear conversion induced by the Bragg scattering in each core, the fourth and the fifth terms correspond to the self-phase modulation and cross-phase modulation, respectively. Note that we assume  $s = \times \equiv \cdot$ .

We then apply the following rescaling to Eqs.(5.17),

$$\mathcal{E}_{1,2+} \equiv \sqrt{\frac{\kappa}{2}}U_{1,2}, \quad \mathcal{E}_{1,2} \equiv \sqrt{\frac{\kappa}{2}}V_{1,2}, \quad (5.18)$$

$$z \equiv \frac{x}{\kappa}, \quad \tau \equiv \frac{\bar{n}}{\kappa c_0}t, \quad (5.19)$$

arriving at the set of the normalized equations which describe the wave propagation in the linearly coupled nonlinear cores with the gratings:

$$iU_{1t} + iU_{1x} + (\sigma|U_1|^2 + |V_1|^2)U_1 + V_1 + \lambda U_2 = 0, \quad (5.20)$$

$$iV_{1t} - iV_{1x} + (\sigma|V_1|^2 + |U_1|^2)V_1 + U_1 + \lambda V_2 = 0, \quad (5.21)$$

$$iU_{2t} + iU_{2x} + (\sigma|U_2|^2 + |V_2|^2)U_2 + V_2 + \lambda U_1 = 0, \quad (5.22)$$

$$iV_{2t} - iV_{2x} + (\sigma|V_2|^2 + |U_2|^2)V_2 + U_2 + \lambda V_1 = 0. \quad (5.23)$$

If the model is realized in terms of the parallel-coupled optical fibers equipped with gratings,  $t$  and  $x$  are the normalized time and propagation distance, respectively. Alternatively, the same model can be realized as describing stationary field distributions in two parallel-coupled planar waveguides with the gratings in the form of a system of parallel scores (stratified layers), in which case  $t$  and  $x$  are, respectively, the normalized propagation distance and the normalized transverse coordinate. In the case of the optical fibers, which is the most realistic realization of the model [101, 104], we neglect the fiber's intrinsic dispersion, while in the case of the planar waveguides, the diffraction is neglected. The coefficient  $\sigma$  accounts for the self-phase modulation to cross-phase modulation coefficient being set equal to 1. In the single-core case, the model with  $\sigma = 0$  is equivalent to MTM [95]. However, in the application to the optical media  $\sigma = \frac{1}{2}$  (as we have already assumed in Eqs.(5.17)). Lastly, the above rescaling yields the coefficient in front of the last linear coupling terms in Eqs. (5.20)–(5.23):  $\lambda = K/\kappa$ .

To find stationary solutions, we search for them in the form

$$U_{1,2} = e^{-i\omega t} u_{1,2}(\xi), \quad V_{1,2} = e^{-i\omega t} v_{1,2}(\xi), \quad (5.24)$$

where  $\xi \equiv x - ct$  is the coordinate in the reference frame moving with the soliton's velocity  $c$  (according to Eqs. (5.19),  $c$  is normalized with respect to the speed of light  $c_0/\bar{n}$  in the dielectric medium), and  $\omega$  is a frequency detuning. Referring to the scaling equations (5.19), it can be noted that the limiting frequency detuning values  $\omega = \pm 1$  correspond to the centre frequency of the soliton being at the edges of the photonic band gap (cf. section 3 of [89]).

Substituting Eqs. (5.24) into Eqs. (5.20)–(5.23) leads to the coupled ODE's (with the prime standing for  $d/d\xi$ ),

$$\omega u_1 + i(1 - c)u_1' + (\sigma|u_1|^2 + |v_1|^2)u_1 + v_1 + \lambda u_2 = 0, \quad (5.25)$$

$$\omega v_1 - i(1 + c)v_1' + (\sigma|v_1|^2 + |u_1|^2)v_1 + u_1 + \lambda v_2 = 0, \quad (5.26)$$

$$\omega u_2 + i(1 - c)u_2' + (\sigma|u_2|^2 + |v_2|^2)u_2 + v_2 + \lambda u_1 = 0, \quad (5.27)$$

$$\omega v_2 - i(1 + c)v_2' + (\sigma|v_2|^2 + |u_2|^2)v_2 + u_2 + \lambda v_1 = 0. \quad (5.28)$$

As a first step, we study quiescent solitons with  $c = 0$ , so that  $\xi \equiv x$ . On the other hand, to set up a standing-wave solution, the forward and backward propagating waves,  $u_{1,2}$  and  $v_{1,2}$ , must bear certain symmetry relations. The relations compatible with the underlying equations and with the exact solutions found in [71] are

$$v_{1,2} = -u_{1,2}^*. \quad (5.29)$$

Substituting Eqs. (5.29) into Eqs. (5.25)–(5.28) (with  $c = 0$ ), we arrive at a simplified system,

$$\omega u_1 + iu_1' + (\sigma + 1)|u_1|^2 u_1 - u_1^* + \lambda u_2 = 0, \quad (5.30)$$

$$\omega u_2 + iu_2' + (\sigma + 1)|u_2|^2 u_2 - u_2^* + \lambda u_1 = 0. \quad (5.31)$$

To find nontrivial (asymmetric) soliton solutions to Eqs. (5.30) and (5.31), two independent methods were employed. An analytical approach is based on the variational approximation (VA), i.e., the same method as used in previous chapters.

However, there is a novel technical feature in the present problem: thus far, VA was usually applied to find real solutions, while here we are seeking for essentially *complex* ones (an exception is the work [70], in which VA was elaborated for solitons in the generalized MTM introduced in [71, 72] to describe an optical fiber with the Bragg grating and cubic nonlinearity). This difference is not simply formal: the necessity to accommodate a complex waveform makes the corresponding *ansatz* (the trial soliton's form) much more involved, and in many cases a straightforward extension of the usual VA leads to messy equations of no practical value. However, below we will develop an analytical approximation that will produce very reasonable results for the present model.

To apply VA, we need the Lagrangian density for Eqs. (5.30) and (5.31), which is

$$\begin{aligned} \mathcal{L} = & \omega(u_1 u_1^* + u_2 u_2^*) + \frac{i}{2}(u_{1x} u_1^* - u_{1x}^* u_1) + \frac{i}{2}(u_{2x} u_2^* - u_{2x}^* u_2) \\ & + \frac{1}{2}(\sigma + 1)(|u_1|^4 + |u_2|^4) - \frac{1}{2}(u_1^2 + u_1^{*2} + u_2^2 + u_2^{*2}) \\ & + \lambda(u_1 u_2^* + u_1^* u_2). \end{aligned} \quad (5.32)$$

Then, the following *ansatz* is adopted for the quiescent solitons sought for:

$$u_1 = A_1 \operatorname{sech}(\mu x) + iB_1 \sinh(\mu x) \operatorname{sech}^2(\mu x), \quad (5.33)$$

$$u_2 = A_2 \operatorname{sech}(\mu x) + iB_2 \sinh(\mu x) \operatorname{sech}^2(\mu x), \quad (5.34)$$

where the amplitudes  $A_{1,2}$  and  $B_{1,2}$  are real. Inserting Eqs. (5.33)–(5.34) into Eq. (5.32), it is straightforward to calculate the *effective Lagrangian*:

$$\begin{aligned}
 L \equiv \int_{-\infty}^{+\infty} \mathcal{L} dx &= \frac{2\omega}{\mu}(A_1^2 + A_2^2) + \frac{2}{3\mu}\omega(B_1^2 + B_2^2) - \frac{4}{3}(A_1B_1 + A_2B_2) \\
 &+ \frac{2(\sigma+1)}{3\mu}(A_1^4 + A_2^4) - 0.8571\frac{\sigma+1}{\mu}(B_1^4 + B_2^4) \\
 &+ \frac{4(\sigma+1)}{15\mu}(A_1^2B_1^2 + A_2^2B_2^2) - \frac{2}{\mu}(A_1^2 + A_2^2) + \frac{2}{3\mu}(B_1^2 + B_2^2) \\
 &+ \frac{4\lambda}{\mu}A_1A_2 + \frac{4\lambda}{3\mu}B_1B_2
 \end{aligned} \tag{5.35}$$

(the numerical coefficient 0.8571 is given by some integral).

The variational equations are obtained by demanding the variations of the Lagrangian with respect to each of  $A_{1,2}$ ,  $B_{1,2}$ , and  $\mu$  to be zero. Thus, we obtain the following five equations:

$$\lambda A_2 - A_1 + \frac{2}{3}(\sigma+1)A_1^3 + \frac{2}{15}(\sigma+1)A_1B_1^2 - \frac{1}{3}\mu B_1 + \omega A_1 = 0, \tag{5.36}$$

$$\lambda A_1 - A_2 + \frac{2}{3}(\sigma+1)A_2^3 + \frac{2}{15}(\sigma+1)A_2B_2^2 - \frac{1}{3}\mu B_2 + \omega A_2 = 0, \tag{5.37}$$

$$\frac{1}{3}\lambda B_2 + \frac{1}{3}B_1 - 0.8571(\sigma+1)B_1^3 + \frac{2}{15}(\sigma+1)A_1^2B_1 - \frac{1}{3}\mu A_1 + \frac{1}{3}\omega B_1 = 0, \tag{5.38}$$

$$\frac{1}{3}\lambda B_1 + \frac{1}{3}B_2 - 0.8571(\sigma+1)B_2^3 + \frac{2}{15}(\sigma+1)A_2^2B_2 - \frac{1}{3}\mu A_2 + \frac{1}{3}\omega B_2 = 0, \tag{5.39}$$

$$\begin{aligned}
 &2\omega(A_1^2 + A_2^2) + \frac{2\omega}{3}(B_1^2 + B_2^2) + \frac{2(\sigma+1)}{3}(A_1^4 + A_2^4) - 0.8571(\sigma+1)(B_1^4 + B_2^4) \\
 &+ \frac{4(\sigma+1)}{15}(A_1^2B_1^2 + A_2^2B_2^2) - 2(A_1^2 + A_2^2) + \frac{2}{3}(B_1^2 + B_2^2) + 4\lambda A_1A_2 + \frac{4\lambda}{3}B_1B_2 = 0.
 \end{aligned} \tag{5.40}$$

We will then use the numerical Newton-Raphson method (see Section (3.3.2)) to solve these algebraic equations.

The other method, as in previous chapters, employs the direct numerical finite-difference solution of the equations, using the approximate solutions furnished by VA as the necessary first guess. Proceeding to finding the stationary solutions to

Eqs. (5.30)–(5.31) numerically, we will split the complex equations (5.30) and (5.31) into four equations for the real and imaginary parts of  $u_{1,2}$ . Straightforward finite-difference numerical techniques can then be applied to solve these real equations. For the travelling SW's, the symmetry relations (5.29) no longer apply. In this case, we split the full system of Eqs. (5.25)–(5.28) into eight equations for the real and imaginary parts of  $u_{1,2}$  and  $v_{1,2}$ , to which the same numerical techniques apply.

Finally, the stability of the soliton solutions is tested by direct simulations of the underlying PDE's (5.20)–(5.23). To this end, we again use the well-known split-step Fourier method, taking the initial configuration in the form of the soliton with a superimposed small perturbation.

## 5.6 Stationary Solutions

### 5.6.1 Quiescent Solitons

Quiescent soliton solutions are standing-wave solutions when the fields travelling in the forward direction,  $U_{1,2}$ , and in the backward direction,  $V_{1,2}$  (cf. Eqs. (5.20)–(5.23)) balance.

The first, quite obvious, result of our analysis is that, for any fixed value of the frequency detuning  $\omega$ , the symmetric soliton solutions are unique and stable at sufficiently large values of the coupling constant  $\lambda$  (we will address the stability issue later.) However, below a critical value of  $\lambda$ , the symmetric solutions bifurcate, giving rise to three branches, one being the continuation of the original symmetric branch, which becomes unstable, while two others are nontrivial stable *asymmetric* solutions. Because the coupled cores considered in this work are symmetric (identical), the two

asymmetric branches are mirror images of each other. As  $\lambda$  goes smaller, the solution gets more asymmetric. At  $\lambda = 0$ , when Eqs. (5.30) and (5.31) become decoupled, the numerical solution matches the *exact* one for the single waveguide (found in [71]) in one core, while the other core is empty in this limit.

The bifurcation is found to be *supercritical* (which is also called a forward bifurcation), the critical value of  $\lambda$  at the bifurcation point decreasing with the increase of  $\omega$ . The full bifurcation diagram, including both the variational prediction and the direct numerical results, is shown, for  $\omega = 0.5$ , in Fig. 5.3, which is a plot of an effective asymmetry parameter

$$\Theta \equiv \left( u_{1m}^2 \quad u_{2m}^2 \right) / \left( u_{1m}^2 + u_{2m}^2 \right) \quad (5.41)$$

vs. the coupling constant  $\lambda$ , where  $u_{1,2m}$  are the amplitudes of the field  $u$  in the two cores (it can be easily shown, using obvious symmetries of Eqs. (5.25) - (5.28), that the bifurcation diagram for  $\lambda < 0$  is the mirror image of that for  $\lambda > 0$ ). As one sees, agreement between the analytical prediction and the numerical results is fairly good. A further comparison of the variational and numerical results is illustrated by Fig. 5.4, which shows the shapes of the real and imaginary parts of the larger of the two asymmetric soliton components in the two cores.

A complete three-dimensional bifurcation, i.e., a plot of  $\Theta$  vs. both  $\omega$  and  $\lambda$ , is shown in Fig. 5.5. For clarity, this bifurcation diagram was drawn using only the numerical results, its variational counterpart being quite close to it. The asymmetric branch can be seen to narrow down as  $\omega$  approaches the limit value 1.

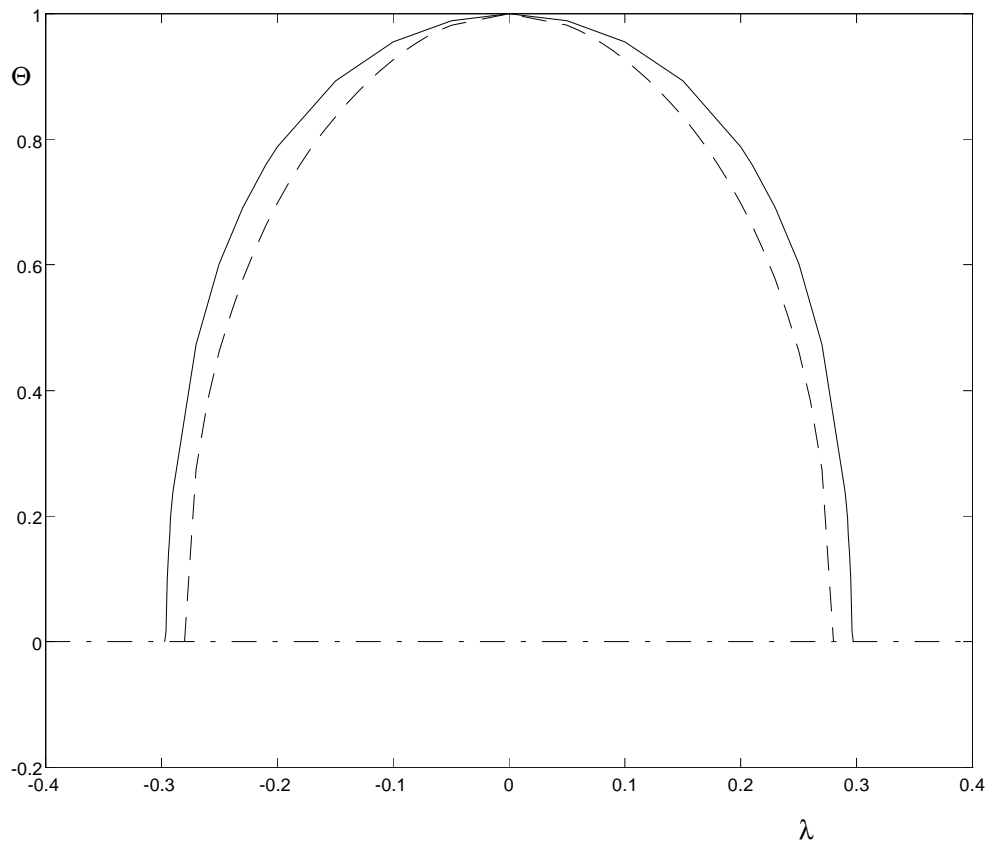


Figure 5.3: Bifurcation diagram for the quiescent soliton at  $\omega = 0.5$ . The solid and dashed line depict, respectively, the numerical results and the variational approximation. The dot-dashed line is the branch corresponding to the symmetric solutions. The branch at  $\Theta < 0$ , which is a mirror image of the curve shown, is not displayed here.

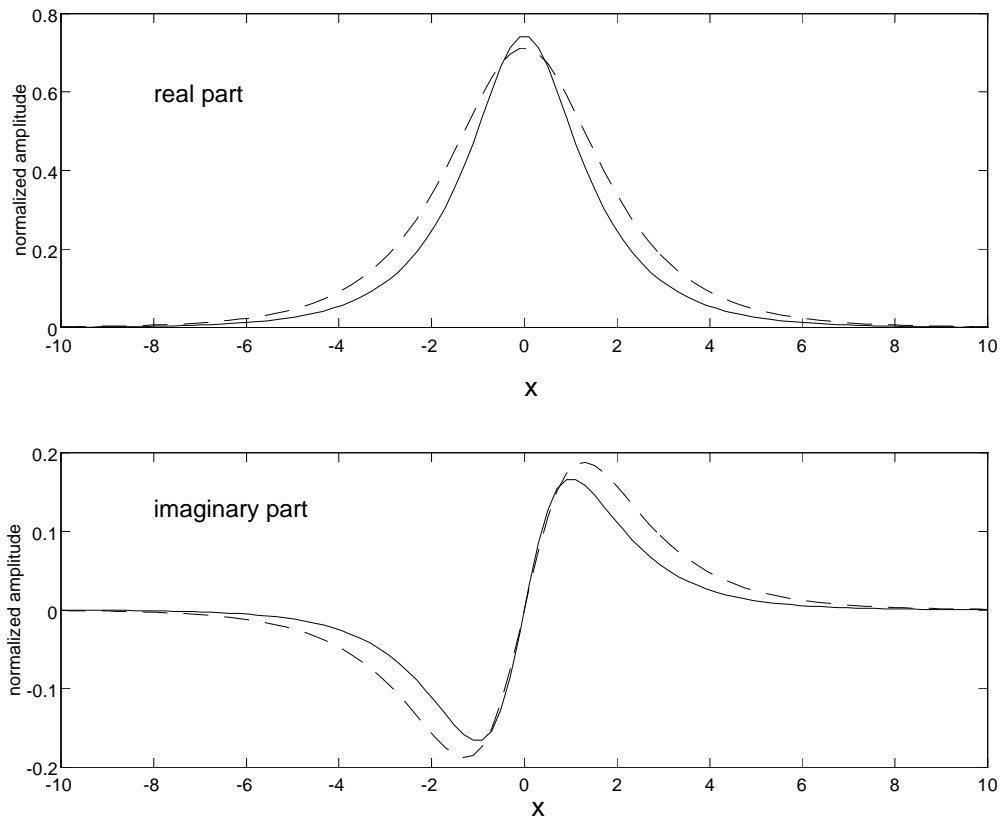


Figure 5.4: The shapes of the larger of the two quiescent-soliton components in the two cores. The upper and lower graphs show the real and imaginary parts of the forward-propagating wave. As in Fig. 5.3, the solid and dashed lines represent the numerical and variational results. Here,  $\omega = 0.5$  and  $\lambda = 0.2$ .

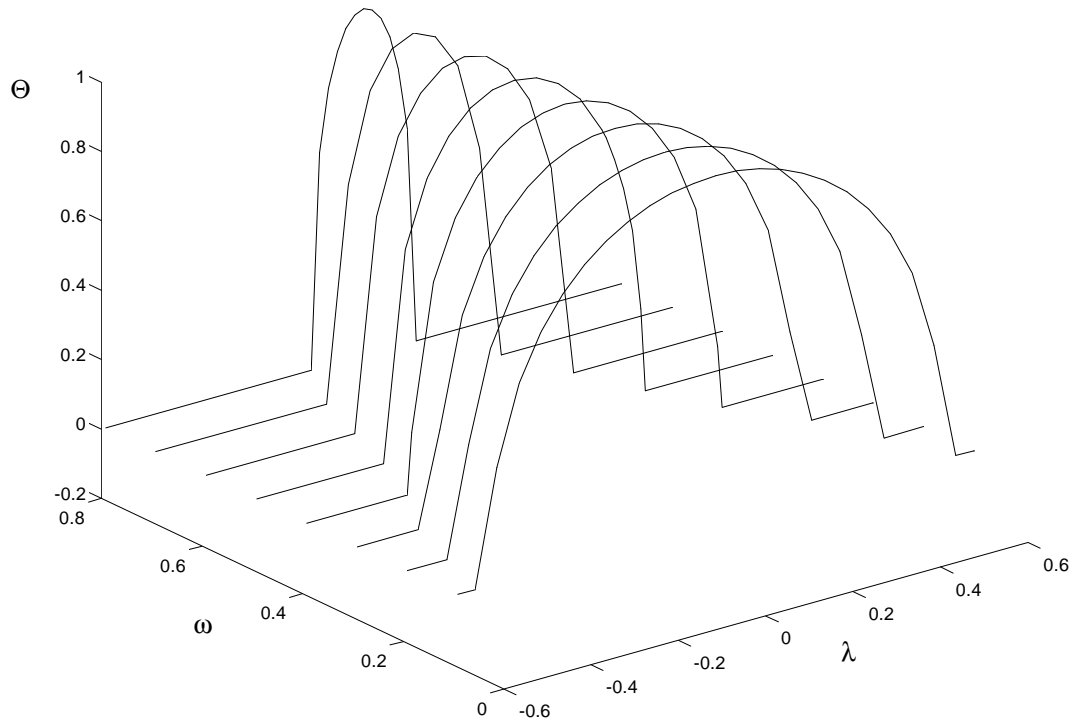


Figure 5.5: The three-dimensional bifurcation diagram for the quiescent solitary wave, showing the effective soliton's asymmetry  $\Theta$  as a function of the frequency  $\omega$  and coupling constant  $\lambda$ .

### 5.6.1.1 Linear Dispersion Relation

The existence range of the soliton solutions in the  $(\lambda, \omega)$ -parametric plane can be found from the linear dispersion relation for Eqs. (5.20)-(5.23). The linear dispersion relation can be found by assuming that the waves  $U_{1,2}$  and  $V_{1,2}$  are small enough that the nonlinear terms are negligible. Eqs. (5.20)-(5.23) will thus become

$$iU_{1t} + iU_{1x} + V_1 + \lambda U_2 = 0,$$

$$iV_{1t} - iV_{1x} + U_1 + \lambda V_2 = 0,$$

$$iU_{2t} + iU_{2x} + V_2 + \lambda U_1 = 0, \quad (5.42)$$

$$iV_{2t} - iV_{2x} + U_2 + \lambda V_1 = 0.$$

Looking for a linearized solution in the form

$$\begin{aligned} U_{1,2} &= u_{1,2} e^{ikx - i\omega t}, \\ V_{1,2} &= v_{1,2} e^{ikx - i\omega t}, \end{aligned} \quad (5.43)$$

Substitute Eqs. (5.43) into Eqs. (5.42) will then give

$$\begin{aligned} (\omega - k)u_1 + v_1 + \lambda u_2 &= 0, \\ u_1 + (\omega + k)v_1 + \lambda v_2 &= 0, \\ \lambda u_1 + (\omega - k)u_2 + v_2 &= 0 \quad (5.44) \\ \lambda v_1 + u_2 + (\omega + k)v_2 &= 0. \end{aligned}$$

or, in the form of a matrix equation,

$$\begin{bmatrix} (\omega - k) & 1 & \lambda & 0 \\ 1 & (\omega + k) & 0 & \lambda \\ \lambda & 0 & (\omega - k) & 1 \\ 0 & \lambda & 1 & (\omega + k) \end{bmatrix} \begin{bmatrix} u_1 \\ v_1 \\ u_2 \\ v_2 \end{bmatrix} = 0. \quad (5.45)$$

Eq. (5.45) can only be satisfied if the determinant of the  $4 \times 4$  coefficient matrix is equal to 0. Evaluation of the determinant will give

$$\omega^4 - 2(k^2 + \lambda^2 + 1)\omega^2 + k^4 + 2(1 - \lambda^2)k^2 + \lambda^4 - 2\lambda^2 + 1 = 0, \quad (5.46)$$

Solving this equation (5.46), the four branches of the dispersion relation in an explicit form are then given by:

$$\omega^2 = \lambda^2 + 1 + k^2 \pm 2\lambda\sqrt{1 + k^2}, \quad (5.47)$$

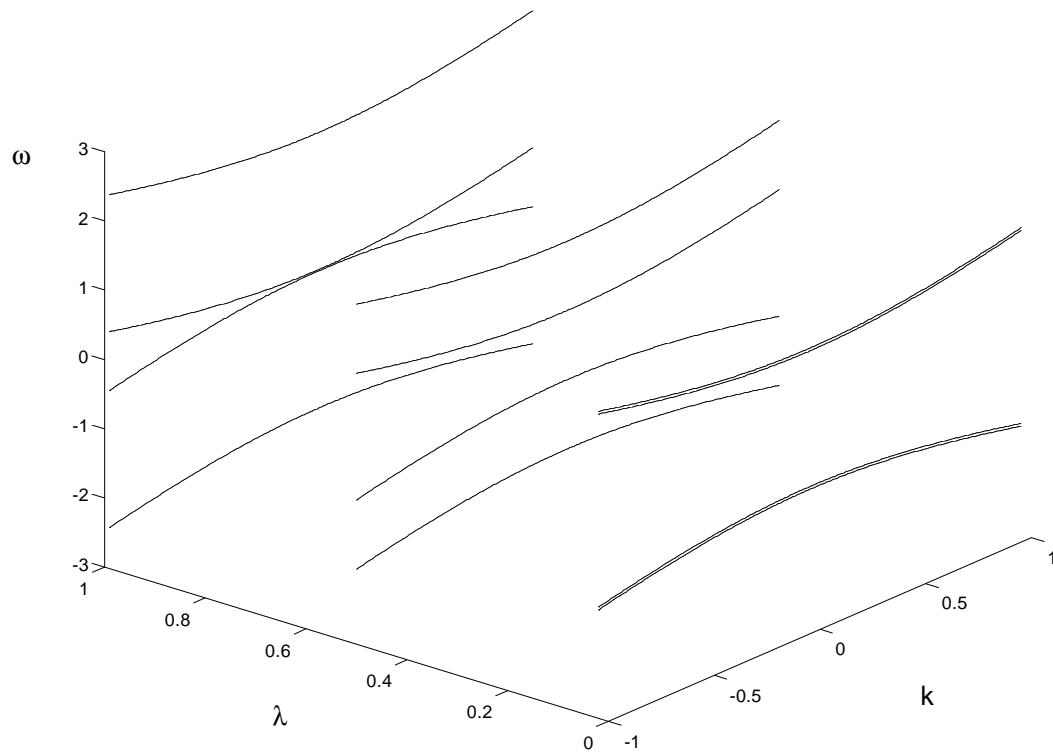


Figure 5.6: A set of the dispersion curves for the linearized equations (5.42) at three different values of the coupling constant:  $\lambda = 0.02$ ,  $\lambda = 0.5$ , and  $\lambda = 0.99$ .

which are displayed in Fig. 5.6. The quiescent solitons can only exist in the gap between the two pairs of the dispersion curves (usually, the soliton solutions exist everywhere in the region where they are allowed by the dispersion relations; however, unexpected lacunas, in which the solitons do not exist, were found in the model of two linearly coupled waveguides with the quadratic nonlinearity [109]). At  $\lambda = 0$ , when the two waveguides decouple, the two pairs of the curves coalesce into just two curves. In this case, the gap is widest:  $-1 < \omega < 1$ . At  $\lambda = 1$  (also at  $\lambda = -1$ , although not shown in Fig. 5.6), the gap gets closed up, i.e., no soliton solution may exist at  $|\lambda| > 1$ . To summarize, the existence range of the quiescent soliton is

confined to  $|\lambda| < 1$  and  $|\omega| < 1$ .

Analysis of a similar issue can be found in [118].

### 5.6.2 Moving Solitary Waves

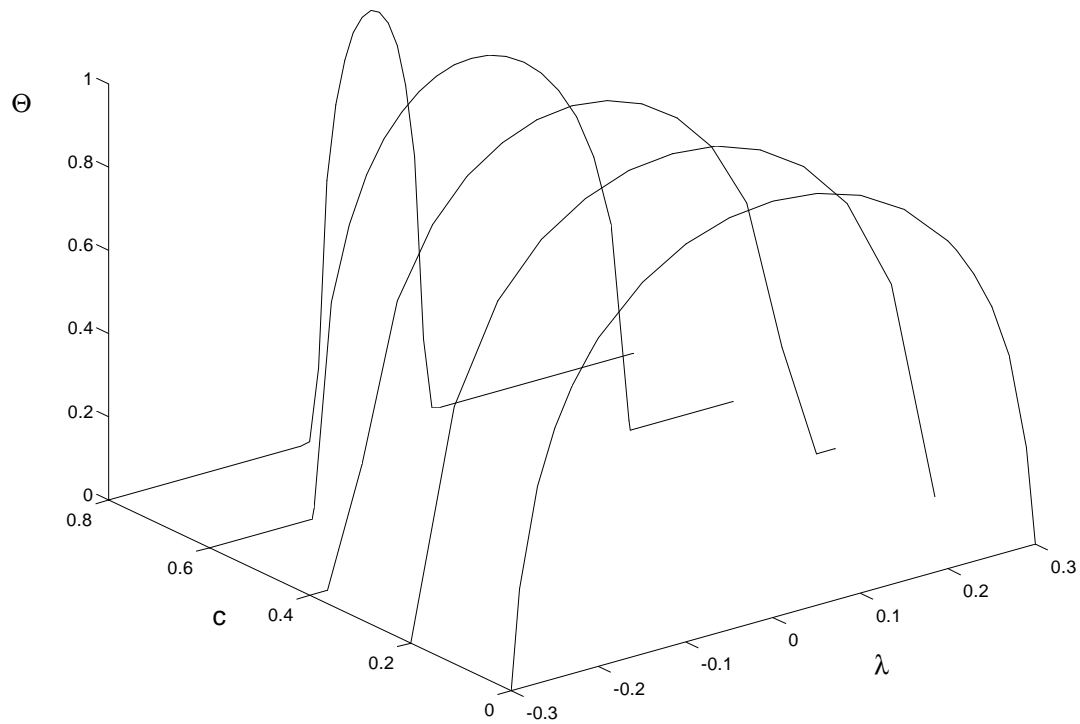


Figure 5.7: The three-dimensional bifurcation diagram for the moving soliton, showing the asymmetry  $\Theta$  vs. the velocity  $c$  and the coupling constant  $\lambda$ .

When the fields travelling in the forward direction,  $U_{1,2}$ , and in the backward direction,  $V_{1,2}$ , (cf. Eqs. (5.20)–(5.23)) do not balance, they interact to form moving (or travelling-wave) solitary wave solutions.

To display a typical example of the results obtained for the moving solitons, we fix  $\omega = 0.5$ . Only the direct finite-difference numerical method was employed to find

the stationary moving solitons. (Recall that stationary solutions mean that they are in the form of Eqs. (5.24).) Fig. 5.7 shows the bifurcation diagram for this case, i.e., the asymmetry parameter  $\Theta$ , defined as per Eq. (5.41), as a function of the soliton's velocity  $c$  and the coupling constant  $\lambda$ . The diagram shows features similar to those noticed above for the quiescent solitons: the asymmetric branches at  $\lambda < 0$  are mirror images of those at  $\lambda > 0$ ; only symmetric solitons exist at large  $|\lambda|$ ; the asymmetric soliton solutions exist only when  $\lambda$  is below the bifurcation value; and the asymmetric branches narrow down as  $c$  increases. We conjecture that the asymmetric branches close up at  $c = 1$ , where the soliton's speed is equal to the light speed. However, this cannot be verified numerically. The numerical scheme gets unstable as  $c$  becomes too close to 1 (no solutions was found for  $c > 0.8$ ). This instability, however, is definitely a numerical artefact rather than a property of the model. Analysis has traced out the inaccuracy of the finite-difference differentiation at the edges of the integration domain to be the origin of the numerical instability. It was observed that the instability can be gradually suppressed by decreasing the grid size of the finite-difference scheme. No solution can be found for  $c > 0.8$  simply because the memory size limit of the computer used restricted further decrease of the grid size.

## 5.7 The Stability Analysis

In this section, we investigate the stability of the stationary solutions by direct simulations of the partial differential equations (5.20)-(5.23), using the split-step Fourier (beam-propagation) method. As the initial configurations, we took the stationary solutions found above by the finite-difference numerical method, with

small arbitrary perturbations added to them.

The study of the stability was done at a number of points inside the regions where the asymmetric solitons exist. The final inferences can be formulated in a fairly simple and general form. It was found that asymmetric solitons, whether they are quiescent or moving, are *always stable* whenever they exist. On the other hand, the symmetric solitons, whenever they coexist with the asymmetric ones at the same values of  $\lambda$ ,  $\omega$ , and  $c$ , are *always unstable*. However, beyond the bifurcation points, where the asymmetric solitons do not exist, the symmetric solitons are *always stable*. These inferences are quite natural, exactly concurring with what one would expect following the lines of the elementary bifurcation theory. We numerically checked the stability of such symmetric solitons; in Fig. 5.8, we show an example of the evolution of a slightly perturbed stable symmetric soliton.

A typical example of the stable asymmetric and the co-existing unstable symmetric solitons is shown in Fig. 5.9. Longer simulations show that the unstable symmetric solitons demonstrate a trend to rearrange themselves into the asymmetric ones existing at the same values of the parameters; however, this is only a trend - the rearranging solitons show strong internal vibrations, which can be suppressed only through emission of dispersive radiation, that would take a very long propagation distance to complete (in [103], it was reported that, in the single-core finite-length fiber with the Bragg grating, a transient needed several round-trip times to settle at typical values of the parameters).

Finally, in Fig. 5.10 we show an example of the evolution of a stable moving asymmetric soliton. Here, the soliton's velocity is quite high,  $c = 0.8$ , showing that the asymmetric solitons still maintain their stability at the high speed. (The apparent oscillations seen in the figure is an artefact produced by the way the graph-

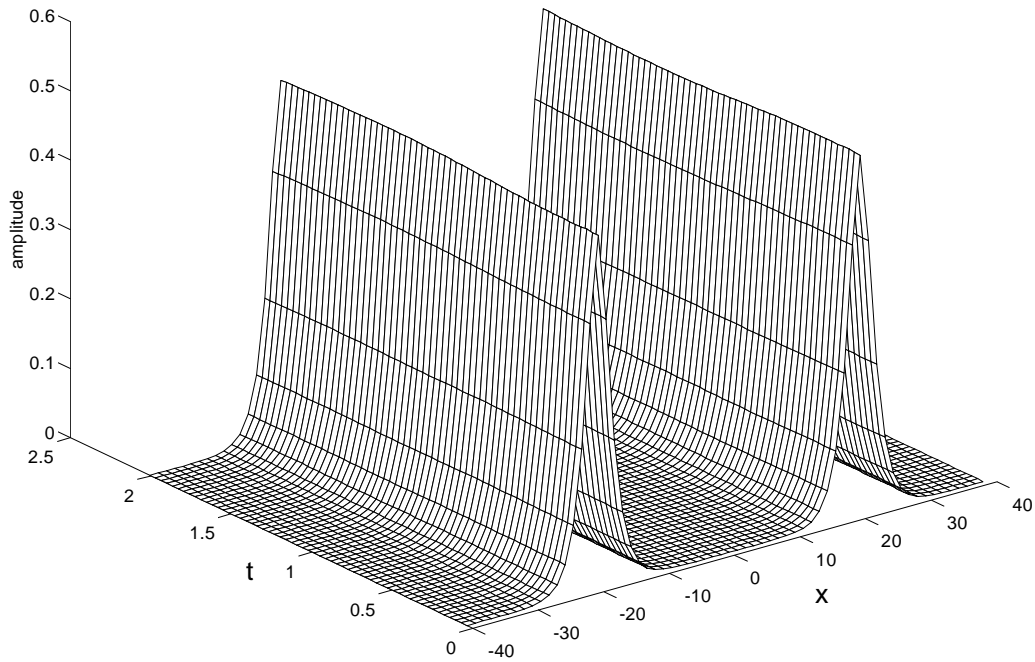


Figure 5.8: The evolution of a slightly perturbed stable quiescent symmetric soliton. Here,  $\lambda = 0.4$ , and  $\omega = 0.4$ , at which no asymmetric soliton exists.

plotting routine was processing the data: it could only display the values at the cross points of the grid lines. So, when the peak values of the waves were located between two longitudinal grid lines, the maximum values had no way to show up, causing the illusive dips.)

## 5.8 Discussion

Although experimental generation of the solitons in the dual-core nonlinear optical fiber with the gratings is not going to be easy, one may expect that this is not

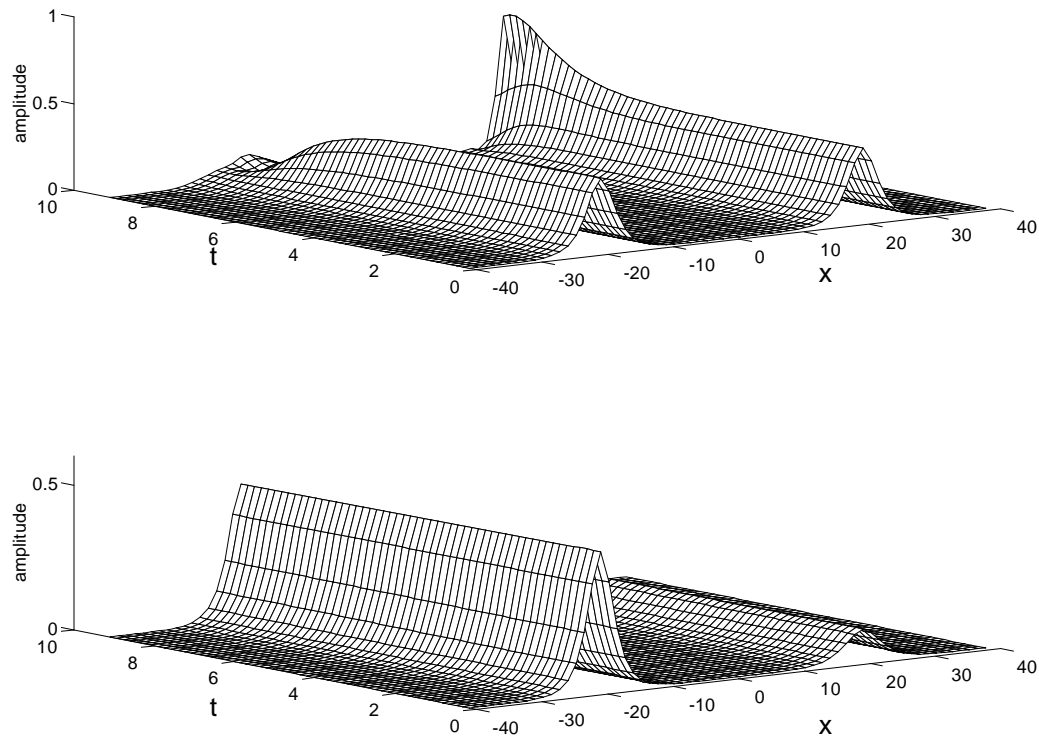


Figure 5.9: The evolution of slightly perturbed symmetric (upper) and asymmetric (lower) quiescent solitons at  $\omega = 0.8$  and  $\lambda = 0.16$ .

unrealistic. Indeed, a characteristic propagation length necessary for formation of the soliton in the recent experiments done with the single-core fiber was  $\sim 2$  cm [101] (while the actual length of the grating was 5.5 cm; actually, gratings up to 1 m long can be fabricated by means of the available technology [104]). At the same time, a typical coupling length in the real dual-core fibers is a few centimeters (but if necessary, it may also be extended to  $\sim 1$  m or even more). The fact that these two important lengths are of the same order makes it possible to expect the existence of solitons whose propagation period will be simultaneously commensurate with both lengths, so that the Bragg scattering and the linear coupling between the cores will

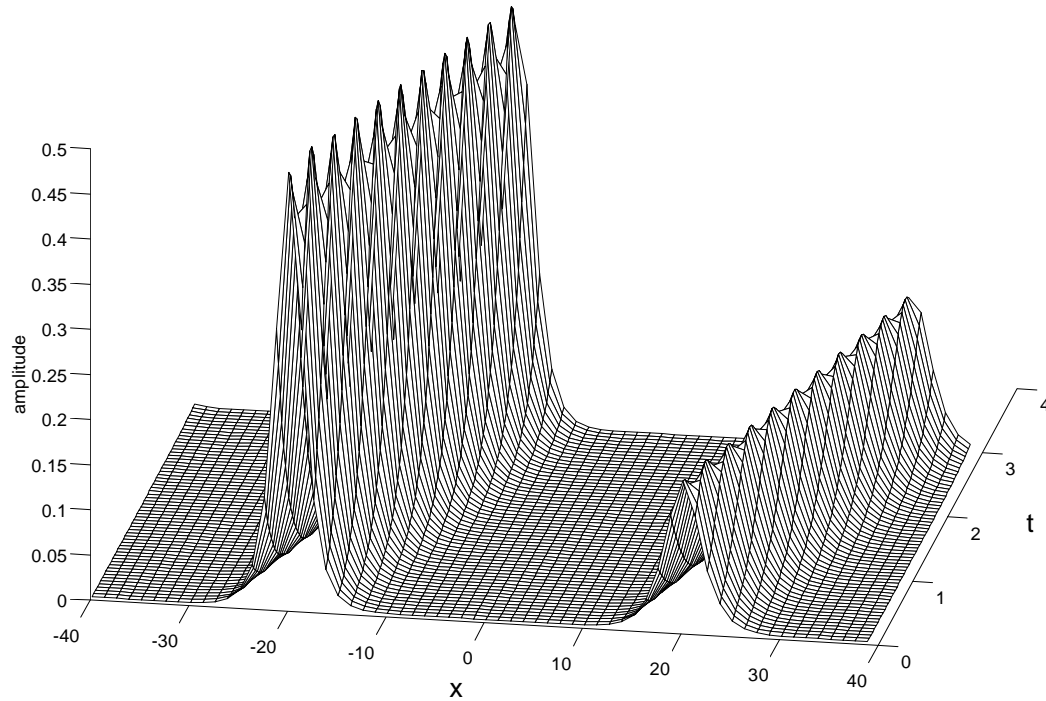


Figure 5.10: The evolution of a slightly perturbed moving asymmetric soliton. Here,  $\omega = 0.5$ ,  $\lambda = 0.04$ , and  $c = 0.8$ .

be equally essential for the soliton. It is also important that, as it follows from what was said above, it is technologically possible to fabricate a relatively long dual-core nonlinear optical fiber with the gratings written on the cores, so that the soliton will have enough room to be observed. As for its expected temporal width, one may conjecture, following the available experimental data [101], that it will be between 15 and 80 picoseconds. At this stage of the theoretical study of the newly proposed system, it would be too early to specify the physical parameters more definitely. Lastly, it is relevant to mention that the dual-core fiber with the gratings is the most straightforward but not the single nonlinear optical medium in terms of which

the model introduced in this work can be realized. Another possible medium is based on parallel-coupled planar nonlinear waveguides, each carrying a grating in the form of a system of parallel scores; in that case, essentially the same model will describe *spatial* solitons rather than temporal ones in the fiber. One can also think of parallel-coupled semiconductor waveguides with periodically corrugated boundaries, although nonlinear absorption may be a problem in the latter system.

A potential for applications of the solitons in both the dual-core nonlinear fibers and in the nonlinear single-core ones equipped with the Bragg grating is well known (switching, bistability, pulse compression, etc., see, e.g., [17, 64] and [104]). The solitons in the dual-core fibers with the gratings may find a still broader field for the applications, as they combine properties of the solitons in both types of the systems, and may be controlled by a larger numbers of parameters.

We will also discuss some additional essential points here. A crucial concept in the Bragg grating theory is a parameter called the effective dispersion [87, 88, 103]. It is defined as the local curvature of the upper dispersion branch at the point where the Bragg grating soliton resides (for the self-focusing nonlinearity, the Bragg-grating soliton can only form on the upper branch of the dispersion curve, where the effective dispersion is anomalous). This definition is based on the reduction of the nonlinear coupled mode equations [89] to the nonlinear Schrödinger equation in the BF approach [99]. The BF approach relies upon approximating the electric field by the Bloch functions on the upper branch (if we limit ourselves to the focusing nonlinearity), which implies that the frequency content of the field must concentrate around the upper edge of the gap. This precludes not only fields with frequency elsewhere in the gap, but also temporally narrow optical pulses with a spectral width of the same order of magnitude as the gap width. This limitation prevented our use

of the local dispersion parameter in this work, as we basically consider *gap soliton* inside the photonic band gap. When the Bloch functions corresponding to the upper and lower branches are equally important, the definition of this effective dispersion parameter is not straightforward. On the other hand, the MTM approach adopted in this work makes the use of this parameter unnecessary.

It is also relevant to discuss the frequency spectrum of the solitons studied in this work. As already mentioned in section 5.5, the values  $\omega = \pm 1$  of the normalized frequency detuning correspond to the soliton's central frequency being at the edges of the photonic band gap. From Eqs. (5.24), it follows that, at the zero soliton's velocity  $c$ , the field envelopes  $U_{1,2}$  and  $V_{1,2}$  have a pure harmonic time dependence. Therefore, at  $c = 0$ , the soliton has zero spectral width. Note that this conforms to what can be deduced from the exact solutions of the single-waveguide case as obtained in [71, 72]. At  $c \neq 0$ , the variable  $\xi$  in Eqs. (5.24) has a time dependence, which leads to a finite spectral width of the soliton. It can be deduced from Eqs. (5.24) that the normalized spectral width will increase with  $c$ . This conforms to the findings in [89] for the single-waveguide case. However, because the main subject of this investigation are the bifurcations and stability of the asymmetric and symmetric solitons, a more detailed calculation of this spectral width was not carried out.

The last topic to be discussed here is the modulational instability of distributed feedback structures. There had been several studies relating to this issue [71, 73, 93, 117]. In them, it was found that the modulational instability initiated conversion an input continuous-wave beam into a train of spiky self-pulsations. In a recent paper [87], a breakup of the Bragg-grating solitons into multiple sharp pulses was observed, which was attributed to the modulational instability. It clearly follows

from our numerical results that the instability of the symmetric solitons (when they are unstable) is clearly *not* of the same type. The instabilities found in this work can be adequately explained by the standard bifurcation theory.

## 5.9 Conclusion

In this work, we have investigated a model describing two linearly coupled waveguides with the cubic nonlinearity, each equipped with the resonant grating.

Using the variational and direct numerical approach, both methods demonstrate the existence of asymmetric solitary wave solutions, alongside the obvious symmetric solitons. The bifurcation diagrams were constructed.

Then, the stability of both asymmetric and symmetric solitons was tested by BPM simulations. The asymmetric solitons, whenever they exist, were shown to be always stable, while the symmetric ones coexisting with them are always unstable. Nevertheless, the symmetric solitons are stable beyond the bifurcation points, where they do not have to coexist with asymmetric solitons.

# Chapter 6

## Three Wave Gap Solitons

### 6.1 Introduction

In a medium without the center of symmetry, quadratic nonlinearity results in parametric three-wave mixing. Two waves, which are in resonant interaction, create a third wave at a combined frequency  $\omega_3 = \omega_1 + \omega_2$ . There is an energy exchange among these three waves of different carrier frequencies. In a degenerate case, two of the waves at the lower frequency are identical. These waves thus correspond to fundamental harmonic (FH) waves. Their interaction will then create a second harmonic (SH) wave, which at the same time, also is down-converted to the FH waves. Such interaction is known as type I second harmonic generation (SHG). In the previous chapters, what we consider, therefore, belonged to type I interaction.

In the particular case when the two lower frequency waves have the same carrier frequency (thus they are FHs), but different polarizations. The two orthogonally polarized FH waves are, so, not identical. This case of three-wave interaction is known as type II SHG [119]. The SH field down-converts to both components of

the FH field.

Observation of the large phase shift in the potassium titanyl phosphate (KTP) crystals, and the suggestion of using it to induce a self-focusing effect [120], have inspired a new surge of studies of solitons generated by mutual trapping of the FH and SH waves in a waveguide (see a review [43]).

In the most physically realistic case, solitons observed in planar waveguides or bulk media are *spatial solitons*, generated by the competition between the cascaded nonlinearity and the spatial diffraction. A great deal of interest to this field is attracted by unique chance to study solitons in a new physical setting, as well as by the potential that the spatial solitons have for implementation of *all-optical switching* in multichannel optical communication systems, the lack of which in a technologically acceptable form is, in fact, the most important problem hindering further progress of optical communications.

When the dispersion or diffraction may be neglected in certain circumstances, it has been investigated in a number of studies [121]-[128]. Note that the three-wave resonance interaction (3WRI) model with group-velocity differences between the waves but *without* diffraction or dispersion is exactly integrable by means of the inverse scattering transform [129] (moreover, this model is integrable too in the multidimensional case). In [130], 3WRI under exact phase-matched conditions was investigated.

In a real experiment, it is essentially easier to achieve the necessary phase matching between the FH and SH through the type-II interaction than through the type-I interaction that involves a single FH component. Actually, the  $\chi^{(2)}$  interaction that gave rise to the spatial solitons observed in [41, 42] belonged to the type-II. This type of the SHG is also preferable for the above-mentioned application to the all-

optical switching, as it is easy to control, by affecting the FH polarization. A lot of experiments, generating high-energy, ultrashort optical pulses, were also achieved using the type-II phase matching technique [131]-[139].

Theoretical studies of 3WRI in the presence of diffraction or dispersion have commenced recently [75, 140, 141]. In [141], particular exact soliton solutions were found; in [75], a general two-parameter family of solitons was constructed by means of both the VA and direct numerical methods, and domains of stable and unstable solitons were identified. Further results concerning the stability of the solitons supported by the 3WRI can be found in [76, 142, 143]. In [142], it was pointed out that 3WRI may give rise to a multistability of the soliton solutions in a limited range of parameters. In [76, 143], analytical stability criteria of the three-wave soliton were derived, and verified numerically.

## 6.2 Scope of Study

In this chapter, we consider solitary waves due to three-wave mixing in a quadratic medium, which has parallel scores (stratified layers in the direction of propagation of the SH wave) inscribed in it, i.e., a resonant grating. The FH waves are chosen so that their carrier wave vectors have equal lengths, and they travel in directions making small, equal but opposite angles with the parallel scores (which is also the direction of the  $Z$ -axis). The SH wave, thus, travels in parallel with the  $Z$ -axis (See Fig. 6.1). The FH waves suffer the Bragg reflection, which couples them to each other, and are thus subjected to a strong effective dispersion or diffraction. This is very significant, because then, it is much easier to achieve the FH-SH phase matching, which is fundamentally necessary to use the  $\chi^{(2)}$  nonlinearity to form

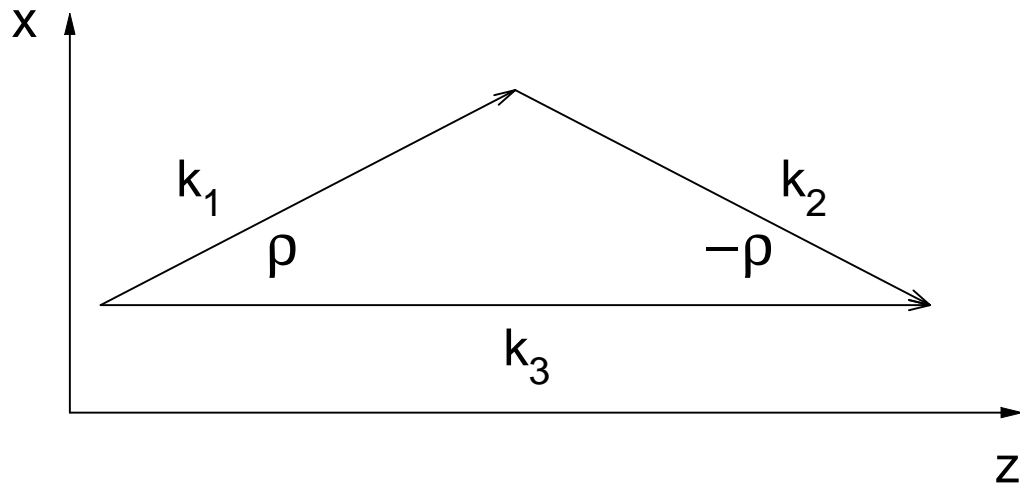


Figure 6.1: The configuration of the wave vectors  $\mathbf{k}_1$ ,  $\mathbf{k}_2$ , and  $\mathbf{k}_3$  of the two components of the fundamental harmonic and of the second harmonic. The scores that form the spatial grating are parallel to the  $z$  axis.

solitons. Theoretical results for the four-wave gap solitons in the temporal domain, in  $\chi^{(3)}$  medium with the Bragg gratings, was discussed in detail in the last chapter. For gap solitons, supported by SHG in combination with the Bragg gratings, can be found in [109, 110, 111, 144]. Here in this chapter, the resonant interaction of the three waves will give rise to *three-wave* spatial solitons, in which the SH wave couples to the two FH components through the nonlinearity.

Since the FH components are assumed to travel at an angle with the gratings, the mathematical model of this system includes transverse-walkoff terms in the equations for the two FH components. These transverse-walkoff terms give rise to an effective diffraction which is definitely much stronger than that of the intrinsic second-derivative diffraction [75]. Therefore, the second-derivative diffraction terms can be dropped in the FH equations. On the other hand, since the SH wave travels in parallel with the grating, it does not interact with the grating, and we have to

keep the second-derivative diffraction term in the SH equation.

A similar model was a starting point in the work [108], but an important difference is that a very large phase mismatch between the SH and FHs was assumed, to allow one to eliminate the SH component, transforming the system into the *massive Thirring model* (MTM) [95], which is exactly integrable by means of the inverse scattering transform [96, 145] (an optical fiber with the Bragg grating and *cubic* (Kerr) nonlinearity is described by a well-known nonintegrable generalization of MTM [71, 72]). Since all the soliton solutions of the integrable MTM are stable, the solitons considered in [108] are also always stable. In the present work, we do not assume that the phase mismatch is specially large, and keep the SH component in the model explicitly. Obviously, the case of a smaller mismatch is more physically interesting. We will demonstrate that stable three-wave soliton solutions do exist at a large mismatch, and they continue to exist as the phase mismatch is decreased. However, we find a *threshold value* of the mismatch, below which the soliton solutions lose their stability (though they do not disappear). An instability threshold in terms of the mismatch parameter is also known for the usual  $\chi^{(2)}$  solitons [40, 58, 75, 76]; however, the principal difference is that the usual solitons are *stable* in the fully matched case, while our solitons may be both stable and unstable in this case, depending on other parameters (the wave number shift and an effective SH diffraction parameter), i.e., the location of the instability threshold is different in the present model. We also investigated the effect of changing the SH diffraction (dispersion) coefficient, finding that it has less effect on the threshold than the wave number shift and the wave-vector mismatch.

Finally, we will consider two-soliton bound-state solutions (or simply two-solitons), finding that they have their own stability threshold (which is higher than but close

to the one for the fundamental solitons). The fact that two-solitons in our model can be stable is quite nontrivial, as, in the usual  $\chi^{(2)}$  models, all the higher-order solitons are subject to an instability [43, 47].

### 6.3 The Model

We consider the resonant nonlinear interaction of two FH waves with identical frequencies  $\omega$  and  $Z$ -components of their carrier wave vectors  $k_1$  and  $k_2$ . The  $\chi^{(2)}$  nonlinearity generates the third wave with wave number  $k_3$  at the frequency  $2\omega$ . The case of interest is  $\Delta k \ll k_3$ , where  $\Delta k \equiv k_1 + k_2 - k_3$  is the wave-vector mismatch. We assume that the FH wave vectors make small angles  $\pm\rho$  with the  $Z$ -direction, and have the same length, so that  $k_1 = k_2 \equiv k$ . (See Fig. 6.1.) Assuming the amplitudes  $E_1$ ,  $E_2$ , and  $E_3$  of the interacting harmonics to be slowly varying in comparison with the carrier waves and employing same techniques as elaborated in Chapter 1, and in the last chapter, one can derive the following system of the amplitude equations:

$$\begin{aligned} 2ik \frac{\partial E_1}{\partial Z} + 2ik\rho \frac{\partial E_1}{\partial X} + \lambda E_2 + \chi E_3 E_2^* e^{i\Delta k Z} &= 0, \\ 2ik \frac{\partial E_2}{\partial Z} - 2ik\rho \frac{\partial E_2}{\partial X} + \lambda E_1 + \chi E_3 E_1^* e^{i\Delta k Z} &= 0, \\ 2ik_3 \frac{\partial E_3}{\partial Z} + \frac{\partial^2 E_3}{\partial X^2} + \tilde{\chi} E_1 E_2 e^{i\Delta k Z} &= 0, \end{aligned} \tag{6.1}$$

where  $\chi \equiv (4\pi\omega^2/kc^2)\chi^{(2)}(\omega; 2\omega, -\omega)$ ,  $\tilde{\chi} \equiv (8\pi\omega^2/k_3c^2)\chi^{(2)}(2\omega; \omega, \omega)$ ,  $\lambda$  being the coupling constant induced by the Bragg scattering. We can then rescale Eq. (6.1) by setting

$$E_1 \equiv \lambda v_1 / \sqrt{\chi \tilde{\chi}}, \quad E_2 \equiv \lambda v_2 / \sqrt{\chi \tilde{\chi}}, \quad E_3 \equiv (\lambda/\chi) v_3 \exp(i\Delta k Z),$$

$$Z \equiv 2kz/\lambda, \text{ and } X \equiv 2\rho kx/\lambda.$$

Additionally, using the fact that  $k_3/k \approx 2$ , and defining the effective mismatch  $q \equiv 4k\Delta k/\lambda$  (note that the parameter  $q$  here carries the same meaning as the  $q$  parameter which was used in Chapters 2 to 4, although the definitions differ slightly due to the use of different normalization schemes), and the diffraction parameter  $D \equiv \lambda/(4\rho^2 k^2)$ , we arrive at the system in the normalized form,

$$\begin{aligned} i\frac{\partial v_1}{\partial z} + i\frac{\partial v_1}{\partial x} + v_2 + v_3 v_2^* &= 0, \\ i\frac{\partial v_2}{\partial z} - i\frac{\partial v_2}{\partial x} + v_1 + v_3 v_1^* &= 0, \\ 2i\frac{\partial v_3}{\partial z} - qv_3 + D\frac{\partial^2 v_3}{\partial x^2} + v_1 v_2 &= 0. \end{aligned} \tag{6.2}$$

Using obvious symmetry properties of the system (6.2), we can confine ourselves to the case  $D > 0$  without the loss of generality.

We are interested in stationary solutions to Eqs. (6.2), in the form  $v_1 = e^{ikz} u_1(x)$ ,  $v_2 = e^{ikz} u_2(x)$ , and  $v_3 = e^{2ikz} u_3(x)$ , where  $k$  is a common wave-number shift of the harmonics. Thus, we obtain from Eqs. (6.2) a system,

$$\begin{aligned} ku_1 + iu_1' + u_2 + u_3 u_2^* &= 0, & ku_2 - iu_2' + u_1 + u_3 u_1^* &= 0, \\ (4k + q)u_3 + Du_3'' + u_1 u_2 &= 0, \end{aligned} \tag{6.3}$$

the prime standing for  $d/dx$ . We can impose a natural reduction,  $u_1 = u_2^* \equiv u$ , on the amplitudes  $u_1$  and  $u_2$ , which is compatible with Eqs. (6.2). Substituting this into Eqs. (6.3), we finally obtain the following equations for the complex function  $u(x)$  and real  $u_3(x)$ ,

$$\begin{aligned} ku + iu' - u_3 u - u^* &= 0, \\ (4k + q)u_3 + Du_3'' - |u|^2 &= 0. \end{aligned} \tag{6.4}$$

This is the simplest version of the model to produce the three-wave solitons in the  $\chi^{(2)}$  media.

## 6.4 The Linearized and Semilinearized Systems

First of all, it is useful to analyze the linearized version of the system (6.4); i.e.,

$$\begin{aligned} ku + iu' - u^* &= 0, \\ (4k + q)u_3 + Du_3'' &= 0. \end{aligned} \quad (6.5)$$

Obviously, the linearized equations get decoupled. Looking for a solution in the form

$$u \sim \exp(-\mu|x|), \quad u_3 \sim \exp(-\mu_3|x|), \quad (6.6)$$

corresponding to an exponentially decaying tail of the soliton, it is straightforward to find, by substituting Eqs. (6.6) into Eqs. (6.5),

$$\mu^2 = 1 - k^2, \quad \mu_3^2 = D^{-1}(4k + q). \quad (6.7)$$

A necessary condition for the existence of the soliton is  $\mu^2 > 0$ , i.e., according to (6.7),  $|k| < 1$ . This restriction on the allowed values of the propagation constant implies that we are dealing with *gap solitons*, which is typical for all the model involving the Bragg scattering [71, 72]. Another necessary condition,  $4k + q > 0$ , is imposed by demanding  $\mu_3^2 > 0$  (recall, we set, by definition,  $D > 0$ ). However, the expression (6.7) for  $\mu_3^2$  makes sense only if  $\mu_3 \leq 2\mu$ , or, in an explicit form,

$$q \leq q_0(k) \equiv 4D(1 - k^2) - 4k, \quad (6.8)$$

otherwise the quadratic term in the second equation (6.4) dominates over the linear ones at  $|x| \rightarrow \infty$ .

Thus, we arrive at a conclusion that the  $\chi^2$  solitons may be of two different types, within the framework of the same model. In the region (6.8), supplemented by the necessary condition  $|k| < 1$ , the tails of both the FH and SH components of the soliton are governed by the decoupled linearized equations and have the form given by Eqs. (6.6) and (6.7), in which case the solitons can be naturally called *free-tail* ones. However, in the opposite case, the equation for the SH component (the second equation of the system (6.4)) *cannot* be linearized, hence the soliton's tails are determined, in this case, by a *semilinear* system,

$$ku + iu' - u^* = 0, \quad (4k + q)u_3 + Du_3'' = |u|^2. \quad (6.9)$$

A general solution to Eqs. (6.9) describing the soliton's tails is (cf. Eqs. (6.6) and (6.7)), if  $k < 0$ :

$$u = A \exp\left(\frac{i}{2} \sin^{-1}\left(\sqrt{1 - k^2}\right)\right) \exp\left(-\sqrt{1 - k^2}|x|\right), \quad (6.10)$$

$$u_3 = A^2 \left[4D(1 - k^2) - (4k + q)\right]^{-1} \exp\left(-2\sqrt{1 - k^2}|x|\right), \quad (6.11)$$

$A$  being an arbitrary real constant, and, in the case  $k > 0$ ,  $u \rightarrow iu^*$ . Of course, the solution (6.10) for the FH tail is exactly the same as in the case of the free-tail soliton; however, the solution (6.11) for the SH tail is very different, being locked to the FH tail, so that the solitons of this type may be called *tail-locked*.

Note that the boundary between the free-tail and tail-locked solitons,  $q = q_0(k)$  (see Eq. (6.8)), may also be defined as the point of the *exact matching* between FH and SH, following the analogy with the usual  $\chi^{(2)}$  models.

## 6.5 Analytical and Numerical Techniques

To find soliton solutions to the full nonlinear equations (6.4), analytical and numerical methods were employed. The same analytical method based on VA and the same numerical finite-difference method used in earlier chapters were used. Such a two-step approach has proved to be very efficient in all the problems described in these earlier chapters.

To apply VA, we need the Lagrangian for Eqs. (6.4),  $L = \int_{-\infty}^{+\infty} \mathcal{L} dx$ , with the density

$$\mathcal{L} = k|u|^2 - \frac{1}{2}(q+4k)u_3^2 + \frac{i}{2}[u'u^* - (u^*)'u] - \frac{1}{2}D(u_3')^2 - |u|^2 u_3 - \frac{1}{2}[u^2 + (u^*)^2]. \quad (6.12)$$

Then, we adopt the following complex *ansatz* for the solutions sought for:

$$u = A \operatorname{sech}(\mu x) + iB \sinh(\mu x) \operatorname{sech}^2(\mu x), \quad u_3 = A_3 \operatorname{sech}(\mu x), \quad (6.13)$$

where the soliton's amplitudes  $A$ ,  $A_3$ , and  $B$  and the inverse width  $\mu$  are free parameters to be found by means of VA. Insertion of Eqs. (6.13) into Eq. (6.12) and integration generate an *effective Lagrangian*  $L$ . We then follow the variational formalism to derive the VA equations:  $\partial L/\partial A = 0$ ,  $\partial L/\partial B = 0$ ,  $\partial L/\partial A_3 = 0$ , and  $\partial L/\partial \mu = 0$ . The resulting algebraic equations are:

$$\begin{aligned} 4\mu^{-1}(1+k)A + \frac{4}{3}B + \pi\mu^{-1}AA_3 &= 0, \\ \frac{4}{3}\mu^{-1}(1-k)B - \frac{4}{3}A - \frac{\pi}{4}\mu^{-1}A_3B &= 0, \\ 2\mu^{-1}(q-4k)A_3 - \frac{2}{3}D\mu A_3 - \frac{\pi}{8}\mu^{-1}B^2 - \frac{\pi}{2}\mu^{-1}A^2 &= 0, \\ \mu^{-2} \left[ 2(1+k)A^2 + \frac{2}{3}(1-k)B^2 + (q-4k)A_3^2 - \frac{\pi}{2}A^2A_3 - \frac{\pi}{8}A_3B^2 \right] \\ \frac{1}{3}DA_3^2 &= 0. \end{aligned} \quad (6.14)$$

This set of algebraic equations was solved numerically, using the Newton-Raphson Method, described in Section (3.3.2). Other details of the procedure are straightforward. After this, the stationary-soliton solutions to Eqs. (6.4) were obtained by means of the direct finite-difference numerical scheme (see Section (3.3.3)). The results produced by these methods are displayed and commented below.

## 6.6 Stationary Solutions: Existence and Stability

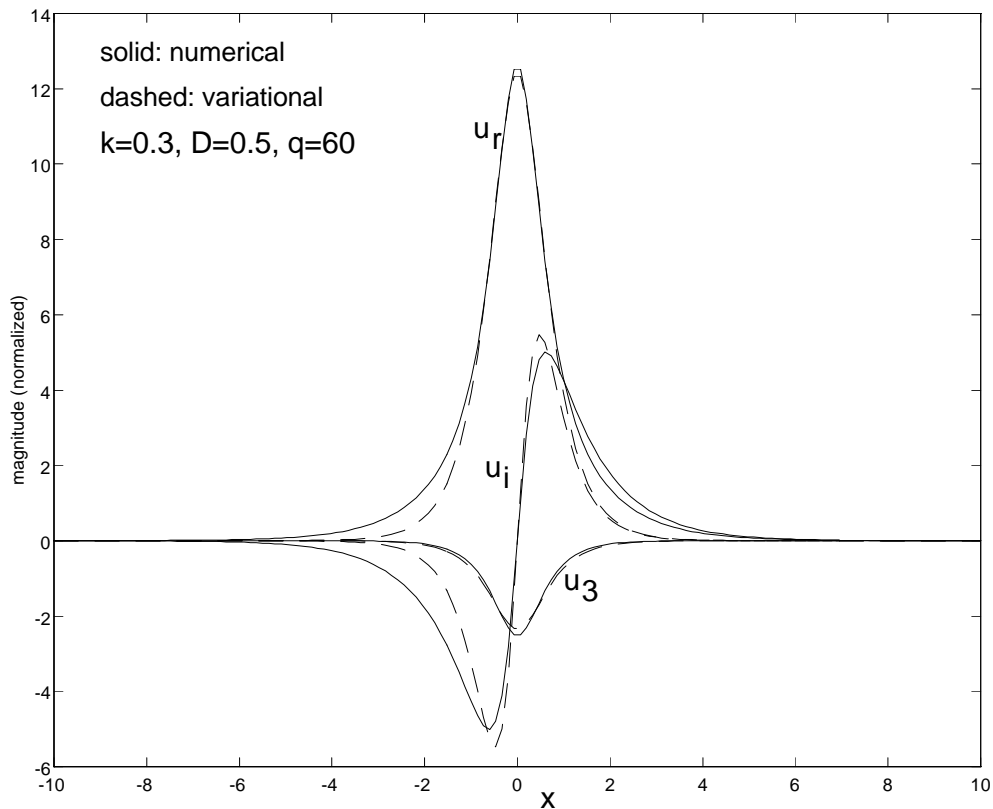


Figure 6.2: A typical example of the comparison between the numerical (solid curves) and variational (dashed curves) fundamental-soliton solutions for the real ( $u_r$ ) and imaginary ( $u_i$ ) parts of the fundamental-harmonic component and the real second-harmonic component ( $u_3$ ). The values of the parameters are:  $k = 0.3$ ,  $D = 0.5$ , and  $q = 60$ .

Stationary solutions were found using both the numerical and the variational methods. Similar to the solutions found in [108], the fundamental harmonic components are complex, with the real parts being even functions and the imaginary parts being odd functions of  $x$ . The second harmonic components are real, and with an opposite polarity to the real parts of the fundamental harmonics.

Plots of the different components of a typical fundamental-soliton solution are shown in Fig. 6.2. Comparison of the solutions obtained, by means of the analytical and numerical methods, is also presented there (a relatively large value of the normalized mismatch,  $q = 60$ , is selected for this figure; however, this corresponds to a point just within the region of stable fundamental solitons, see Fig. 6.7 below). It is seen that the agreement is acceptable, especially in view of the fairly simple form of the *ansatz* (6.13).

In Figs. 6.3 – 6.6, we present a numerically obtained *family* of the fundamental soliton solutions to Eqs. (6.4), in the form of three-dimensional plots showing the dependence of the basic characteristics of the fundamental-soliton, viz., the amplitudes and widths of its two FH components  $u$  and SH  $u_3$  vs. the mismatch  $q$  and wave-number shift  $k$ , the diffraction coefficient  $D$  being fixed at a realistic value 0.5. The width of the  $u_3$ -component turns out to be quite close to (more accurately, slightly smaller than) the  $u$ -component's width (note that the *ansatz* (6.13) adopted above as the basis of VA assumed both components to have identically equal widths). Here, the standard definition of the FWHM width is applied to the absolute values of the complex fields, and the amplitudes refer to their peak values.

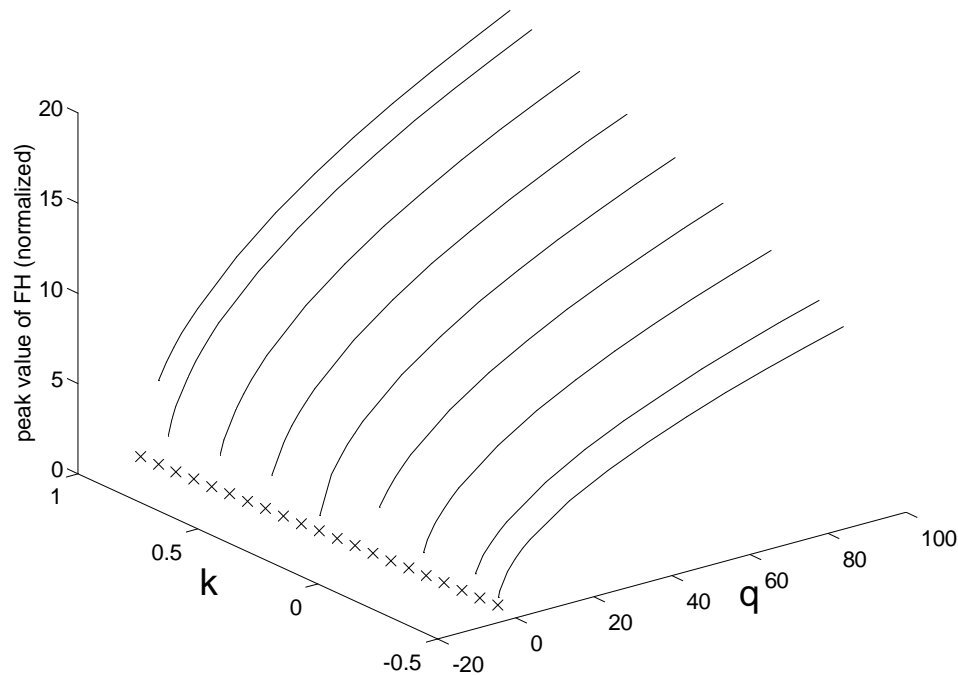


Figure 6.3: The family of the fundamental-soliton solutions: the FH ( $u$ ) amplitude is plotted vs. the wave-number shift  $k$  and phase mismatch  $q$ , while the SH diffraction parameter is fixed at  $D = 0.5$ .

A general trend seen in these plots is that the amplitudes of the soliton's components increase, whereas their widths decrease, with the increase of  $q$  and  $k$ . Another clearly seen, and quite natural, feature is that the FH and SH amplitudes are on the same order of magnitude at small values of the mismatch  $q$ , while at large  $q$  the FH amplitude is much larger. In Fig. 6.3 and Fig. 6.4, we also indicate the soliton existence limit as implied by Eq. (6.7); i.e.,  $4k + q > 0$  (shown by the crosses on the base plane). It can be seen that the trend of decreasing amplitudes and increasing widths accelerates rapidly as this soliton existence limit is approached. A similar trend is observed as another existence limit,  $k = -1$ , is approached, although no curves beyond  $k = -0.5$  were drawn, because, in this region, the numerical

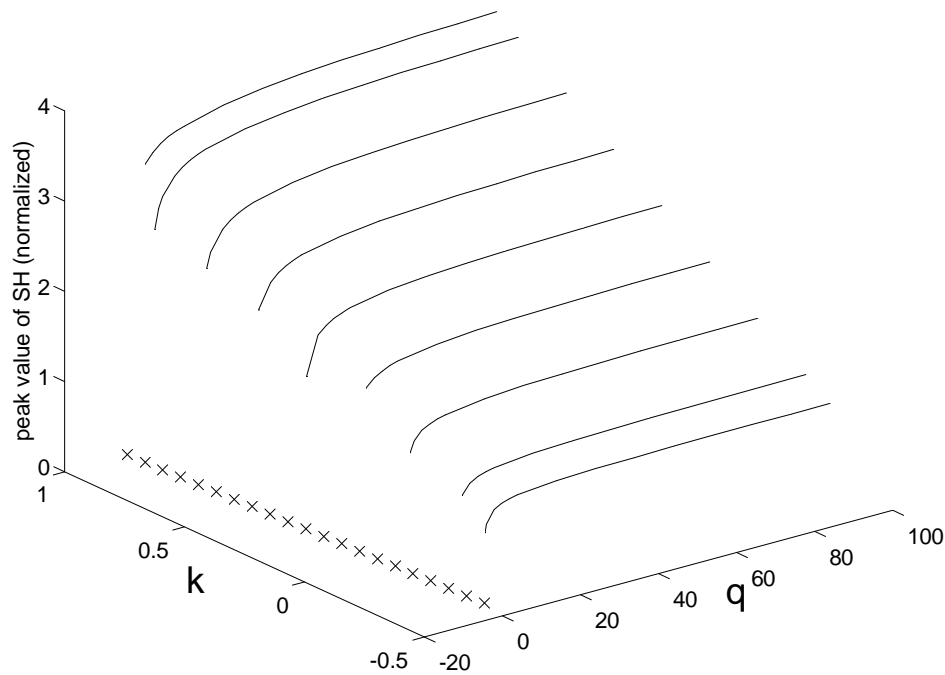


Figure 6.4: The family of the fundamental-soliton solutions: the SH ( $u_3$ ) amplitude. The line consisting of crosses in both Figs. 6.3 and 6.4 shows the existence boundary  $4k + q = 0$  for the tail-free solitons.

scheme converges too slowly, which makes it difficult to accumulate enough data for drawing the continuous curves. However, an *opposite* trend is seen as yet another soliton existence limit,  $k = 1$ , is approached: the amplitudes and widths keep on, respectively, increasing and decreasing, which is quite surprising, because from Eq. (6.7), one would expect that the width should diverge at both limits,  $k = \pm 1$ . This unexpected trend does not reverse up to the value,  $k = 0.99$ . At  $k = +1$ , the amplitude remains finite; however, the soliton becomes delocalized with a small finite-amplitude cw (continuous wave) oscillatory tail. (Such delocalized soliton solutions were previously discussed in detail in [79].) This, in turn, is in accord with Eq. (6.7), which can also be interpreted as that the exponentially decaying soliton

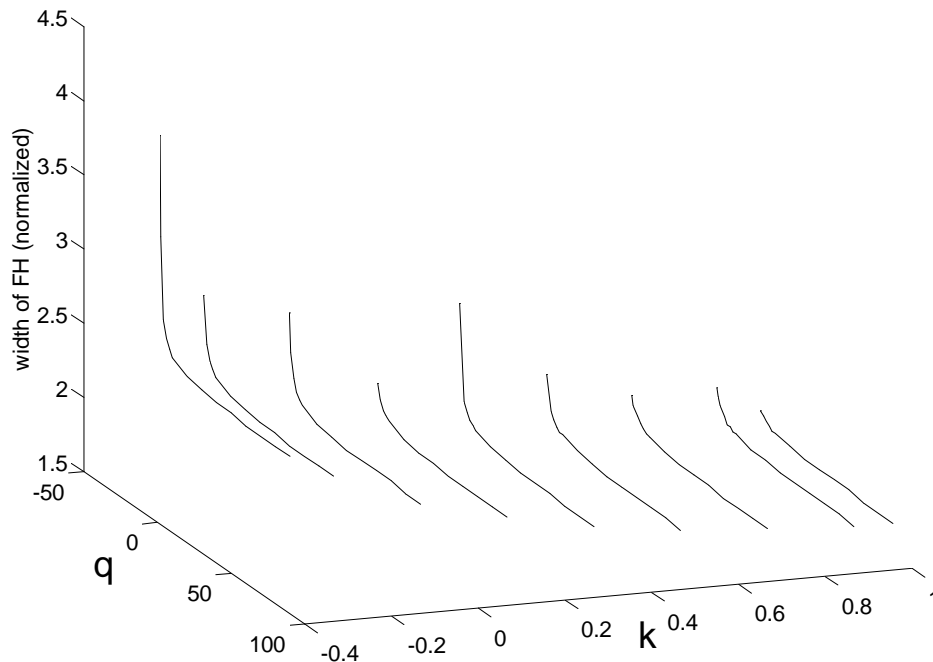


Figure 6.5: The family of the fundamental-soliton solutions: the FH width.

tail is changed to a nonvanishing oscillatory cw. No solutions can be numerically found for  $k > 1$ . However, since a delocalized soliton is not really a soliton, and also, as it is shown below, in the same limit the solitons become strongly unstable, investigation was not carried out further beyond  $k > 1$ . It is relevant to stress that the parametric domain in which the three-wave gap solitons may exist in the present model, appears to be completely filled by the soliton solutions. This is a drastic difference from the four-wave model of the  $\chi^{(2)}$  gap solitons [75], in which large “voids” were found inside the formally available existence domain.

Proceeding to the stability of the fundamental solitons, one sees that it would be really difficult to investigate it analytically (in particular, VA is much less convenient for this than to search for the shape of stationary solitons). Therefore, the stability was tested by direct simulations of Eqs. (6.2), using the beam propagation method

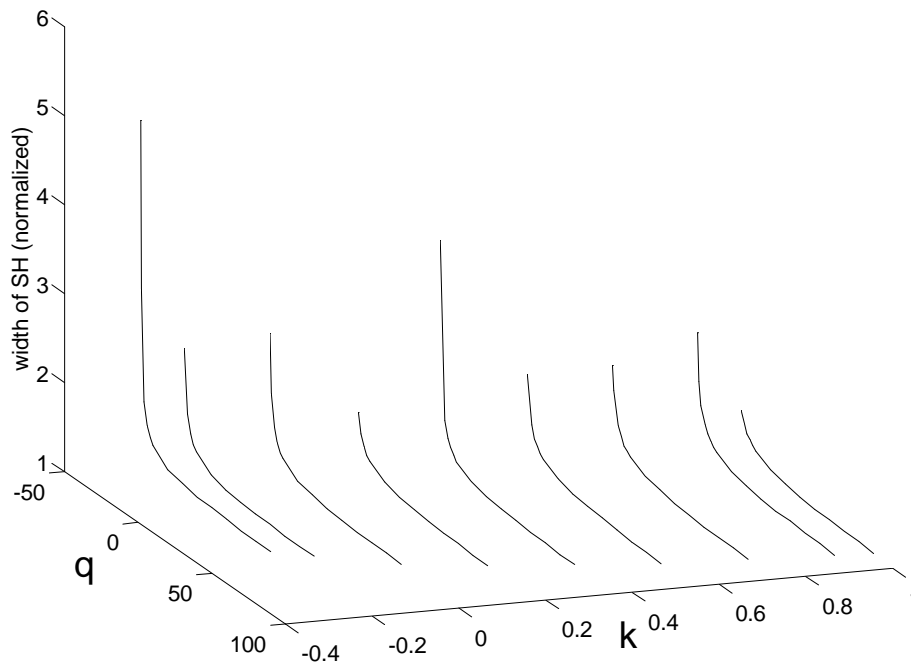


Figure 6.6: The family of the fundamental-soliton solutions: the SH width.

(BPM). The stationary shape of the solitons produced by the finite-difference numerical solution was used as the initial configuration for the BPM simulations, with an additional perturbation generated by increasing the amplitude of the wave components by 1%. In most cases, the simulations were run over the propagation distance  $z = 2\pi$  (in the notation of Eqs. (6.2)), which was quite sufficient to discern between the stable and unstable solitons; however, in some cases, the simulations were run twice as long for stable solitons, in order to further check the stability. No change has been observed in the longer simulations as compared to those with  $z = 2\pi$ .

It has been found that, when the mismatch  $q$  is large enough, the solitons are stable (in agreement with the results reported in [108]). The solitons existing at  $k > 0$  become unstable as  $q$  decreases past a *threshold value*  $q_{\text{thr}}^{(F)}$  (which depends on

the wave-number shift  $k$ , and slightly on the diffraction coefficient  $D$ , see below; the superscript F refers to the fundamental solitons, as another stability threshold, for two-solitons, will be found below). For smaller positive values of  $k$ ,  $q_{\text{thr}}^{(\text{F})}$  is smaller too, and for  $k < 0$  the threshold does not exist - in this case, *all* the solitons turn out to be stable in the simulations (see more details below). On the other hand, when  $k$  gets close to its limit value 1 (see above),  $q_{\text{thr}}^{(\text{F})}$  becomes very large (i.e., the stability is lost in the limit  $k \rightarrow +1$ , when the soliton demonstrates the unexpected behavior described above). The simulations also demonstrate that the instability of the solitons with  $q$  slightly below  $q_{\text{thr}}^{(\text{F})}$  evolves by developing an asymmetry between the two FH components: for instance,  $u_1$  grows, while  $u_2$  diminishes, or vice versa. Thus the instability breaks the reduction that leads from Eqs. (6.3) to (6.4). The asymmetry is enhanced as the waves propagate. For still smaller values of  $q$ , the soliton breaks up or develops large distortion very rapidly.

In Fig. 6.7, we summarize the results found numerically for the stability of the fundamental solitons, in the form of their stability and instability domains on the  $(k, q)$  (with  $k > 0$ ) and  $(D, q)$  parametric planes (the presentation of these results in the form of one three-dimensional plot is undesirable because it does not seem clear). Evidently, the borders between the domains simultaneously display the dependencies, respectively,  $q_{\text{thr}}^{(\text{F})}(k)$  and  $q_{\text{thr}}^{(\text{F})}(D)$ . With regard to the great difference in the vertical scales between Figs. 4a and 4b, it can be inferred that the diffraction parameter  $D$ , unlike the wave-number shift  $k$ , has a little effect on  $q_{\text{thr}}^{(\text{F})}$ .

Additional information is given by Fig. 6.8, where we have redrawn the stability and instability domains (the boundary between them is labeled as the “stability” curve consisting of circles) on the  $(k, q)$  parametric plane with a different scale, so that the soliton existence limit  $4k + q = 0$  (shown by crosses and labeled as the

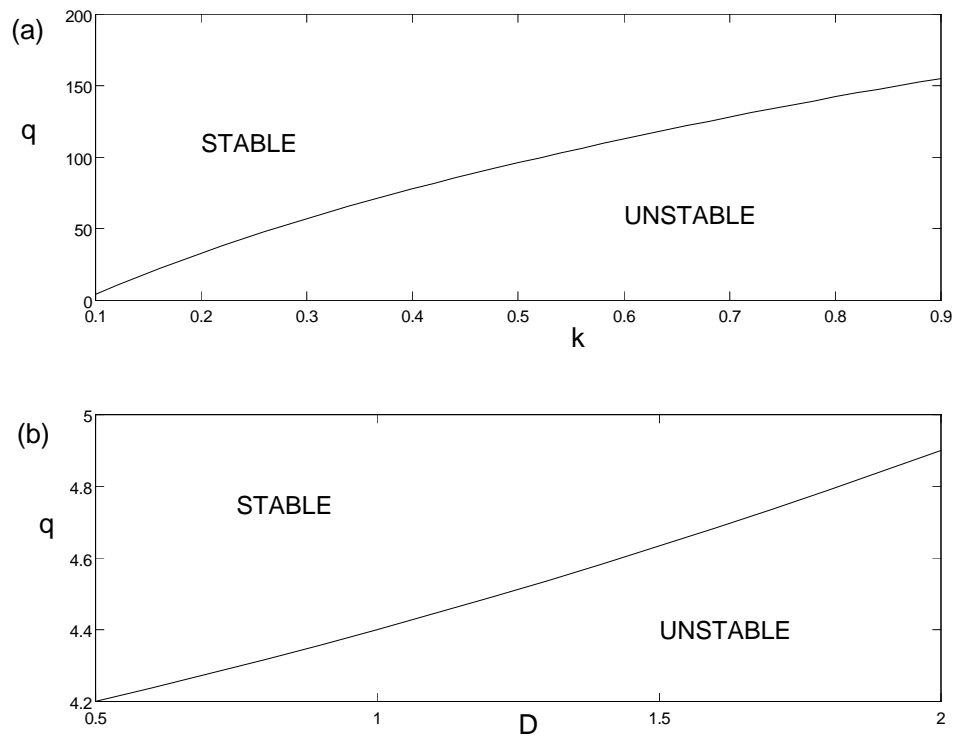


Figure 6.7: Numerically found stability domains for the fundamental solitons: (a) on the  $(q, k)$  plane at  $D = 0.5$ ; (b) on the  $(q, D)$  plane at  $k = 0.1$ .

“existence” curve), and the boundary  $q = q_0(k)$ , see Eq. (6.8), between the free-tail and tail-locked solitons (the solid line labeled “tail”) can all be plotted too,  $k < 0$  being also included. The other two soliton existence limits,  $k = \pm 1$ , form the left and right boundaries of the figure. In this figure,  $D$  is fixed at 0.5. Solitons exist above the “existence” boundary, are stable to the left of the “stability” boundary, and are of the tail-locked type above the “tail” boundary. Note that the free-tail solitons exist only in a narrow stripe. It can be deduced from Eq. (6.8) that, as  $D$  decreases, the curvature of the “tail” curve reduces (but with the end points at  $k = \pm 1$  fixed), and thus, the free-tail soliton existence region will further shrink, tending to nothing as  $D \rightarrow 0$ .

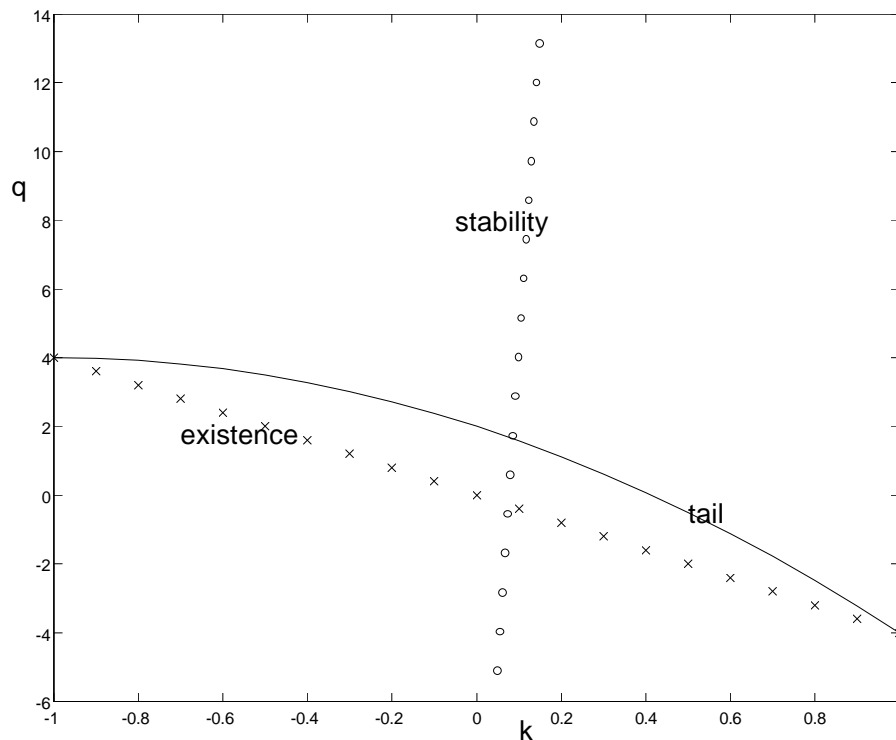


Figure 6.8: Numerically determined domains of existence, stability, and tail-type for the fundamental solitons on the  $(q, k)$ -plane at  $D = 0.5$ .

The “stability” and “existence” curves intersect in Fig. 6.8 at  $(k, q) = (0.08, 0.3)$ ; thus, *all* the solitons at  $k < 0$  are *stable*, which was verified in many runs of the numerical simulations. It is also noteworthy that, at the negative mismatch,  $q < 0$ , there is only a tiny stability domain, at  $k$  very close to 0. It is interesting that not all the solitons with the exactly matched harmonics (corresponding to the “tail” curve) are stable. This situation is drastically different from that known for the usual  $\chi^{(2)}$  solitons, which are always stable at the exact-match point [40, 58, 75, 76]. Also, in the usual  $\chi^{(2)}$  models, *all* the tail-locked solitons (corresponding to positive mismatch) and a part of the free-tail ones (that correspond to negative mismatch) are simultaneously stable. This is different from what is depicted here: only part of

both the tail-locked and the free-tail solitons are stable.

## 6.7 Two-Soliton States

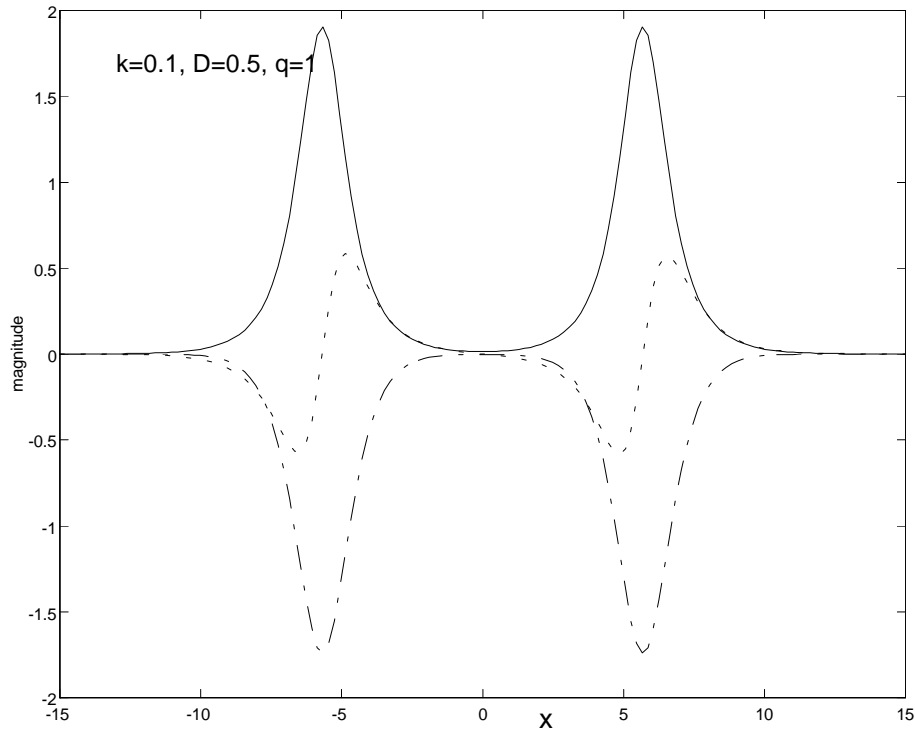


Figure 6.9: A typical shape of a numerically found two-soliton, at  $k = 0.1$ ,  $D = 0.5$ , and  $q = 1$ . The solid and dotted curves are the real and imaginary parts of the FH field  $u$ , and the dot-dashed curve is the real SH field  $u_3$ .

The parametric space of Eqs. (6.4) was numerically scanned to search for other possible stationary solutions, and a family of two-soliton bound states was found. A shape of a typical two-soliton solution is shown in Fig. 6.9. To describe the whole family of the two-soliton solutions, in Figs. 6.10 - 6.12 we plot the FH and SH amplitudes, together with the SH width of the individual bound pulses, vs.  $q$  and  $D$ , fixing  $k = 0.1$ . Note that the two individual pulses in the bound state always

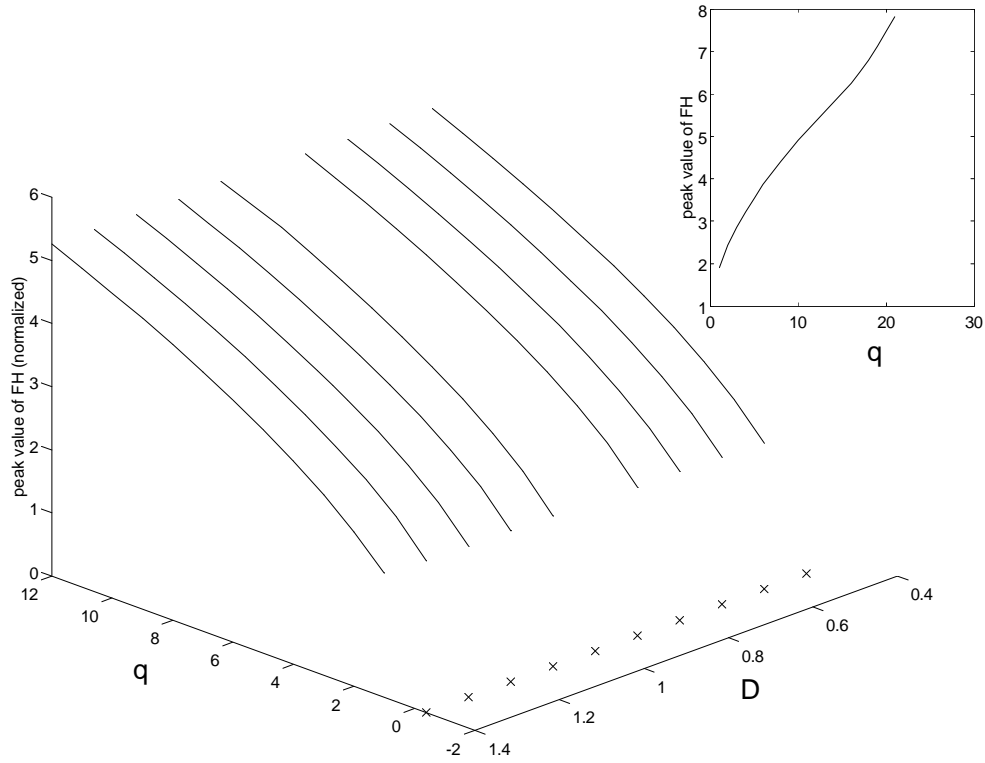


Figure 6.10: The family of the two-soliton solutions: the amplitude of the FH ( $u$ ) field plotted vs. the phase mismatch  $q$  and the SH diffraction parameter  $D$ , at a fixed wave-number shift,  $k = 0.1$ . The inset shows an extended plots of the FH amplitude vs.  $q$  at  $D = 1$ .

have equal peak values.

It can be seen that the basic features of the two-soliton solutions are similar to those of the fundamental-soliton ones. The amplitudes of the FH and the SH components increase, while the widths decrease, with the increase of  $q$ . The effect of changing  $D$  is much smaller. As can be expected, the SH amplitude and width decrease and increase, accordingly, with the increase of  $D$ , while the FH amplitude and width are only slightly affected by changing  $D$ . The soliton existence limit,  $4k + q = 0$ , is also included in Figs. 6.10 and 6.11, showing the trend of the solitons to disappear by getting infinitely broad and having vanishing amplitudes in this

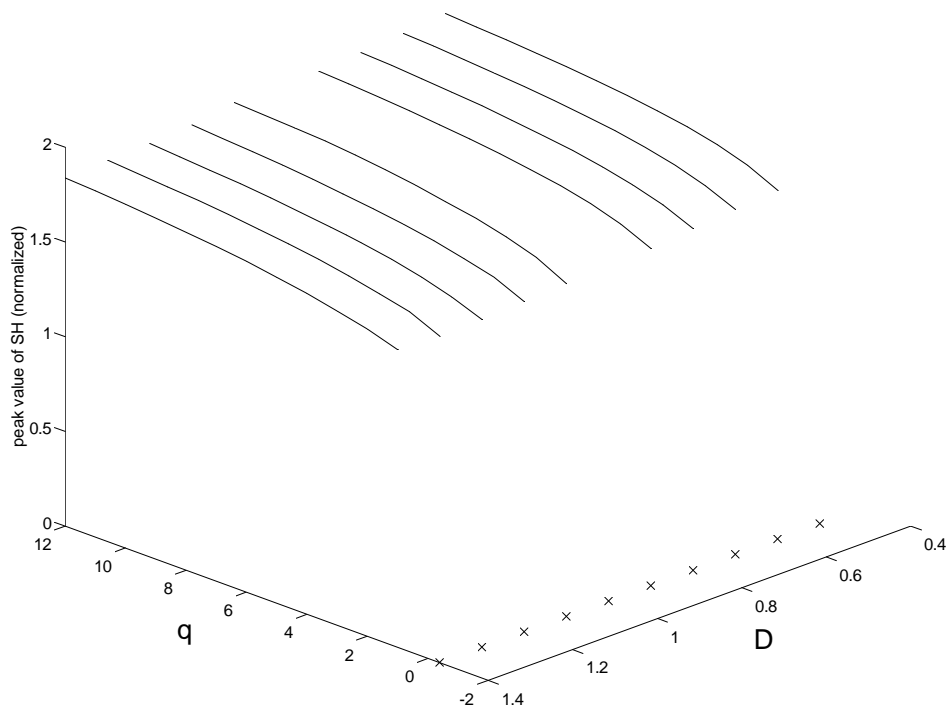


Figure 6.11: The family of the two-soliton solutions: the amplitude of the SH ( $u_3$ ) field. The line consisting of crosses in Figs. 6.10 and 6.11 shows the existence boundary  $4k + q = 0$  for the free-tail solitons.

limit. The curves were not traced up to the limit because of the slow convergence of the numerical scheme; however, there is no doubt that this trend persists.

In the limit  $q \rightarrow \infty$ , when the SH field can be eliminated to cast the model into the Massive Thirring Model (MTM) form [108], the two-soliton solution only exists under restricted conditions [146]. This inspires one to search for the two-solitons' existence limit for large  $q$  and the way they disappear when approaching the limit. In the inset of Fig. 6.10, we show the dependence of the FH amplitudes vs.  $q$  for  $k = 0.1$  and  $D = 1$ , with  $q$  extended to larger values. It can be seen that the amplitude keeps on increasing, and the increase accelerates when at  $q \sim 20$ . The widths of the waves (not plotted here) are decreasing accordingly. Thus, the

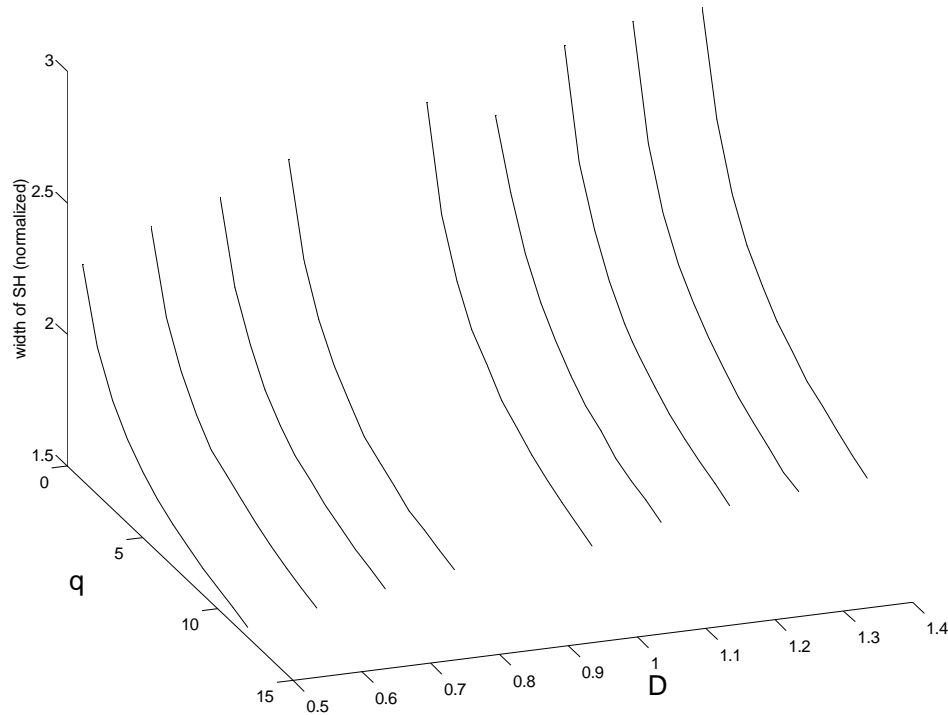


Figure 6.12: The family of the two-soliton solutions: the SH width of the individual bound pulse inside the two-soliton.

trend for the two-solitons is to become taller and narrower as  $q$  increases. At  $q > 20$ , the numerical scheme has failed because of an instability caused in it by the large change of the derivatives at the sharp peaks of the pulse. Although an exact existence limit of the two-solitons was not reached at large  $q$ , we conjecture that they disappear through a collapse-like mechanism, similarly to what is well-known in the multidimensional  $\chi^{(3)}$  models.

A specific characteristic of the two-soliton is the dependence of the separation  $S$  between the individual bound pulses on the model's parameters. The simulations demonstrate that the separation is nearly immune to the changes of the parameters over most of the range considered, except that  $S$  slightly decreases with increasing  $q$ , and increases at those existence limits,  $k = 1$  and  $4k + q = 0$ , where the

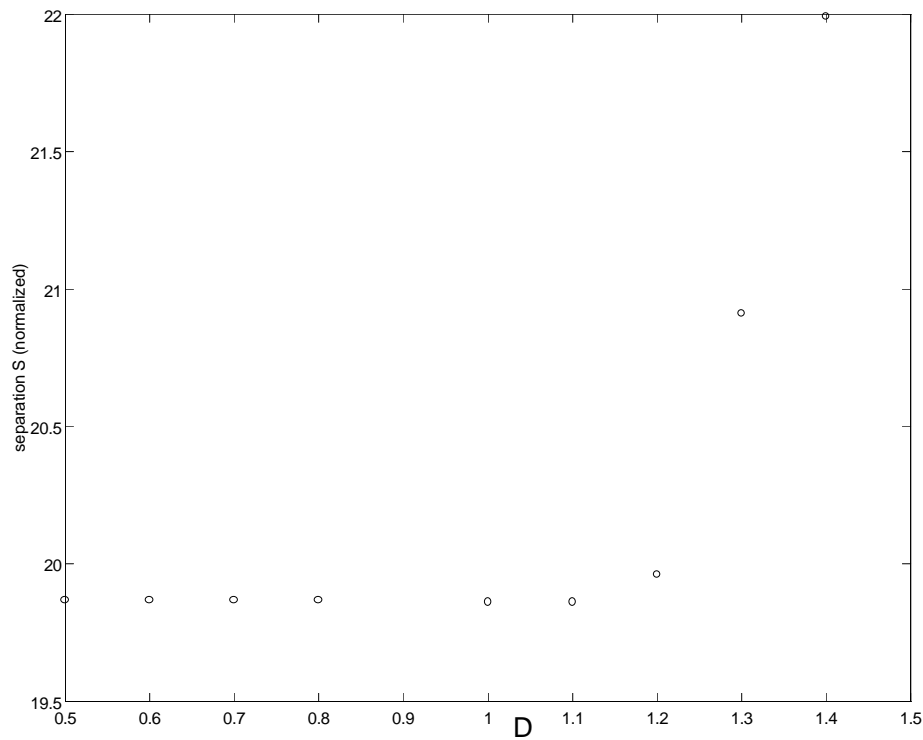


Figure 6.13: The separation between the bound pulses inside the two-soliton vs. the diffraction parameter  $D$ , at  $k = 0.1$  and  $q = 10$ .

fundamental solitons broaden indefinitely. It seems that, near these limits, the individual pulses repel each other stronger as they spread out. A separate plot of the dependence  $S$  vs.  $D$  is shown in Fig. 6.13 for  $q = 10$  and  $k = 0.1$ . It demonstrates an interesting feature that, beyond  $D \approx 1.1$ , the separation of the pulses rapidly increases with  $D$ . This probably indicates a two-solitons' existence limit at large  $D$ .

The effect of the wave-number shift,  $k$ , on the characteristics of the bound-state solutions was also investigated. Without displaying detailed results, it is sufficient to note the characteristics of the two-solitons vary with  $k$  similarly to those of the fundamental solitons (see Figs. 6.3 - 6.5): with increasing  $k$ , the amplitudes

increase and the widths decrease. As the existence limits,  $k = 1$  and  $4k + q = 0$ , are approached, the solitons broaden and amplitudes vanish.

Stability of the two-solitons is an important issue, as similar bound states are also known in the usual (two-wave)  $\chi^{(2)}$  model, but they are *always unstable* [43]. On the other hand, a numerically stable object similar to a two-soliton was found in simulations of the four-wave  $\chi^{(2)}$  gap-soliton model combining SHG and the Bragg scattering, but completely ignoring the diffraction (dispersion) [75]. We have performed systematic BPM simulations of perturbed two-solitons in order to test their stability in the present model (it is virtually impossible to study the stability analytically - first of all, because the stationary two-soliton is not known in an analytical form). As well as in the case of the fundamental solitons, the initial perturbation added to the stationary two-solitons was generated by an increase of the amplitudes of the two constituent pulses by 1%, and the simulations were then, typically, run over the propagation distance of  $z = 2\pi$ , which was sufficient to conclude if the two-soliton was stable or not. In many cases when the two-solitons seemed stable, the runs were made twice as long in order to control the accuracy of the results, which, however, never revealed an additional instability.

The stability was first tested for fixed  $k = 0.1$ , while  $q$  and  $D$  were varied. As well as the fundamental solitons, the two-solitons are always found to be *stable* at a sufficiently large phase mismatch  $q$ , getting destabilized when  $q$  decreases past a specific two-soliton's threshold value  $q_{\text{thr}}^{(2)}$ . As an illustration, in Figs. 6.14 and 6.15 we show a typical example of the evolution of slightly perturbed stable and unstable two-solitons, corresponding to  $q$  taken, respectively, above (at  $q = 6$ ) and beneath (at  $q = 1$ ) the threshold. Only the FH components are shown in Figs. 6.14 and 6.15,  $v_1$  being displayed in the region  $x < 0$ , and, simultaneously,  $v_2$  at  $x > 0$ . This

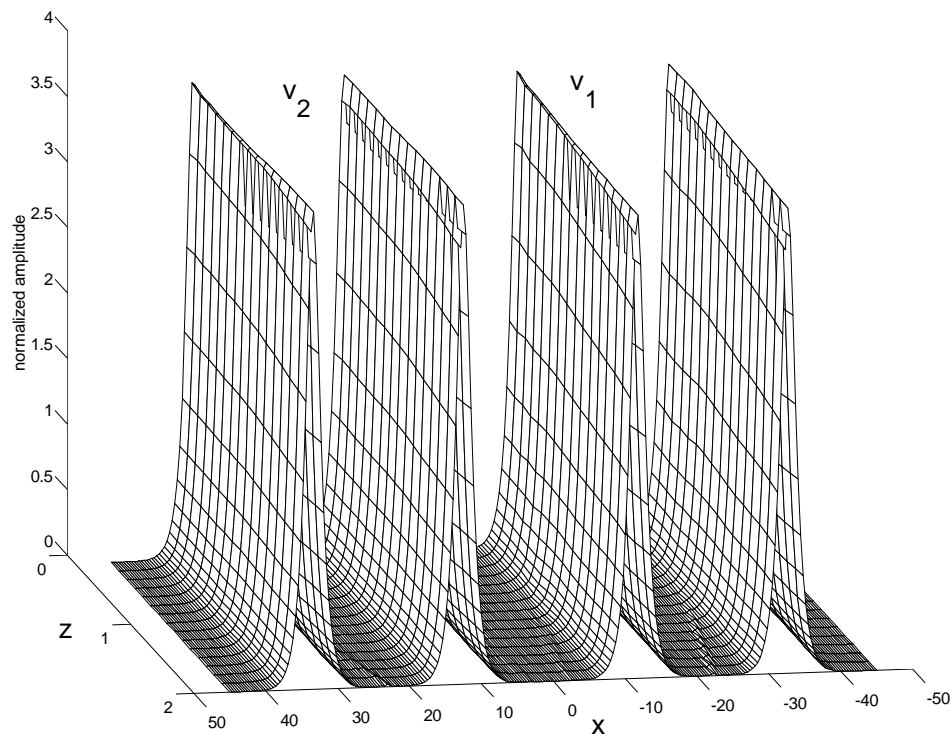


Figure 6.14: Evolution of a slightly perturbed two-soliton over a propagation distance of  $2\pi$  above the instability threshold, at  $k = 0.1$ ,  $D = 1.2$ , and  $q = 6$ . ( $z$  is in units of  $\pi$ .)

way of presenting the numerical results was adopted for convenience; in reality, of course, both components occupy the same space in the medium. It can be seen that the stable two-solitons in Fig. 6.14 maintains its shape and amplitudes, while the two-soliton in Fig. 6.15 clearly develops an instability, developing an asymmetry between  $v_1$  and  $v_2$  ( $v_2$  grows and  $v_1$  diminishes).

The stability threshold  $q_{\text{thr}}^{(2)}$  is found to be higher than that for the fundamental solitons, although the two thresholds are actually close. The numerically determined stability domain for the two-solitons was plotted on the  $(q, D)$ -plane in Fig. 6.16. As  $D$  increases, the threshold  $q_{\text{thr}}^{(2)}$  decreases, although the effect of changing  $D$  is actually very weak (note at the vertical scale of Fig. 6.16). Also, the border between

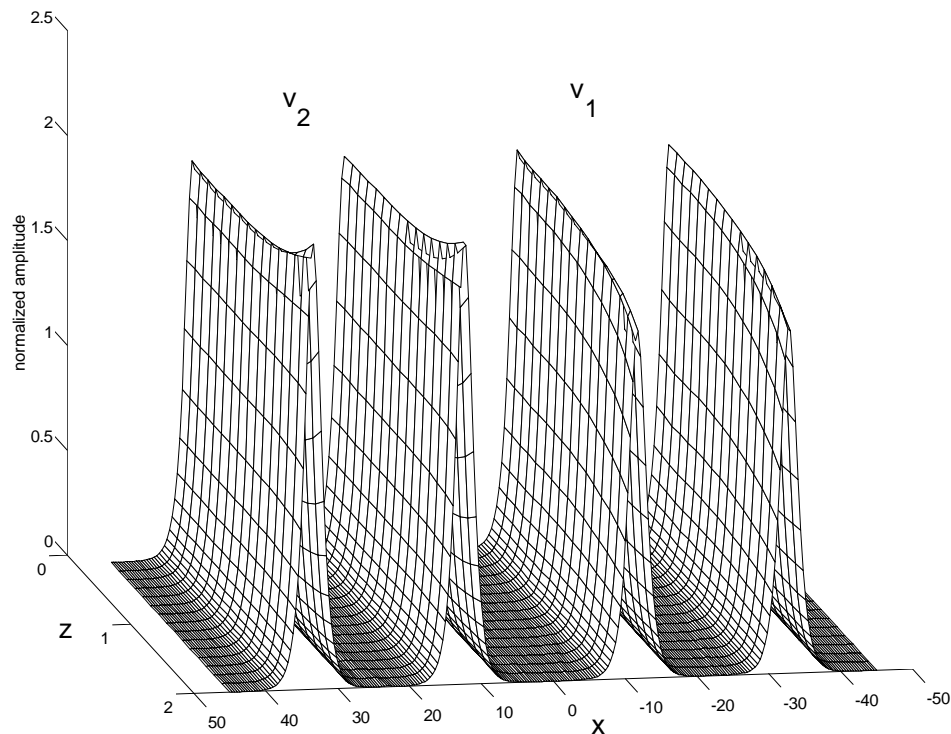


Figure 6.15: The same as Fig. 6.14, except that  $q = 1$ , i.e., *below* the two-soliton instability threshold.

the stable and unstable domains is *obtained* to be practically straight, within our accuracy. It can be seen that  $q_{\text{thr}}^{(2)}$  decreases towards the threshold value  $q_{\text{thr}}^{(F)}$  for the fundamental soliton (see Fig. 6.7b), which is quite natural: as it follows from Fig. 6.13, the two pulses in the two-soliton state separate as  $D$  increases, hence the two-soliton's stability essentially amounts to the stability of the individual pulses, although the reason why  $q_{\text{thr}}^{(2)}$  decreases with increasing  $D$ , in the range of small  $D$ , where the separation between the two individual pulses is quite insensitive to  $D$ , is unknown.

For values of  $k$  other than 0.1, the stability was also investigated. For  $k > 0.1$ , *all* the two-solitons were found to be unstable, while for  $k < 0$ , they *all* are stable, so that a stability-threshold curve on the  $(q, k)$ -plane, similar to that drawn in

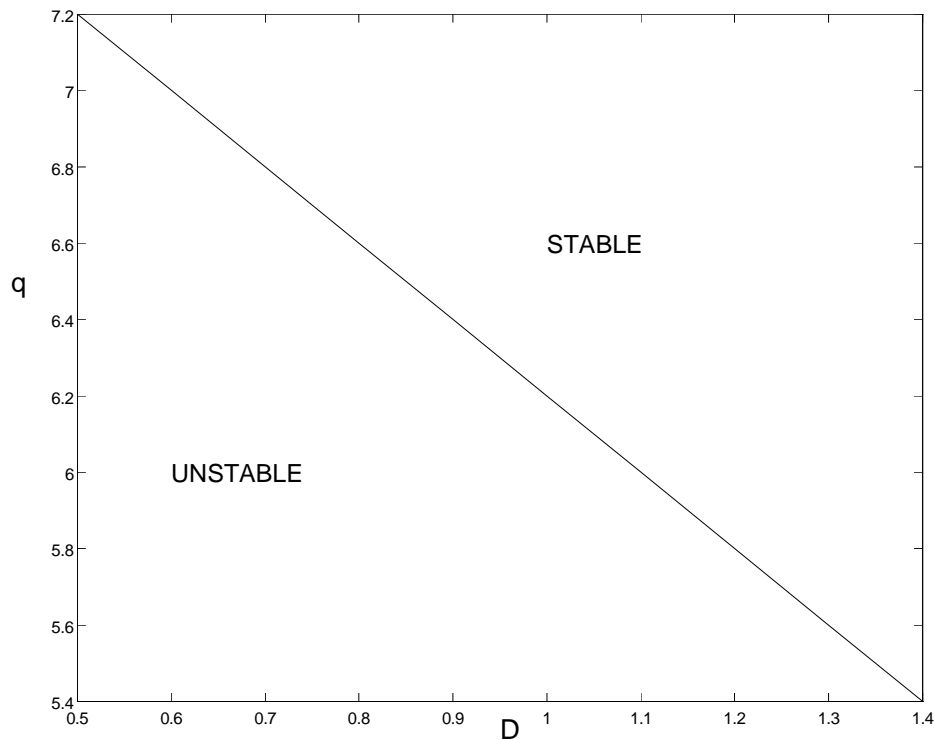


Figure 6.16: Numerically determined stability domains for the two-solitons on the  $(q, D)$ -plane at  $k = 0.1$ .

Fig. 6.7a for the fundamental solitons, cannot, as a matter of fact, be obtained for the two-solitons. However, the dependence of the two-solitons' stability threshold on the wave-number shift  $k$  can be understood by the following argument. For  $k = 0.1$ , it has been found that the threshold  $q_{\text{thr}}^{(2)}$  is close to but a bit larger than the threshold  $q_{\text{thr}}^{(F)}$  for the fundamental soliton. For  $k = 0.3$ , the results borrowed from the previous section yield  $q_{\text{thr}}^{(F)} = 57$ . If extrapolation from the  $k = 0.1$  case is approximately correct,  $q_{\text{thr}}^{(2)}$  should be  $> 60$  for  $k = 0.3$ . Then, of course, no stable two-solitons can be found for  $k > 0.1$ , since the numerical scheme fails to find any stationary two-solution for  $q > 20$ , as mentioned above in the discussion related to the inset in Fig. 6.10. Furthermore, if the two thresholds  $q_{\text{thr}}^{(2)}$  and  $q_{\text{thr}}^{(F)}$  are always

close, Fig. 6.8 can be applied, approximately, to the two-solitons too. Recall that Fig. 6.8 tells us that all the solitons are stable at  $k < 0$ , which exactly complies with the numerical finding that all the two-solitons are also stable if  $k < 0$ .

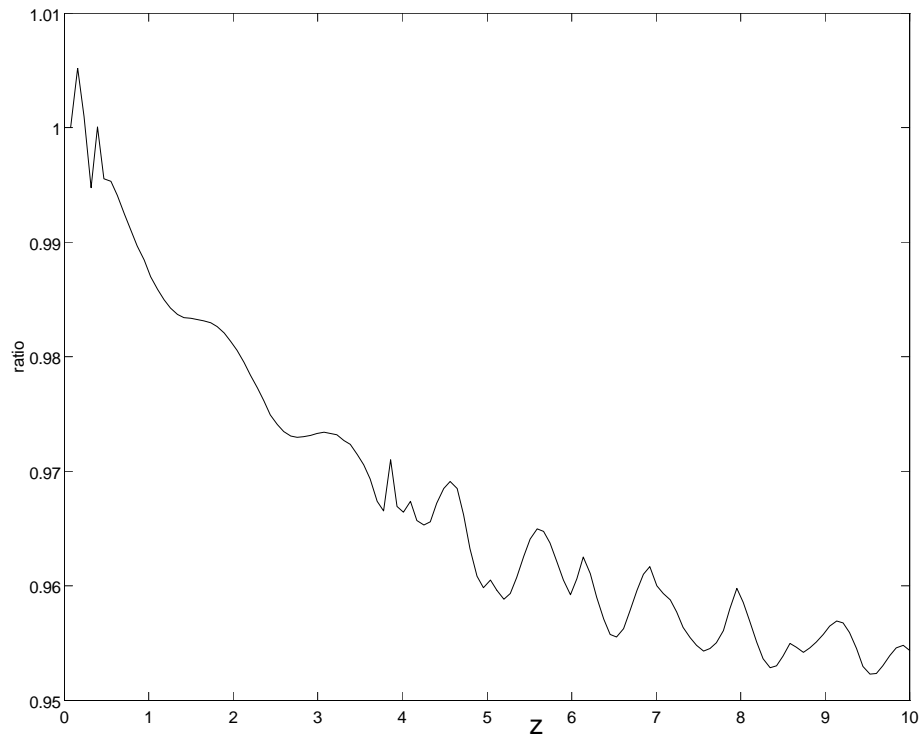


Figure 6.17: Evolution of the asymmetry ratio of the two-soliton over a very long propagation distance of  $10\pi$  well above the instability threshold, at  $D = 0.5$ ,  $k = 0.1$ , and  $q = 10$ . ( $z$  is in units of  $\pi$ .)

The last issue to be addressed is the asymmetry between the two FH components, which spontaneously develops as the solitons propagate. Although it cannot be seen in Fig. 6.14, all the stable solitons, *both* fundamental and two-solitons, are found to acquire a non-zero, although small, asymmetry. Because the stability of the two-solitons is a crucially important issue, more simulation runs with an excessively long propagation distance,  $z = 10\pi$ , were carried out to see if the asymmetry will keep

growing at the parameters values inside the stability domain. A typical example of the evolution of the asymmetry, for  $D = 0.5$ ,  $k = 0.1$ , and  $q = 10$ , is shown in Fig. 6.17. The asymmetry is quantified by the ratio of the peak values of  $v_1$  and  $v_2$ . The oscillatory evolution of the asymmetry reflects the internal vibrations of the solitary wave, when it approaches its stationary value. Similar to the quadratically nonlinear system considered in Chapters 2 & 3, the damping of these oscillations is slight (see Sec. (2.4.3) &(3.4)). Discussions of similar evolution of transients in soliton solutions in quadratically nonlinear media can be found in [58, 59, 142]. It can be seen that the ratio approaches a constant value, slightly different from 1, after propagating over a very long distance. A natural assumption that explains this numerical observation is that the underlying equations (6.3) have a general family of *asymmetric* stationary fundamental-soliton and two-soliton solutions, the solution subject to the above symmetry reduction,  $u_1 = u_2^*$ , being only a particular one. Then, a small perturbation breaking the solution's symmetry (generated, e.g., due to an inaccuracy of the numerical scheme) is expected to be neutrally stable, leading to a slightly asymmetric established solution.

Furthermore, a survey of the asymmetry over the whole parameter plane shows that, for the stable solitons in the positive  $k$  region, the asymmetry is  $\sim 1\%$ , decreasing as  $k$  decreases. In the region of negative  $k$  (where the solitons have the trend to be more robust), the observed asymmetry is  $\sim 0.1\%$  at  $k = 0.1$ , and, at  $k = 0.5$ , it drops to  $\sim 0.01\%$ , which indicates that the soliton have practically no asymmetry. This is another confirmation of the general inference formulated above, according to which the two-solitons are essentially more robust at larger negative  $k$ .

## 6.8 Conclusion

A model of the second-harmonic-generating ( $\chi^{(2)}$ ) optical medium with a Bragg grating is considered. Two components of the fundamental harmonic (FH) are assumed to be resonantly coupled through the Bragg reflection, while the second harmonic (SH) propagates parallel to the grating, hence its dispersion (diffraction) must be explicitly taken into regard. It is demonstrated that the system can easily generate stable three-wave gap solitons of two different types (*free-tail* and *tail-locked* ones), that are identified analytically according to the structure of their tails. The stationary fundamental solitons are sought for analytically, by means of the variational approximation, and numerically. The results produced by the two approaches are in a fairly reasonable agreement. The existence boundaries of the soliton are found in an exact form. The stability of the solitons is determined by direct PDE simulations. A threshold value of an effective FH-SH mismatch parameter is found, the soliton being stable above the threshold and unstable below it. The stability threshold strongly depends on the soliton's wave-number shift  $k$ , and very weakly on the SH diffraction coefficient. Stationary two-soliton bound states are found too, and it is demonstrated numerically that they are stable if the mismatch exceeds another threshold, which is close to that for the fundamental soliton. At  $k < 0$ , the stability thresholds do not exist, as *all* the fundamental and two-solitons are stable. With the increase of the mismatch, the two-solitons disappear, developing a singularity at another, very high, threshold. The existence of the stable two-solitons is a drastic difference of the present model from the earlier investigated  $\chi^{(2)}$  systems. It is argued that both the fundamental solitons and two-solitons can be experimentally observed in currently available optical materials with the quadratic nonlinearity.

# Chapter 7

## Conclusion

In this thesis, I reported the findings in the investigation of the characteristics of solitons (solitary waves) in coupled waveguides.

The investigation as reported can be divided into two categories. The first half of the thesis covers the parallel tunnel-coupled waveguides which have quadratic nonlinearity. We reported a bifurcation, which can be observed in such coupler structure. Effects due to a spatial walkoff, and different phase mismatches were also reported. Investigation was further carried out for the coupling structure when the assumption of identical waveguides was removed; i.e., solitons in asymmetric couplers were investigated.

The second half of the thesis covers coupling phenomena that can be observed in waveguides which are equipped with gratings. This is further divided into two parts. The first is on the investigation of gap solitons in a pair of linearly coupled waveguides which also have Bragg gratings inscribed in them. The nonlinearity considered here is however cubic. The reason for considering cubic nonlinearity here is that the model involved will be simpler than the same structure but with

quadratic nonlinearity. On the other hand, since coupled waveguides with Bragg gratings *and* cubic nonlinearity was a *novel* research topic, it can provide useful informations in the understanding of such a structure. The second part is on the investigation of solitons due to three wave resonant interaction in a waveguide which also has gratings in it.

In the first two chapters, we have formulated and analyzed a model describing two linearly coupled quadratically nonlinear waveguides. The model includes two equations for the fundamental harmonics, and two equations for the second harmonics. We have considered in details the most important special case of no-walkoff and fully matched harmonics, when the only control parameter is the coupling constant, the same for both harmonics in the first chapter. It was demonstrated that, alongside the obvious symmetric solitons, the model supports asymmetric solitary waves. A bifurcation point at which the asymmetric solutions appear was found exactly. A full description of these solutions in an analytical form was based on a simple variational approximation. Comparison with numerical results obtained by the shooting method has demonstrated that this approximation provides a fairly good accuracy in a range where existence of the stationary asymmetric solitons was predicted, while in some other range, asymmetric solitary-wave solutions were not found, although periodic solutions can be easily obtained. Direct simulations of the full PDE's have shown that the asymmetric solitons, whenever they exist, are always neutrally stable. On the contrary, the symmetric solitons are stable (effectively, also neutrally) only to the right of the bifurcation point, where the asymmetric solitons do not exist. To the left of the bifurcation point, the symmetric soliton is found to be unstable, demonstrating a trend to rearrange itself into the stable asymmetric soliton that exist at the same value of the coupling constant  $Q$ .

As the next steps, in chapter 2, we investigated the parallel tunnel-coupled waveguide system, when the assumption of equal fundamental and second harmonic coupling constants was removed. This is equivalent to removing the restriction that the separation between the two waveguides needs to be small. We have completely identified the entire region (that includes two sub-regions) where the asymmetric solitons exist, along with the bifurcation lines, at which the asymmetric solitons branch off from the obvious symmetric-soliton solutions. Similar to what was used in Chapter 1, the asymmetric solutions were found in the two different ways: One (analytical) approach based on the variational approximation, and another approach is direct numerical. However, the variational approach used the Gaussian ansatz. As usual, the main advantage of using this type of ansatz is a possibility to admit different components of the soliton to have different widths. Final solutions to the system of eight algebraic equations produced by the variational approximation were found numerically. Another approach which was based on direct numerical solution employed a finite-difference scheme, instead of the shooting method used in Chapter 1. The reason is that the shooting method failed to produce solutions for the range  $Q < 0.3$ . The agreement between the analytical and direct numerical results turns out to be very good, except for a very narrow region, where the SH component of the soliton is changing its sign, and its shape is strongly non-Gaussian (nonmonotonous).

Then, the stability of these soliton states was again tested by direct PDE simulations. The result is in line with previous findings: The asymmetric solitons, whenever they exist, were shown to be neutrally stable, while the symmetric solitons that obviously coexist with the asymmetric ones are always unstable. Moreover, simulations of evolution of the symmetric solitons close to the bifurcation point

and farther from it show that the unstable symmetric solitons suffer spontaneous symmetry breaking and begin to evolve into the corresponding asymmetric solitons (which they do faster if they are farther from the bifurcation point). The finding of this investigation suggests that the strong dependence of the stable asymmetric solutions upon the effective coupling parameter, or, in physical units, upon the energy of the beam, may open way to use these states for optical switching.

We then investigated the effect of the walkoff (spatial misalignment) on the solitons in the coupled waveguides for different values of the coupling constants. An estimate for the values of the walkoff parameter  $\delta$  corresponding to experimentally relevant values of the misalignment angles was obtained ( $\delta \sim 0.05$  for the angles  $\sim 0.3$  degrees). The walkoff term being small enough, the asymmetric solitons, as well as the symmetric ones existing before the bifurcation, remain robust. With increase of the parameter  $\delta$ , the solitons develop a distortion, and they finally get destructed when walkoff becomes too large.

We have also investigated effects produced by varying the phase mismatch parameter. As phase mismatch parameter,  $q$ , gets smaller than 1, the regions where the asymmetric solitons exist shrink, whereas these regions expand when  $q$  gets larger than 1. However, as  $q$  increases beyond about 4, the asymmetry stays more or less constant, especially for the case  $K = 0$ . We have also demonstrated that, in the opposite limit of very small  $q$ , one can eliminate the second-harmonic fields to transform the model into that for the twin-core fiber with the Kerr nonlinearity.

In Chapter 4, we also investigated solitons in asymmetric coupler with quadratic nonlinearity. We report results of analysis of the soliton bifurcations in such a pair of asymmetric linearly coupled waveguides. We analyzed two limiting cases, when the coupling constants at the fundamental and second harmonics are equal, or when the

coupling at the second harmonic is absent. These cases correspond to the physical situations in which the coupled waveguides are, respectively, weakly or strongly separated. Two different kinds of the asymmetry between the waveguides were considered. The first of them corresponds to a different phase mismatch between the fundamental and second harmonics in the two cores. Unfoldings of the previously known bifurcation diagrams corresponding to the symmetric coupler were studied in detail at various values of the asymmetry parameter, and stability of different branches of the solutions was tested by direct simulations. Both the unfoldings and the stability results were found to be in line with what is predicted by the elementary bifurcation theory. Solitons on the unstable branches were found to have a tendency to rearrange themselves, through the evolution of the growing dynamical perturbations, into the corresponding stable solitons.

The second kind of the asymmetry investigated was the special case when one waveguide is linear, while the other one possesses the quadratic nonlinearity. It was found that soliton solutions exist in such a system. In contrast to the case when both waveguides are nonlinear, here, the soliton solutions for the two limiting cases of the weakly and strongly separated waveguides are not much different. All the solitons were found to be stable in the latter system.

The obtained results, and especially bifurcations between solitons of different types, suggest straightforward applications of the asymmetric quadratically nonlinear couplers to the all-optical switching.

In Chapter 5, we have investigated a model describing two linearly coupled waveguides with the cubic nonlinearity, each equipped with the resonant grating. Assuming the Bragg scattering to dominate, the temporal dispersion or spatial diffraction was ignored. This resulted in four coupled-mode equations which describe

the propagation of the forward and backward waves in the two cores.

Using the variational approach, we have obtained approximate stationary solitary-wave solutions in an analytical form, which were then refined by direct finite-difference numerical computations. The analytical and numerical results are found to be in a good agreement. Both methods demonstrate the existence of asymmetric solitary wave solutions, alongside the obvious symmetric solitons. The bifurcation diagrams were constructed, showing narrowing down in terms of the coupling constant  $|\lambda|$  when either the frequency  $|\omega|$  or the velocity  $|c|$  increases. We have also found exact existence limits for the solitary waves following from the linear dispersion analysis. It was shown that the solitary-wave solutions may only exist at  $|\lambda| < 1$  and  $|c| < 1$ . For the quiescent solitons, the existence range is also limited by the condition  $|\omega| < 1$ .

Then, the stability of both asymmetric and symmetric gap solitons was tested by direct PDE simulations. The asymmetric solitons, whenever they exist, were shown to be always stable, while the symmetric ones coexisting with them are always unstable. Nevertheless, the symmetric solitons are fairly stable beyond the bifurcation points, where they do not have to coexist with asymmetric solitons.

In the last chapter, We have demonstrated the existence of spatial gap solitons, and of their bound states in the form of two-solitons, in a system of three waves, resonantly interacting in a quadratically nonlinear planar waveguide with a Bragg grating written on it. The model includes two components of the fundamental harmonic, with different orientations of their wave vectors, and the second harmonic, whose wave vector is parallel to the grating. Control parameters of the model are the phase mismatch between the harmonics and the diffraction coefficient of the second harmonic that does not interact with the grating. The analysis of the linearized

and *sem*linearized versions of the model has allowed us to identify two possible types of the solitons, distinguished by the structure of their tails (*free-tail* and *tail-locked* solitons). Then, a family of the complex fundamental-soliton solutions was constructed numerically and analytically, by means of the variational approximation, that demonstrates a fairly reasonable agreement with the numerical solutions. Soliton existence limits were found in an exact form. Mechanisms by which the fundamental-solitons disappear as these limits are approached were explored. Unlike the gap solitons in the four-wave  $\chi^{(2)}$  model, in the present one the solitons completely fill the domain where they can exist (which implies that they should be easier to observe in the experiment).

Two-soliton solutions also exist in a broad parametric range, with the separation between the bound pulses inside them very weakly depending on the parameters, except for a vicinity of the existence borders. With the increase of the mismatch parameter, the two-solitons display a trend to disappear via a collapse.

The stability of the fundamental solitons and two-solitons was analyzed by means of direct PDE simulations. It was found that both types of solitons are stable or unstable when the mismatch is, respectively, above or beneath a corresponding threshold value. The thresholds for the fundamental solitons and two-solitons are different but close, the latter one being somewhat higher. The thresholds strongly depend upon the soliton's wave-number shift  $k$ , but are nearly independent of the second-harmonic's diffraction coefficient. At  $k < 0$ , the thresholds do not exist as *all* the fundamental solitons and two-solitons are stable. Depending on the parameters, the fundamental soliton at the point of the exact matching between the fundamental and second harmonics (which is, simultaneously, a boundary between the free-tail and tail-locked solitons) may be both stable and unstable, in contrast to the usual

$\chi^{(2)}$  models. The existence of *stable* two-soliton bound states is a remarkable feature of the model, which is a drastic difference from the familiar  $\chi^{(2)}$  systems.

Because a  $\chi^{(2)}$  waveguide with the resonant grating can be easily fabricated, the most important physical result of this work is that it suggests straightforward ideas for the experimental search for single- and two-humped three-wave spatial solitons in  $\chi^{(2)}$  optical materials by means of the Bragg grating.

# Bibliography

- [1] J. L. Baird, British Patent **285**, 738 (1927).
- [2] A. C. S. van Heel, Nature **173**, 39 (1954).
- [3] K. C. Kao, G. H. Hockham, Proc. IEE, **113**, 1151 (1966).
- [4] A. Hasegawa, F. Tappert, Appl. Phys. Lett. **23**, 142 (1973).
- [5] P. N. Butcher, D. Cotter, *The Elements of Nonlinear Optics*, Cambridge University Press, Cambridge, Great Britain (1990).
- [6] Y. R. Shen, *The Principles of Nonlinear Optics*, John Wiley and Sons, New York (1984).
- [7] G. P. Agrawal, *Nonlinear Fiber Optics*, Academic Press, Inc., New York (1988).
- [8] C. R. Menyuk, R. Schiek, and L. Torner, J. Opt. Soc. Am. B, **11**, 2434 (1994).
- [9] A. G. Kalocsai and J. W. Haus, Phys. Rev. E, **52**, 3166 (1995).
- [10] A. V. Buryak, *Solitons due to Quadratic Nonlinearities* Ph. D. Thesis, Australian National University, Canberra (1996).
- [11] A. W. Snyder and J. D. Love, *Optical Waveguide Theory*, Chapman and Hall, London, Great Britain (1984).

- [12] S. Chi and Q. Guo, *Opt. Lett.* **20**, 1598 (1995).
- [13] A. Yu. Savchenko and B. Ya. Zeldovich, *J. Opt. Soc. Am. B*, **13**, 273 (1996).
- [14] D. Marcuse, *Theory of Dielectric Optical Waveguides* Academic Press, Inc., New York, U.S.A. (1991).
- [15] S. M. Jensen, *IEEE J. Quantum Electron.*, **QE-18**, 1580 (1982).
- [16] M. Romangoli, S. Trillo, and S. Wabnitz, *Opt. Quantum Electron.* **24**, S1237 (1992).
- [17] B. A. Malomed, I. Skinner, G. D. Peng, and P. L. Chu, *Phys. Rev. E* **53**, 4084 (1996).
- [18] A. W. Snyder, D. J. Mitchell, L. Poladian, D. R. Rowland, and Y. Chen, *J. Opt. Soc. Am. B* **8**, 2102 (1991).
- [19] C. Paré and M. Florjańczyk, *Phys. Rev. A* **40**, 4455 (1989); *ibid*, *Phys. Rev. A* **41**, 6287 (1990).
- [20] N. Akhmediev and A. Ankiewicz, *Phys. Rev. Lett.* **70**, 2395 (1993).
- [21] J. M. Soto-Crespo and N. Akhmediev, *Phys. Rev. E* **48**, 4710 (1993).
- [22] A. Ankiewicz, N. Akhmediev, and J. M. Soto-Crespo, *Opt. Commun.* **116**, 411 (1995).
- [23] P. L. Chu, B. A. Malomed, and G. D. Peng, *J. Opt. Soc. Am. B* **10**, 1379 (1993).
- [24] N. Akhmediev, and J. M. Soto-Crespo, *Phys. Rev. E* **49**, 4519 (1994).

- [25] T. I. Lakoba, D. J. Kaup, and B. A. Malomed, *Phys. Rev. E* **55**, 6107 (1997).
- [26] G. Cohen, *Phys. Rev. E* **52**, 5565 (1995).
- [27] S. Trillo and S. Wabnitz, *Opt. Lett.* **16**, 1 (1991).
- [28] G. L. J. A. Rikken, C. J. E. Seppen, E. G. J. Staring, and A. H. J. Venhuizen, *Appl. Phys. Lett.* **62**, 2483 (1993).
- [29] K. Clays, J. S. Schildkaut, and D. J. Williams, *J. Opt. Soc. Am. B* **11**, 655 (1994).
- [30] T. Watanabe, V. Edel, X. T. Tao, S. Shimoda and S. Miyata, *Opt. Commun.* **123**, 76 (1996).
- [31] A. Bratz, B. U. Felderhof, and G. Marowsky, *Appl. Phys. B* **50**, 393 (1990).
- [32] G. Marowsky, E. J. Canto-Said, S. Lehmann, and F. Sieverdes, *Phys. Rev. B* **48**, 18114 (1993).
- [33] E. Popov, M. Nevriere, R. Reinisch, J. L. Coutaz, and J. F. Roux, *Appl. Opt.* **34**, 3398 (1995).
- [34] S. Tomaru, T. Watanabe, M. Hikita, M. Amano, Y. Shuto, I. Yokohoma, T. Kaino, and M. Asobe, *Appl. Phys. Lett.* **68**, 160 (1996).
- [35] M. Jäger, G. I. Stegeman, W. Brinker, S. Yilmaz, S. Bauer, W. H. G. Horsthuis and G. R. Möhlmann, *Appl. Phys. Lett.* **68**, 1183 (1996).
- [36] T. C. Kowalczyk, K. D. Singer, and P. A. Cahill, *Opt. Lett.* **20**, 2273 (1995).
- [37] M. J. Werner, and P. D. Drummond, *J. Opt. Soc. Am. B* **10**, 2390 (1993).

- [38] A. V. Buryak and Yu. S. Kivshar, *Opt. Lett.* **19**, 1612 (1994).
- [39] V. V. Steblina, Yu. S. Kivshar, M. Lisak, and B. A. Malomed, *Opt. Commun.* **118**, 345 (1995).
- [40] L. Torner, C. R. Menyuk, and G. I. Stegeman, *Opt. Lett.* **19**, 1615 (1994).
- [41] R. Schick, Y. Baek, and G. I. Stegeman, *Phys. Rev. E* **53**, 1138 (1996).
- [42] W. E. Torruellas, Z. Wang, D. J. Hagan, E. W. VanStryland, G. I. Stegeman, L. Torner, and C. R. Menyuk, *Phys. Rev. Lett.* **74**, 5036 (1995).
- [43] G.I. Stegeman, D.J.Hagan, L. Torner, *Opt. Quant. Electr.* **28**, 1691 (1996).
- [44] G. Assanto, G. Stegeman, M. Sheik-Bahae, and E. Van Stryland, *Appl. Phys. Lett.*, **62**, 1323 (1993).
- [45] G. Assanto, A. Laureti-Palma, C. Sibilina, and M. Bertolotti, *Opt. Commun.* **110**, 599 (1994).
- [46] M.A. Karpierz, *Nonlinear Guided Waves and Their Applications*, OSA 1996 Technical Digest Series, **15**, 70 (1996).
- [47] A. V. Buryak, and Yu. S. Kivshar, *Phys. Lett. A* **197**, 407 (1995).
- [48] A. W. Snyder, *J. Opt. Soc. Am.* **62**, 1267 (1972).
- [49] A. W. Snyder and J. D. Love, *Optical Waveguide Theory*, Ch. 27-29 & 31, 1st Ed., Chapman and Hall, New York, U.S.A. (1983).
- [50] Y. N. Karamzin and A. P. Sukhorukov, *Pis'ma ZhETF* **20**, 734 (1974) [*JETP Lett.* **20**, 339 (1974)].

- [51] Y. N. Karamzin and A. P. Sukhorukov, Zh. Eksp. Teor. Fiz. **68**, 834 (1975) [JETP Lett. **41**, 414 (1976)].
- [52] W.H. Press, B.P. Flannery, S.A. Teukolsky, W.T. Vetterling. *Numerical Recipes in C : the art of scientific computing*, Cambridge University Press, Cambridge, London, New York (1988).
- [53] J. R . Rice, *Numerical Methods, Software, and Analysis* McGraw-Hill, New York, (1983).
- [54] G. Goubau, and F. Schwering, Proc. IEEE Antennas Propag., **A-9**, 248 (1961).
- [55] A. G. Fox, and T. Li, Bell Syst. Tech. J., **40**, 453 (1961).
- [56] J. A. Fleck, J. R. Morris, and M. D. Feit, Appl. Phys. **10**, 129 (1976).
- [57] G. P. Agrawal, *Nonlinear Fiber Optics*, Ch.2, Academic Press, Inc., New York (1989).
- [58] D. E. Pelinovsky, A. V. Buryak, and Yu. S. Kivshar, Phys. Rev. Lett. **75**, 591 (1995).
- [59] C. Etrich, U. Peschel, F. Lederer, B. A. Malomed, and Yu. S. Kivshar, Phys. Rev. E **54**, 4321 (1996).
- [60] U. M. Ascher, R. M. M. Mattheij, and R. D. Russell, *Numerical Solution of Boundary Value Problems for Ordinary Differential Equations*, Prentice-Hall Inc., New Jersey (1988).
- [61] R. Seydel, *From Equilibrium to Chaos: Practical Bifurcation and Stability Analysis*, Chap. 1, Elsevier Science Publishing Ltd., New York (1988).

- [62] S.R. Friberg, A.M. Weiner, Y. Silberberg, B.G. Sfez, and P.S. Smith, *Opt. Lett.*, **13**, 904 (1988).
- [63] S. Trillo, S. Wabnitz, E.M. Wright, and G.I. Stegeman, *Opt. Lett.*, **13**, 672 (1988).
- [64] H. Hatamihanza, P. L. Chu, B. A. Malomed, and G. D. Peng, *Opt. Commun.* **134**, 59 (1997).
- [65] A. L. Steele, J. P. Hemingway, *Opt. Commun.* **123**, 487 (1996).
- [66] W.C.K. Mak, B.A. Malomed, and P.L. Chu, *Phys. Rev. E*, **55**, 6134 (1997).
- [67] W.C.K. Mak, B.A. Malomed, and P.L. Chu, *Phys. Rev. E*, **57**, 1092 (1998).
- [68] C. R. Menyuk, *IEEE J. Quant. Electron.* **QE-23**, 174 (1987).
- [69] C. R. Menyuk, *IEEE J. Quant. Electron.* **QE-25**, 2674 (1989).
- [70] B. A. Malomed, R. S. Tasgal, *Phys. Rev. E* **49**, 5787 (1994).
- [71] A. B. Aceves and S. Wabnitz, *Phys. Lett. A* **141**, 37 (1989).
- [72] D. N. Christodoulides and R. I. Joseph, *Phys. Rev. Lett.* **62**, 1746 (1989).
- [73] C. M. DeSterke and J. E. Sipe, *Phys. Rev. A* **42**, 2858 (1990).
- [74] L. Torner, D. Mihalache, D. Mazilu, and N. N. Akhmediev, *Opt. Lett.* **20**, 2183 (1995).
- [75] U. Peschel, C. Etrich, F. Lederer, and B. A. Malomed, *Phys. Rev. E* **55**, 7704 (1997).

- [76] A. V. Buryak, Yu. S. Kivshar, and S. Trillo, *Phys. Rev. Lett.* **77**, 5210 (1996).
- [77] M. Bertolotti, M. Monaco, and C. Sibilia, *Opt. Commun.*, **116**, 405 (1995).
- [78] C. C. Yang, *Opt. Lett.*, **16**, 1641 (1991).
- [79] D. J. Kaup, T. I. Lakoba, and B. A. Malomed, *J. Opt. Soc. Am. B* **14**, 1199 (1997).
- [80] C. W. Wu, S. T. Lu, T. L. Wu, and H. C. Chang, *IEEE Photon. Tech. Lett.* **7**, 1054 (1995).
- [81] J. D. Love, and V. V. Steblina, *Electron. Lett.* **30**, 1853 (1994).
- [82] S. J. Hewlett, J. D. Love, and V. V. Steblina, *Opt. & Quant. Electron.* **28**, 71 (1996).
- [83] T. F. Krauss, R. M. Delarue, P. J. R. Laybourn, B. Vogele, C. R. Stanley, *IEEE J. of Selected Topics in Quant. Electron.* **1**, 757 (1995).
- [84] P.N. Butcher and D. Cotter, *The Elements of Nonlinear Optics*, pp. 222 and pp. 308. (Cambridge University Press, Cambridge, Great Britain, 1990).
- [85] B.A. Malomed, P. Drummond, H. He, A. Berntson, D. Anderson, and M. Lisak, *Phys. Rev. E* **56**, 4725 (1997).
- [86] G. Iooss and D.D. Joseph. *Elementary Stability and Bifurcation Theory* (Springer-Verlag, New York, Heidelberg, Berlin, 1980).
- [87] B. J. Eggleton, and C. M. de Sterke, *J. Opt. Soc. Am. B* **14**, 2980 (1997).
- [88] P. St. J. Russel, *J. Mod. Opt.* **38**, 1599 (1991).

- [89] C. M. de Sterke and J. E. Sipe, *Progress in Optics* **33**, 203, E. Wolf, Ed., North-Holland, Amsterdam (1994).
- [90] H. G. Winful, J. H. Marburger, and E. Garmire, *Appl. Phys. Lett.* **35**, 379 (1979).
- [91] H. G. winful, G. D. Cooperman, *Appl. Phys. Lett.* **40**, 298 (1982).
- [92] W. Chen and D. L. Mills, *Phys. Rev. Lett.* **58**, 160 (1987).
- [93] H. G. Winful, R. Zamir, and S. Feldman, *Appl. Phys. Lett.* **58**, 1001 (1991).
- [94] D. L. Mills, and S. E. Trullinger, *Phys. Rev. B* **36**, 947 (1987).
- [95] W.E. Thirring, *Ann. Phys.* **3**, 91 (1958).
- [96] D. J. Kaup and A. C. Newell, *Lett. Nuovo Cimento* **20**, 325 (1977).
- [97] J. E. Sipe and H. G. Winful, *Opt. Lett.* **13**, 132 (1988).
- [98] C. M. de Sterke and J. E. Sipe, *Phys. Rev. A* **38**, 5149 (1988).
- [99] C. M. de Sterke and J. E. Sipe, *Phys. Rev. A* **42**, 550 (1990).
- [100] V. E. Zakharov and A. B. Shabat, *Sov. Phys. JETP* **34**, 62 (1972).
- [101] B. J. Eggleton, R. E. Slusher, C. M. de Sterke, P. A. Krug, and J. E. Sipe, *Phys. Rev. Lett.* **76**, 1627 (1996).
- [102] C. M. de Sterke, B. J. Eggleton, and P. A. Krug, *J. Opt. Soc. Am. B* **15**, 1494 (1997).
- [103] C. M. de Sterke, N. G. R. Broderick, B. J. Eggleton and M. J. Steel, *Opt. Fiber Technol.* **2**, 253 (1996).

- [104] C. M. de Sterke, B. J. Eggleton, and P. A. Krug, *J. Lightwave Technol.* **15**, 1494 (1997).
- [105] U. Mohideen, R. E. Slusher, V. Mizrahi, T. Erdogan, J. E. Sipe, M. Gonokami, P. J. Lemaire, C. M. de Sterke, and N. G. R. Broderick, *Opt. Lett.* **20**, 1674 (1995).
- [106] Yu.K. Kishar, *Phys. Rev. E* **51**, 1613 (1995).
- [107] M. Picciau, G. Leo, and G. Assanto, *J. Opt. Soc. Am. B* **13**, 661 (1996).
- [108] S. Trillo, *Opt. Lett.* **21**, 1732 (1996).
- [109] T. Peschel, U. Peschel, F. Lederer, and B.A. Malomed, *Phys. Rev. E* **55**, 4730 (1997).
- [110] C. Conti, S. Trillo, and G. Assanto, *Phys. Rev. Lett.* **78**, 2341 (1997).
- [111] H. He and P. D. Drummond, *Phys. Rev. Lett.* **78**, 4311 (1997).
- [112] A. Kozhokin and G. Kurizki, *Phys. Rev. Lett.* **74**, 5020 (1995).
- [113] P. N. Butcher, and D. Cotter, *The Elements of Nonlinear Optics*, Ch. 2, Cambridge University Press, Cambridge (1990).
- [114] G. P. Agrawal, *Nonlinear Fiber Optics*, Ch. 7, Academic Press, Inc., New York (1989).
- [115] A.M. Maier, *Kvantovaya Elektron. (Moscow)* **9**, 2996 (1982).
- [116] D. Marcuse, *Theory of Dielectric Optical Waveguides*, 2nd Ed., chap. 3, Academic Press, Boston, U.S.A. (1991).

- [117] K. Tai, A. Tomita, J. L. Jewell, and A. Hasegawa, *Appl. Phys. Lett.*, **29**, 236 (1986).
- [118] W. E. P. Padden, C. M. de Sterke, D. C. Psaila, *Phys. Rev. E*, **52**, 4, 4401 (1995).
- [119] Y. R. Shen, *The Principles of Nonlinear Optics*, Chapter 6, Wiley, New York (1984).
- [120] R. DeSalvo, D. J. Hagan, M. Sheik-Bahae, G. I. Stegeman, E. W. Van Stryland, and H. Vanherzeele, *Opt. Lett.* **17**, 28 (1992).
- [121] S. Trillo and G. Assanto, *Opt. Lett.* **19**, 1825 (1994).
- [122] A. L. Belostotsky, A. S. Leonov, and A. V. Meleshko, *Opt. Lett.* **19**, 856 (1994).
- [123] G. Assanto, G. I. Stegeman, M. Sheik-Bahae, and E. Van Stryland, *IEEE J. Quant. Electron.* **QE-31**, 673 (1995).
- [124] A. Kobaykov, U. Peschel, and F. Lederer, *Opt. Commun.* **124**, 184 (1996).
- [125] A. Kobaykov and F. Lederer, *Phys. Rev. A* **54**, 3455 (1996).
- [126] L. Lefort and A. Barthelemy, *Electron. Lett.* **31**, 910 (1995).
- [127] G. Assanto, Z. Wang, D. J. Hagan, E. W. Van Stryland, *Appl. Phys. Lett.* **67**, 2120 (1995).
- [128] L. Lefort and A. Barthelemy, *Opt. Lett.* **20**, 1749 (1995).
- [129] D. J. Kaup, *Stud. Appl. Math.* **55**, 9 (1976).

- [130] G. Daguanno, C. Sibilìa, E. Fazio, and M. Bertolotti, *Opt. Commun.* **142**, 75 (1997).
- [131] M. Nisoli, S. Stagira, S. Desilvestri, O. Svelto, G. Valiulis, and A. Varanavicius, *Opt. Lett.* **23**, 630 (1998).
- [132] S. French, A. Miller, M. Ebrahimzadeh, *Opt. & Quant. Electron.* **29**, 999 (1997).
- [133] S. Wu, G. A. Blake, Z. Y. Sun, J. W. Ling, *Appl. Opt.* **36**, 5898 (1997).
- [134] M. Nisoli, S. Desilvestri, G. Valiulis, A. Varanavicius, *Appl. Phys. Lett.* **68**, 3540 (1996).
- [135] P. J. Wegner, and M. D. Feit, *Appl. Opt.* **35**, 890 (1996).
- [136] R. Danielius, A. Dubietis, G. Valiulis, and A. Piskarskas, *Opt. Lett.* **20**, 2225 (1995).
- [137] T. J. Zhang, Y. Kato, K. Yamakawa, H. Daido, and Y. Izawa, *Japanese J. of Appl. Phys.* **34**, 3552 (1995).
- [138] V. Smilgevicius, A. Stabinis, *Opt. Commun.* **106**, 69 (1994).
- [139] G. P. Banfi, P. Ditrapani, R. Danielius, A. Piskarskas, R. Righini and I. Santa, *Opt. Lett.* **18**, 1547 (1993).
- [140] H. T. Tran, *Opt. Commun.* **118**, 581 (1995).
- [141] B. A. Malomed, D. Anderson, and M. Lisak, *Opt. Commun.* **126**, 251 (1996).
- [142] A. V. Buryak and Yu. S. Kivshar, *Phys. Rev. Lett.* **78**, 3286 (1997).

- [143] Y. J. Chen, *Phys. Lett. A* **234**, 443 (1997).
- [144] C. Conti, S. Trillo, and G. Assanto, *Phys. Rev. E* **57**, R1251 (1998).
- [145] A.V. Mikhailov, *Pis'ma Zhurn. Eksp. Teor. Fiz.* **23**, 356 (1976).
- [146] D. David, J. Harnad, S.Shnider, *Lett. Math. Phys.*, **8**, 27 (1984).